Late Stages of Continent-Continent Collision: Timing, Kinematic Evolution, and Exhumation of the Northern Rim (Aar Massif) of the Alps

Herwegh, M.[1], Berger A.[1], Glotzbach, C.[2], Wangenheim, C.[2,3], Mock, S.[1], Wehrens, P. [1,4], Baumberger, R.[1,4], Egli, D.[1], Kissling, E.[5]

[1] Institute of Geological Sciences, University of Bern, Baltzerstrasse 1+3, CH-3012 Bern

[2] Institute for Geology, Leibniz University Hanover, Callinstrasse 30, 30167 Hannover, Germany

[3] now at Department of Geosciences, University of Tuebingen, Wilhelmstrasse 56, 72074 Tuebingen, Germany

[4] now at Federal Office of Topography, Swiss Geological Survey, Seftigenstrasse 264, 3084 Wabern, Switzerland

[5] Institute of Geophysics, ETH Zürich, Sonneggstrasse 5, CH-8092 Zürich, Switzerland

Abstract

The Alpine front's External Crystalline Massifs represent exhumation of mid-crustal basement during late-stage continent-continent-collision. We unravel the geodynamic evolution of the Northalpine front (Aar Massif) by combining structural and low-T thermochronometric data. A crustal-scale tectonic restoration (Neogene-present) and estimation of associated changes in exhumation rates become possible. The European continental margin experienced multiple switches from horizontal- to vertical- and again to horizontal-dominated tectonics. Early thrust-related inversion of rift basins is followed by a switch to rapid vertical exhumation, with deformation along steep

reverse/normal faults. This vertical tectonics related to a positive buoyancy force of the European crust induced by lower crustal delamination of the Aar Massif during an orogenic rollback process of the European lithosphere (~22-20 Ma). Differential rock uplift rates of up to 1.3-1.6 km/Myr resulted, which decreased northwards to 0.1 km/Myr. Reducing buoyancy forces (isostatic compensation) led to a horizontal tectonic style again. Persisting compressional forces induced an orogen-scale strain partitioning with dextral transpressive faults in the south and simultaneous crustal-scale northwest-directed thrusting in the north. 'En-bloc' exhumation of the entire Aar Massif in the thrusts' hanging wall occurred between 13-5 Ma and 5-0 Ma at rates of 0.5-0.9 km/Myr and 0.6-0.8 km/Myr, respectively. It is this late-stage thrusting in combination with surface erosion, which shaped today's prominent Northalpine front. Switches between horizontal and vertical tectonics might generally be relevant for late continent-continent-collision stages. Here buoyancy forces of non-thinned continental crust entering the subduction zone cause a strong vertical tectonic deformation style instead of classical thrust tectonics.

Introduction

Plate convergence rate in classical Andean type subduction zones decreases significantly when the former passive continental margin with its low-density crust enters the subduction zone, which results in an Alpine style continent-continent collision (e.g. Burchfiel, 1980; Laubscher, 1983; Tricart, 1984; Schmid et al., 1996; Handy et al., 2010; Rosenberg and Kissling; 2013 and references therein). During early stages of this collisional environment, sediment nappes are scraped off from their substratum (e.g. Pfiffner, 1993; Bellahsen et al., 2014; Lacombe and Bellahsen,

2016, von Tscharner et al., 2016; Bauville and Schmalholz, 2017; Pfiffner, 2017; Mair et al., 2018; Nibourel, 2019) and are basally accreted to the overriding hanging wall by thin-skinned tectonics. With progression, basement becomes incorporated by thick-skinned tectonics (e.g. Leloup et al., 2005; Boutoux et al., 2016; Lacombe and Bellahsen, 2016; Pfiffner, 2017 and references therein) resulting in sediment-basement nappes or in large-scale sedimentary recumbent thrust-folds with crystalline cores (e.g. Escher et al., 1993; Pfiffner, 2016). The European Alps provide a typical scenario for such a transition from subduction to continent-continent collision, where particularly the late collisional stage can be studied in great detail (e.g. Burkhard and Sommaruga, 1998; Bellahsen, et al. 2014; von Hagke et al., 2014; Rosenberg and Kissling, 2013; Mock et al., 2019). Very prominent in the case of the Alps is the formation of the so-called External Crystalline Massifs (ECMs see Fig. 1; e.g. Marquer and Gapais, 1985; Lacombe and Mouthereau, 2002; Leloup et al. 2005; Bellahsen et al., 2012; Egli and Mancktelow, 2013; Lacombe and Bellahsen, 2016), which represents exhumation of the underlying European basement (the thick continental lower plate of collision) of up to 18-20 kilometers in the case of the Aar and Mont Blanc Massifs (Leloup et al., 2005; Challandes et al., 2008; Bellahsen et al., 2014; Wehrens et al., 2017; Diamond and Tarantola, 2015). In the past, five end-member models for the exhumation of the Aar Massif have been suggested (Fig. 2): (i) An antiformal-imbricate-stack model, where in-sequence imbricate thrusting resulted in a piling up of the stack and a progressive steepening of the older southern imbricate thrusts (Burkhard, 1990; Burkhard and Sommaruga, 1998; Burkhard, 1999). (ii) A fault-bend-fold model, where the Aar Massif is considered to represent a large-scale fold above a basal detachment (Burkhard, 1990; Krayenbuhl and Steck, 2009). (iii) A pure-shear model, where horizontal bulk shortening and vertical stretching

above a basal thrust zone is accommodated by conjugate sets of non-coaxial shear zones (Choukroune and Gapais, 1983; Marquer, 1990; Burkhard, 1990). All these models require the existence of an Alpine sole thrust, which is in contrast to (iv) a pure buoyancy-driven uplift model without considerable horizontal shortening (Burkhard, 1990; Neugebauer et al., 1980). (v) A recently proposed multistage block-extrusion model is mainly based on changes in slab dynamics with (a) a first stage of incipient thick-skinned thrust tectonics followed by (b) buoyancy-driven vertical tectonics requiring decoupling in the lower crust and (c) evolution of a sole-thrust-like domain during retrograde cooling and last stages of compression (Herwegh et al., 2017). Independent of the model, there is seemingly a consensus that tectonic inheritance related to Permo-Carboniferous and Mesozoic crustal-scale extension provided the base for the type and style of inversion of the ECMs during the Alpine continent-continent collision (e.g. Rohr, 1926; Burkhard, 1988; Butler and Mazzoli, 2006; Bellahsen et al., 2012; Bellahsen et al., 2014; Boutoux et al., 2014; Lacombe and Bellahsen, 2016). In the following, we will focus on the Aar Massif as study area to improve our knowledge on the kinematics, timing, and geodynamics of the exhumation of the largest ECM. Given the high topographic and structural relief, the good outcrop conditions as well as the many recent studies on structural geology, metamorphism, and dating of Alpine deformation, the Aar Massif provides an excellent field laboratory for studying the late collisional stages of the Alpine orogeny.

While in the ECMs of the Western Alps (Fig. 1) thorough tectonic reconstructions and thermochronometric studies provide insights into their exhumation history (e.g. Lacombe and Mouthereau, 2002; Leloup et al., 2005; Glotzbach et al., 2008, 2011; Egli and Mancktelow, 2013; Bellahsen et al., 2014, Boutoux et al., 2016, Lacombe

and Bellahsen, 2016), a comprehensive structural study through the entire Aar Massif including its internal deformation structure is yet missing. This is mainly due to the fact that previous studies either focused on deformation in the sediments (e.g. Burkhard, 1988; Hänni and Pfiffner, 2001; Herwegh and Pfiffner, 2005; Pfiffner et al., 2011), the basement-cover contact or the gneisses in the northern part of the massif (e.g. Rohr, 1926; Müller and Arbenz, 1938; Labhart, 1966; Kammer, 1989; Marquer and Burkhard, 1992; Krayenbuhl and Steck, 2009; Mair et al., 2018, Fig. 3), or the massif internal basement deformation only (e.g. Steck, 1968; Choukroune and Gapais, 1983; Marquer and Gapais, 1985; Rolland et al., 2009; Goncalves et al., 2012). A first article by Herwegh et al. (2017) aimed at closing this gap by synthesizing a series of structural, geomorphological, thermochronological, and geochemical studies carried out over the past years at different scales along the Haslital transect of the central Aar Massif (Fig. 4; Baumberger, 2015; Wehrens, 2015; Fölmli et al., 2015; Belgrano et al., 2016; Berger et al., 2016; Wehrens et al., 2016, 2017; Berger et al., 2017; Schneeberger, 2017; Schneeberger et al., 2017; Mair et al., 2018; Baumberger et al., in press). Building upon this knowledge and combining it with our new results we aim at the following goals:

1. Presenting the structures and kinematics responsible for the Aar Massif's exhumation reaching from the time of peak metamorphism to the present-day.
2. Unravelling the thermal evolution by means of thermometry and low-T thermochronometry with focus on three major thermal stages: (i) peak metamorphism, retrograde cooling below the (ii) zircon fission track (ZFT) closing temperatures (~240-300°C) and (iii) apatite fission track (AFT) closing temperature (~110°C).

3. Linking of (1) and (2) with tectonic retro-deformation in order to obtain a consistent geodynamic model for the inversion and exhumation of the former European passive continental margin in the area of the central Aar Massif during the late stage Alpine orogeny.

For this purpose, we first introduce the known geological framework, followed by a description of the applied methodology. New and existing structural data are then presented and combined with geochronologic/thermochronometric data to constrain the rock uplift and exhumation history of the central Aar Massif. Finally, we broaden the scale by discussing the relevance of the new findings of the Aar Massif in the context of other ECMs before we then set the scene for a geodynamic consideration in light of late stage continent-continent collisional processes. In the context of this framework, we will use the terms ‘vertical tectonics’ and ‘horizontal tectonics’, for shortening with dominant vertical rock uplift and dominant horizontal displacement component, respectively. Note that in both cases, however, a horizontal/vertical component exists as well, which though is circumstantial in the respective situation of overall compression.

Methods

This study is based on a combined approach of structural fieldwork, construction and retro-deformation of tectonic cross-sections, as well as low-temperature thermochronometry. We used the corresponding outcomes to decipher the tectonic and geodynamic evolution as well as the timing of exhumation of the central Aar Massif, putting special emphasis on its morphologically steep northern rim (Fig. 3),

where the exposed basement-cover contact serves as an important structural marker to unravel different deformation episodes.

Structural Analysis

In terms of structural data, fault/shear zones and foliations, their geometries and kinematics as well as relative age relationships were collected in order to unravel different deformation events. We will use the term 'fault zone' for shear planes, which clearly underwent brittle deformation at some stage of their evolution, while the term 'shear zone' is solely used for localized ductile deformation. Note that fault zones often have a ductile precursor during earlier high temperature stages of Alpine deformation (see also Steck, 1968; Wehrens et al., 2016, 2017). Thin-sections were manufactured perpendicular to the foliation and parallel to the stretching lineations of shear zones for microstructural investigations on the style, the kinematics, and the physico-chemical conditions of deformation.

For the northern part of the study area, we build on findings of previous studies (Rohr, 1926; Mueller and Arbenz, 1938; Labhart, 1966; Kammer, 1989; Michalski and Soom, 1991; Berger et al., 2017; Mair et al., 2018) but also add own new structural data. For the southern part of the study area (bright coded colors of units in Fig. 4), this work greatly benefits from previously published data (Wehrens et al., 2016, 2017; Herwegh et al., 2017; Schneeberger et al., 2017). The following data provided the base for the construction of a tectonic NNW-SSE section (Figs. 4 and 5a): (i) Surface information from the geological map of Berger et al. (2016) and GeoCover (map.geo.admin.ch; swisstopo), (ii) structural field data from this and previous studies (Wehrens et al., 2016, Herwegh et al., 2017, Schneeberger et al., 2017, Wehrens, et al. 2017), (iii) the 3D model of the large-scale shear zone pattern of the Haslital transect

(Baumberger et al., in press), (vi) the tectonic cross-section on Plate V of Pfiffner et al. (2011), (v) the seismic section C1 of Pfiffner et al. (1997), and information from local earthquake tomography (Diehl et al., 2009). The late stage thrust structures (see Fig. 4 and explanations below) and offsets of the basement-cover contact made it possible to construct individual thrust planes via 3D modeling using the software MOVE (Petroleum Experts; Midland Valley). The projection of Triassic dolomites, which act as a marker for the basement-cover contact, into the section plane provides a first order estimate on (i) localized deformation expressed by the displacement along individual thrust planes and on (ii) the strain accommodated by internal shortening along distributed thrust sheets (bending and folding of the Triassic dolomite layer).

Retro-deformation

To gain insight into the geodynamic evolution of the area during the late stage of continent-continent collision, the tectonic NNW-SSE section was retro-deformed by using line (basement-cover contact) and area balancing (crystalline crust, i.e. base of sediment cover down to Moho; Helvetic nappes). The following steps were carried out:

- Retro-deformation of displacements of the youngest thrust-related deformation in the Aar Massif (Pfaffenchopf phase, see below).
- ‘Unfolding’ of the bulge of the Aar Massif and the overlaying Alpine nappe stack by using the contact between autochthonous sediments and basement rocks as a marker horizon (Nibourel et al., 2018). The maximum depth of this contact at peak metamorphic conditions was obtained by assuming a geothermal gradient of 25°C/km and using pre-existing data on geothermometry (see supplementary Figure 2 in Herwegh et al. (2017)).

Moreover, P-T data from Goncalves et al., (2012) (450°C/6.5 kbar) and Oliot et al., (2010) (490°C/7.3 kbar) were used, respectively, for the southern Aar Massif and the Gotthard nappe to define maximum burial depth at peak metamorphic conditions.

- Combining aforementioned information with the seismic (Pfiffner et al., 1997) and seismo-tomographic data (Diehl et al., 2009; Wagner et al., 2012) from the European continental crust north of the Aar Massif (e.g. Moho depth), the geometry of the southward dipping European plate was estimated at the time of peak metamorphic conditions. Permo-Carboniferous half-graben structures served as markers, allowing us to reconstruct the locations of synrift Permo-Carboniferous transtensional faults and the origin of the steep Alpine normal and reverse faults (Handegg phase shear zones).
- Back-stripping of the Helvetic nappes and Infrahelvetic slices defined the promontory of these sediment units on top of the former passive European continental margin.
- Following the argumentation of Campani et al. (2012), von Hagke et al. (2014b), and Schlunegger and Kissling (2015), we assumed the average topographic mean elevation for the last 20 Ma to be similar to today's. Consequently, we attributed the rock mass between the Helvetic nappes and the paleo-surface to overlying units (i.e. undifferentiated Penninic and Austroalpine). Note that these units became accreted to the orogenic wedge prior to the rise of the Aar Massif but since then, they are continuously eroding owing to progressive exhumation (Schlunegger and Kissling, 2015 and references therein).

Low-T Zircon and Apatite Thermochronometry

In order to obtain information on the temperature evolution in the range between maximum burial and today's exhumed rocks, different geothermometers were applied for peak metamorphic conditions (see Herwegh et al., 2017 for details). Additionally, data from zircon and apatite fission track thermochronometry were used to estimate the timing and location of different intervals of rock uplift (Fig. 5). In general, fission tracks will be annealed when the target mineral is exposed long enough to temperatures above the partial annealing zone (PAZ; e.g. Gleadow et al., 1983). During cooling, the fission tracks start to accumulate as soon as the sample passes the PAZ, where still parts of the former produced fission tracks will anneal (shortened). For the sake of simplicity, often the mean value between the upper and lower temperature limit of the PAZ is used as closing temperature (T_c) (e.g. Gleadow et al., 1983; Brandon et al., 1998; Ketcham et al. 2007; Reiners and Brandon, 2006). In the case of zircon, there exist significant variations in the estimation of the effective T_c ranging from about 205 - 350°C in field-based studies (Zaun and Wagner, 1985; Hurford, 1986; Brandon et al., 1998; Bernet, 2009; Rahn et al., 2019) and even up to 360°C in the case of experimental approaches (Yamada et al., 1995; Tagami et al., 1998; Rahn et al., 2004). Given this uncertainty, we use for ZFT both the often applied 240°C but also 300°C. The reasoning for also using the latter relates to large discrepancies between ZFT ages and radiometric ages obtained for deformation stages with robust P-T constraints (see discussion below for details). For the AFT thermochronometer, we apply the mean T_c approach and use a value of 110°C (Brandon et al., 1998; Ketcham et al., 2007; Reiners and Brandon, 2006).

ZFT data were compiled from Michalski and Soom (1990) and Wangenheim (2016) and perpendicularly projected at the respective sample's altitude onto the tectonic NNW-SSE section (Fig. 5b). On the basis of the location of the data points with similar ZFT ages, the timing of the passing the effective T_c at about ~240-300°C can be revealed. AFT data were collected from Michalski and Soom (1990), Vernon et al. (2009), and the PhD thesis of C. Wangenheim (2016; Fig. 5c). Given the sensitivity of the low T_c of the apatite system on topography controlled cooling (Vernon et al., 2009; Glotzbach et al., 2011; Grasemann and Mancktelow, 1993; Mancktelow and Grasemann, 1997; Stüwe et al., 1994), we tried to reduce potential age variations owing to lateral topographic changes by only considering samples close to the tectonic NNW-SSE section (projection distance of <10-13 km to each side of the profile trace). The sample locations were projected perpendicular to the NNW-SSE section and domains with similar age intervals were color-coded in order to detect potential age trends (Fig. 5c).

Geological Setting

Pre-Alpine Evolution

The central Aar Massif consists of a polymetamorphic basement with mainly Ordovician- and Variscan-orogeny-related gneisses and migmatites (Innertkirchen-Lauterbrunnen zone, Erstfeld zone, Guttannen zone, Ofenhorn-Stampfhorn zone, Grimsel zone, Ausserberg-Avat zone), which are dissected by post-Variscan (~300 Ma) magmatic intrusions (Mittagfluh granite, Central Aar granite (CAGr), Grimsel granodiorite (GrGr), Southwestern Aar granite; Figs. 4 and 5a). Within the late to post-Variscan geodynamic transtensional framework, Permo-Carboniferous half-grabens formed, which were filled by volcano-clastic sediment series (e.g. von

Raumer and Neubauer, 1993; Abrecht, 1994; Schaltegger and Corfu, 1995; Berger et al., 2016).

During Mesozoic times the future Aar Massif was part of the proximal passive continental margin of the European plate. In the Triassic, continental to shallow marine sedimentation occurred, followed by an emersion of large parts of the future Aar Massif during the Lower Jurassic (Alemannic land; Trümpy, 1949). Subsequently, the Tethys Ocean (Valais trough in its northern part; Pfiffner, 2009) opened to the south, which is referred to as the Penninic domain. The Adriatic passive continental margin (Austro-/Southalpine) defines the Tethys' southern termination. During Mesozoic rifting, the area of the present-day Aar Massif was only slightly affected by crustal extension, as manifested by the occurrence of half-graben structures filled by Middle Jurassic to Cretaceous sediments (Burkhard, 1988; Hänni and Pfiffner, 2001; Herwegh and Pfiffner, 2005; Nibourel, 2019) but without substantial crustal thinning. The Aar Massif therefore represents a proximal part of the European passive continental margin, which was situated still north of the necking zone typically found at the transition to the more extended to hyper-extended continental crust in such margins (see for example Figure 1 in Mohn et al., 2012).

It is important to note that the Aar Massif's crustal rocks were intensely tectonically pre-conditioned, which resulted in the following steeply dipping large-scale mechanical discontinuities:

- NE-SW trending subvertical mineral bandings and foliations in Ordovician to Variscan polymetamorphic gneisses (Steck, 1968; Abrecht and Schaltegger, 1988; Abrecht, 1994; Zurbriggen, 2015).

- Steep intrusion contacts (often NE-SW trending) of the post-Variscan granitoid plutonites as well as metabasic and aplitic dikes (Labhart, 1977; Abrecht and Schaltegger, 1988; Abrecht, 1994; Keusen et al., 1989; Wehrens et al., 2017; Schneeberger et al., 2017).
- NE-SW trending steep extensional faults, some of which already formed during Permo-Carboniferous times, others evolved or became reactivated later during Mesozoic rifting (Rohr, 1926).

Alpine Deformation

During compressional tectonics at the onset of the late Paleogene continent-continent-collision between the Adriatic and European plate (e.g. Schmid et al., 1996; Rosenberg and Kissling, 2013; Schmid et al., 2017) the sediment cover in the south of the former European margin was sheared off from their substratum, forming the Helvetic nappe stack (Drusberg, Axen, and Infrahelvetic (lower Helvetic) nappes; Pfiffner et al., 2011, Prabé phase of Burkhard (1988) and Kiental phase of Günzler-Seiffert, 1943; Burkhard, 1988) and was accreted to the base of the Penninic-Austroalpine nappe stack of the upper plate. This classical nappe stacking terminated in the Neogene, when the entire nappe stack experienced a passive upward bulging by the rise of the Aar Massif (Grindelwald phase of Günzler-Seiffert, 1943; Burkhard, 1988). Since the pioneering idea of Günzler-Seiffert's (1943) Grindelwald phase, numerous structural and petrographic studies on massif internal domains were performed in the last years, allowing nowadays for a more distinct kinematic view, particularly in the case of the central (i.e. Haslital) transect (Steck, 1966; Challandes et al., 2008; Rolland et al., 2009; Goncalves et al., 2012; Mock, 2014; Baumberger,

2015; Baumberger et al., in press; Wehrens et al., 2016, 2017; Schneeberger et al., 2016; Berger et al., 2017; Herwegh et al., 2017; Mair et al., 2018; Buess, 2019; Nibourel, 2019).

Structures, Kinematics, and P-T Conditions in the Central Aar Massif

Recent studies on the structural and kinematic evolution of the Aar Massif in the Haslital transect defined a subdivision of Günzler-Seiffert's Grindelwald phase into three kinematically distinguishable sub-phases: (1) The reverse faulting dominated Handegg phase (Wehrens et al., 2016, 2017), (2) the strike-slip dominated Oberaar phase (Wehrens et al., 2016, 2017), and (3) the thrust-related Pfaffenchopf phase (Berger et al., 2017). Note that here we strictly distinguish the terms 'thrusts' and 'reverse faults' for crustal ramps and fault planes with dip angles of about 30° and >45°, respectively, with both showing hanging wall up movements. Since there is a pronounced structural difference between the northern and southern part of the central Aar Massif, we focus first briefly on the well-known and described occurrences of Handegg and Oberaar phase structures in the south, before proceeding then to a more detailed analysis, with new data, of the so far less known northern part.

Early exhumation structures of the southern part of the Haslital transect are predominantly located within post-Variscan plutonites and relate to the Handegg phase fault zones (Wehrens et al., 2016, 2017; Figs. 4 and 5). They mainly consist of SE dipping and NE-SW trending reverse faults with steep down-dip lineations (Steck, 1968; Choukroune and Gapais, 1983; Marquer and Gapais, 1985; Challandes et al., 2008; Rolland et al., 2009; Wehrens et al., 2016, 2017; Baumberger et al., in press; Belgrano et al., 2016; Herwegh et al., 2017; Schneeberger et al., 2017; Egli et al.,

2018). They formed under mainly viscous aseismic, in parts seismic, conditions (Wehrens et al., 2016). These faults, several kilometers in length and few decimeters to decameters in width, dispersedly transect the massif showing a decreasing spacing from about 200 m to <100 m towards Grimsel Pass (see Choukroune and Gapais, 1983; Wehrens et al., 2017 and supplementary material therein). Their activity is mainly responsible for generating today's exposed metamorphic N-S gradient, showing increasing peak metamorphic conditions from about 250°C/2.5 kbars to 450°C/6.5 kbars (Goncalves et al., 2012; Wehrens et al., 2017; Herwegh et al., 2017 see their electronic supplementaries). Particularly towards the southern rim of the central Aar Massif, E-W and NE-SW trending dextral strike- to oblique-slip zones of the Oberaar phase occur. Among them, the crustal-scale Grimsel Pass shear zone is the most prominent one in terms of shear zone width and spatial extent (see Fig. 4 and Baumberger et al., in press; Wehrens et al., 2017). It first evolved as a reverse fault during the Handegg phase and was then reactivated as a major strike-slip shear zone. At depth, mylonites and ultramylonites evolved into cataclasites and fault gouges during progressive exhumation and cooling (Kralik et al., 1992; Rolland et al., 2009; Wehrens et al., 2016; Berger et al., 2017) eventually resulting in a hydrothermally active fault (Pfeiffer et al., 1992; Hofmann et al., 2004; Belgrano et al., 2016; Egli et al., 2018; Diamond et al., 2018).

From a large-scale geological point of view, the northern domain clearly differs from the southern one (Figs. 4 and 5a): (i) No post-Variscan plutonites exist but instead polymetamorphic gneisses prevail. (ii) At the northern rim of this domain the basement-cover contact is exposed. Most evident are subvertically oriented wedges of Mesozoic and locally Permo-Carboniferous sediments, which are associated with major faults and are sandwiched between basement units (Figs. 4 and 5a). Near

Innertkirchen two prominent sediment wedges occur, the so-called ‘Pfaffenchopf’ and ‘Loibstock’ wedge (PFW and LBW in Fig. 4; Rohr, 1926; Mueller and Arbenz, 1938). Despite evidence for an original subvertical orientation of the wedges, nowadays they show recumbent syncline-like structures, with moderately southeast dipping sediments in the apparent limbs. Our new results demonstrate that both wedges are tectonically situated in a domain where a large number of moderately SE-dipping thrust faults of the Pfaffenchopf phase exist (purple lines in Figs. 4 and 5a). These faults are often discrete (few cm to few dm), are widely spaced (mean spacing 100-150 m, min. 50 m, max. 300 m), dissect the basement-cover contact by transposing the hanging wall towards NW (Figs. 6a, 7-9), and form a fault array (fault array 1) in its entirety (Figs. 4 and 5). Structurally, the appearance of this fault array 1 represents (iii) the major difference compared to the southern domain, since it dips towards the SE, where it can be traced until the area of Guttannen before disappearing below the surface (Fig. 4). (iv) Vice versa, the Oberaar phase strike-slip faults diminish from south to north (Figs. 4 and 5a), while the Handegg phase faults are present in the basement units of the entire study area. In the following, we present new data on geometries, kinematics, and metamorphic conditions of the different structures found in the northern domain, starting with the oldest Alpine structures - the Handegg phase.

Like in the southern domain, the Handegg phase faults in the north dip also towards the SE. However, dip angles are less steep (mean orientation 140/70; Figs. 5a and 8). They are still characterized by down-dip stretching lineations (mean 160/64; Fig. 8) with a dominant reverse faulting component (Figs. 5a and 8). Across the Massif, the displacement along individual faults is rather small (few decimeters to tens of meters). Given the large number of these faults, however, substantial subvertical cumulative

displacement in the range of kilometers was accommodated by differentially accumulated rock uplift towards the south (Fig. 5a; see also Herwegh et al., 2017). The polymetamorphic gneisses show a steep foliation, which is oriented parallel to the aforementioned Handegg phase shear zones. However, owing to the polyphase and long-lasting deformation history since the Ordovician, older generations of foliations, experiencing up to amphibolite facies metamorphic conditions, exist (Abrecht, 1994 and references therein). Their coarse-grained microstructures, with coarse sheet silicates like white mica and biotite, are transposed from their already steep pre-Alpine orientation into the one of the Handegg phase. Peak metamorphic conditions during the Handegg phase did not exceed 300°C in this northern domain (Frey and Mählman, 1999; Bambauer et al., 2009; Berger et al., 2017; Herwegh et al., 2017). Hence, the finer grained Alpine metamorphic mineral assemblage as well as the low-T overprint of quartz, as manifested by low-T crystal plasticity and very limited amount of bulging recrystallization, allow for a clear discrimination between the pre-Alpine high-grade fabrics and their low-T Alpine overprint.

The subsequent Pfaffenchopf phase is characterized by moderately SE dipping and NE-SW striking faults (mean 135/32; Fig. 8) with SE dipping stretching lineations (mean 145/30; Fig. 8). It is evident at a variety of scales that both the Handegg phase faults/foliation and the Handegg phase/pre-Alpine foliation are dragged into the Pfaffenchopf fault planes, indicating a younger age of the latter (Fig. 6b, c; see also Labhart, 1966). However, as already recognized by Kammer (1989), both the steeply and shallowly dipping planes were active synchronously and the spacing of the latter, i.e. Pfaffenchopf planes, decreases with increasing strain. Macroscopically, the stretching lineations on the two planes show an identical NW-SE striking orientation. From a microstructural point of view, the retrogression from Variscan amphibolite

facies to an Alpine lower greenschist facies mineral assemblage on both planes as well as an associated grain size reduction document synchronous activity (Fig. 6c). We thus suggest a reactivation of the old steep structures (Handegg phase and earlier pre-Alpine foliations) during Pfaffenchopf phase faulting. Together with the new Pfaffenchopf planes, this forms two geometric and mechanical discontinuities, with a top to the NW sense of shear (Fig. 6). This relationship is visible at a variety of scales, ranging from hundreds of meters (Fig. 6a), over the outcrop (Fig. 6b), down to the thin-section scale (Fig. 6c; see also Kammer, 1989). Pfaffenchopf shearing may have initiated at temperatures between 250 - 300°C. This can be inferred from the typical occurrence of low-temperature crystal plasticity (grey arrow in Fig. 6c), as well as the local and rare manifestation of bulging recrystallization in quartz. Mostly, however, quartz is affected by brittle fractures and associated dissolution-precipitation processes (Fig. 6c pressure solution (white arrow); see also Kammer, 1989 and Berger et al., 2017). Mass transfer and precipitation processes in the form of shear veins along the Pfaffenchopf thrust planes are often observed. Chemically and mechanically most important is the evolution of phyllonitic zones along the two actively sheared foliation planes of the Pfaffenchopf phase (Kammer, 1989; Berger et al., 2017). They evolved out of a complex interplay between alteration of feldspars and episodic stages of precipitation, partial dissolution, and replacement of sheet silicate phases (Berger et al., 2017). Note that such phyllonitic shear zones are key for the mechanical behavior of basement rocks during the late stage of collision since they represent a rather typical deformation style for low temperature deformation (<300°C, Jefferies et al., 2006; Wibberley, 2005; Bellahsen et al., 2012; Egli et al., 2017).

As already observed by Labhart (1966), NE-SW striking faults with a subvertical dip (mean 120/87, Fig. 8) and N-block up movement represent the youngest fault

generation, since they cut Handegg as well as Pfaffenchopf faults (Fig. 7). Accordingly, older foliations are dragged into the fault planes. The individual faults are very discrete (few mm to cm thick and several tens of meters long) and commonly have fault gouges in their core as evident from underground exposures (Labhart, 1966). These widely spaced faults are not very abundant and are mainly observed in the Gadmen valley. For that reason, they are referred to as Gadmen faults (Berger et al., 2017). Note that the apparent spatial restriction of these faults to the Gadmen valley is probably illusive. They are also found in the Eiger-Mönch-Jungfrau area (Mair et al., 2018) and in the eastern Aar Massif (Nibourel, 2019). They might also occur in the southern areas of the Aar Massif, there, however, (i) the lack of Pfaffenchopf structures and (ii) the parallel nature of the Gadmen and Handegg faults inhibits a discrimination based on cross-cutting relations. The fact that gouge-filled fault cores also occur in this region (Fölmli et al., 2015; Wehrens et al., 2017; Schneeberger et al., 2017), some of them along faults with N-block up movement, might indeed indicate that Gadmen faults as the youngest fault generation could be more dispersed over the entire Aar Massif than visible at a first glance. Labhart (1966) pointed out that in terms of the tectonic framework no interpretation for these young faults exist and even hypothesized a potential post-glacial origin.

Age Constraints on the Exhumation Structures

Radiometric Age Data

In the southern domain, radiometric Ar-Ar and K-Ar dating on sheet silicates (biotite, white mica) yields geologically reliable ages in the range of 22-17 Ma and 14-12 Ma, respectively, recording deformation at elevated temperatures (>350°C) for ductile

shearing during the Handegg and the Oberaar phase (see Challandes et al., 2008; Rolland, et al., 2009; Berger et al., 2017). At the southern boundary of the study area, Pleuger et al. (2012) documented K-Ar ages of non-cohesive fault gouges between 14.9-10.8 Ma, with lower ages for decreasing grain size fractions. The fact that these ages overlap with those obtained for ductile shearing poses the question of inheritance of old mylonitic ages during brittle shearing. Exactly this behavior has recently been documented for the northern part of the study area, where K-Ar ages from young fault gouges yield ages of the ductile shearing and not of the brittle overprint (Berger et al., 2017). Given these limitations in dating of low-T deformation in gouges by the K-Ar system, we compiled and present in the following data from low-T thermochronometry (ZFT, AFT) to unravel the young deformation history.

Zircon Fission Track Data

In the working area, existing ZFT data of Michalski and Soom (1990) was combined with new ones (Wangenheim, 2016; Figs. 4 and 5b, Table 1 in the supplementary material). Projection of the sampling locations and associated fission track ages into the NNW-SSE cross-section shows a consistent age range between 13-12 Ma (with 15.5 Ma as an outlier) in the Hanging wall of the Pfaffenchopf fault array 1 between the Guttannen area and Grimsel Pass (Figs. 4 and 5b). Along the NNW-SSE profile this iso-age range defines a linear trend (stippled black line in Figure 5b), which is slightly inclined towards the north. In the northern part of the Erstfeld zone and in the upper part of the Pfaffenchopf fault array 1, ZFT dating yields older ages ranging from 27.5 Ma down to 16.4 Ma (Figs. 4 and 5b). In the central to northernmost parts of the Innertkirchen-Lauterbrunnen zone the ZFT ages are oldest ranging from 88.4 to 136.3 Ma (Figs. 4 and 5b).

Interpretation of ZFT Ages

Within error, the ZFT ages of 13-12 Ma in the southern Aar Massif are matching the 14-12 Ma Ar-Ar and K-Ar ages of white mica derived from mylonites of the same area. White mica neocrystallized during retrograde Oberaar phase reactivation of the former high-temperature Handdegg phase shear zones (Figs. 4 and 5b; Rolland et al., 2009; Berger et al., 2017). The fact that in these retrograde mylonites (i) biotite is unstable and breaks down into chlorite, (ii) white mica is neo-recrystallized, and (iii) quartz is affected by subgrain rotation recrystallization indicates synkinematic temperatures in the range between 300-350°C. Hence, when applying a ZFT closing temperature (T_c) of 240°C, these rocks should have experienced at the same time 240°C and 300-350°C, which cannot be the case. Such discrepancies are known from literature (e.g. Brandon et al., 1998; Rahn et al., 2004; Garver et al., 2005; Bernet, 2009) and solving this problem is out of the scope of the current study. We therefore proceed in the following by using both, 240°C and 300°C as lower and upper end member of the ZFT T_c, respectively. Based on these assumptions, the 13-12 Ma ZFT age range connected by the stippled black line in Fig. 5b indicates (i) that this range represents the age of cooling of these rocks through the 300/240°C isotherm and (ii) that this block was uplifted in its entirety without considerable jumps across the pre-existing steep Handegg phase faults within the southern three quarters of the Aar Massif (Fig. 5b). Note that all these samples are situated in the hanging wall of the projected Pfaffenchopf fault array 1 (Fig. 5b) and were therefore passively exhumed during northwest-directed thrusting along this array. In contrast, the northernmost samples in this hanging wall are significantly older with an age range between 22-15 Ma, assuming the 27.5 Ma (partially annealed?) sample to be an outlier. This range fits with the time of maximum burial and the radiometric age dating of the Handegg

phase in the southern domain (see above). Hence, the 22-15 Ma ZFT ages indicate that this part of the hanging wall rocks was already cooled below the T_c at the time of the onset of N-directed thrusting along the Pfaffenchopf fault array 1. Pre-Pfaffenchopf, subvertical uplift along the steep reverse faults of the Handegg phase and associated cooling represent therefore the most likely interpretation. With the northernmost ZFT samples being located within the Pfaffenchopf fault array 1 (Figs. 4 and 5b), the obtained ZFT age range from 88 to 136 Ma is geologically not meaningful since it is much younger and older than Variscan and Alpine metamorphism, respectively. Therefore these ages seem to be partially annealed only. During Alpine metamorphism, these samples were situated at peak metamorphic temperatures of about 250°C (Berger et al., 2017; Herwegh et al., 2017) and therefore never reached temperatures above the ZFT PAZ during the Alpine orogeny but stayed at maximum in the PAZ. The older fission tracks were therefore partly preserved and the ZFT age (>88 Ma) was not reset completely during Alpine deformation. Such an interpretation is in line with thermochronological studies from other parts of the Aar, Gotthard, Aiguilles Rouges, and the Mont Blanc Massif (e.g. Michalski and Soom, 1990; Seward and Mancktelow, 1994; Glotzbach et al., 2008; Glotzbach et al., 2010; Nibourel, 2019), yielding very similar ZFT ages with a dominance of ages between 21-12 Ma in the internal parts and ages >20 Ma towards the foreland. Older ZFT ages are documented all along the exposed basement-cover contact in the NW Aar Massif (e.g. Michalski and Soom, 1990), suggesting a common exhumation history and tectonic origin. In addition to the ZFT data in the Grimsel area, the only partial and complete fission track annealing of samples that experienced T_{peak} of 250°C and 300°C, respectively, is in favor of a T_c closer to 300°C than to 240°C for the ZFT in

this regional context (Fig. 10; see also Frey and Mählman, 1999; Bambauer et al., 2009; Herwegh et al., 2017).

To conclude, the ZFT data strongly corroborate the sequential evolution of first Handegg reverse-and then Pfaffenchopf thrust-faulting. The uncertainty regarding the effective T_c does not affect these outcomes. However, the different T_c values become important once dealing with rock uplift and exhumation rates (see below). As mentioned above, the correlation between thermal evolution and timing are in favor of the assumption of an upper bound T_c of 300°C rather than 240°C. However, below we proceed considering both estimates and leave it to the reader's judgement to decide which values are reckoned to be more reliable.

Apatite Fission Track Data

The compiled and projected existing (Michalski and Soom, 1990; Vernon, 2008) and new AFT data represent an age range from 10.5 to 4.2 Ma (Table 2). Here, intervals of one million years are color coded and displayed in the cross-section of Fig. 5c. Within error, the AFT ages of the Haslital between 8-5 Ma align all along a slightly N dipping linear trend (black stippled line in Fig. 5c). The oldest AFT ages (>8 Ma) are only found in the northern part of the Aar Massif, within the Pfaffenchopf fault array 1 or just above it (see data enclosed by red stippled ellipse in Fig. 5c). AFT ages <5 Ma are only found in the southern domain of the transect and in the Gotthard nappe.

Interpretation of AFT Ages

Since the T_c of apatite is located much closer to the surface, AFT can be affected by thermal disturbances in the underground, which are induced either by topographic

variations (e.g. Vernon et al., 2009; Glotzbach et al., 2010; Valla et al., 2012) or the circulation of hydrothermal fluids (Valla et al., 2016). Such effects might be the reason for some blurring of the AFT age signal in the studied transect (Fig. 5c). However, all samples have been completely reset, i.e. experienced temperatures above the AFT PAZ. Based on the AFT data present we conclude that, within error, the entire today exposed part of the Aar Massif of the Haslital transect crossed the AFT T_c at 8-5 Ma.

Discussion on the Aar Massif's Deformation and Exhumation History

The ECMs in general, and aforementioned data from the Aar Massif in particular, provide the opportunity to investigate kinematics, timing, and driving forces of exhumation processes during the late-stage continent-continent collision, when non-(hyper)extended crust is on the way to be dragged into the subduction zone. In this light, the following discussion is divided into two main parts. A first part aims at unravelling the Aar Massif's evolution. In a second part these findings are framed into a general geodynamic context for the late-stage Alpine collision.

Structures, Deformation Style, and Kinematics

Based on the presented structures of the Handegg, the Oberaar, and the Pfaffenchopf phase, it becomes evident that in the case of the Aar Massif exhumation was the result of a multistage deformation history. The fact that (i) faults represent the main massif-internal deformation features as well as their variable extent and occurrence in space (ii) and (iii) time, indicates strong time-dependent strain partitioning. Below, we will demonstrate that the general dome-shape of the Aar Massif (Grindelwald phase of

Günzler-Seiffert, 1943), results from the inversion of the former European passive continental margin and its control by inherited pre-Alpine (pre-Triassic and Mesozoic) structures providing the tectonic preconditioning for subsequent Alpine deformation. Taking the above-mentioned structural and timing constraints, we can postulate two temporally distinct deformation stages: (i) A first stage with substantial vertical tectonics (Handegg phase, 20-17 Ma), followed by (ii) a stage of partitioned transpressional deformation with two spatially separated but synchronous kinematic phases: focused dextral strike-slip shearing in the south (Oberaar phase, <14-12 Ma) and thrust tectonics (Pfaffenchopf phase, <13-12 Ma) in the north, the latter with a potential continuation in the deeper underground of the southern Aar Massif.

The steep, dominantly reverse Handegg phase faults are in an unfavorable orientation for a formation in a compressional framework with an approximately NW-SE directed principal horizontal stress orientation as suggested in previous models (e.g. Burkhard, 1999). Early studies therefore postulated a steepening of the shear zones, which would require substantial rotation from thrust-related 30° S-dipping into the steep orientations observed today. However, based on the present-day orientation of pre-Alpine dikes and the basement-cover contact, such considerable amounts of rotation have recently been questioned by Schneeberger et al. (2017) and Nibourel, (2019), respectively. For the dikes in the southern Aar Massif, Schneeberger et al. (2017) derived a maximum rotation of 20° around a horizontal axis with an azimuth of 065° since their injection in the magmatic state. This rotation angle is too low to back-rotate the steep shear zones into a 30° thrust-related orientation. Based on the orientation of the basement-cover contact and the link to the steep fault planes, Nibourel (2019) proved a steep origin of the Handegg faults in the central to eastern

Aar Massif also arguing against a substantial rotation, i.e. steepening of the fault planes.

Choukroune and Gapais (1983) already recognized a strong flattening component within the southern Aar Massif leading to the idea of a co-axial deformation style of these fault zones. Although certainly present, bulk flattening alone cannot explain the observed peak metamorphic N-S gradient from 250-450°C (see supplementary Figure 3 in Herwegh et al., 2017). Wehrens et al. (2017) and Herwegh et al. (2017) therefore suggested the accommodation of a strong vertical rock uplift component, though with an increasing flattening component with increasing metamorphic grade towards the south. In this way, the rock volume of the southern Aar Massif ascended vertically for at least 6-9 km during Handegg phase faulting with maximum estimates of 8-11 km (Fig. 10). During this stage of vertical uplift in the southern Aar Massif, rapid decompression under nearly isothermal conditions (Challandes et al., 2008; Diamond and Tarantola, 2015; Herwegh et al., 2017, see below) sustained ductile deformation in the shear zones. The latter consist of very fine-grained polymineralic (quartz, albite, white mica, epidote) ultramylonites within the stability field of biotite (400-450°C; Rolland et al., 2009; Wehrens et al., 2016, 2017). With progressive rock uplift (slower decompression) and faster cooling, ductile strain further localized in the ultramylonites with quartz, chlorite, white-mica, epidote as stable mineral assemblage (Wehrens et al., 2016, 2017; Berger et al., 2017). Note that ultramylonitic ductile deformation behavior persisted well below the ductile deformation behavior of monomineralic quartz (<300°C), as manifested by boudinaged and fractured quartz aggregates within the ultramylonites.

A major kinematic switch occurred at 14-12 Ma, when along the southern rim of the Aar Massif the Handegg phase faults, particularly the crustal-scale Grimsel Pass shear zone, were ductilely reactivated during the Oberaar phase as dextral strike- to oblique-slip faults (Rolland et al., 2009; Wehrens et al., 2017). At the scale of the entire NW-SE Aar Massif transect, this means a simultaneous activity of Oberaar phase strike-slip faulting in the south and Pfaffenchopf phase NW-directed thrusting in the north. These kinematically different phases occur coevally within the same large-scale geodynamic framework, which implies a regional-scale strain partitioning within a transpressive regime. Given our new data and the importance of the northern deformation structures for the late-stage Alpine collision, we elaborate these differences in the following in more detail.

The geometric relationship between steep Handegg structures and moderately SW-dipping Pfaffenchopf deformation structures at the basement-cover contact of the northern Aar Massif have strongly influenced the drawing style of tectonic cross-sections incorporating the Aar Massif since decades (e.g. Rohr, 1926; Mueller and Arbenz, 1938; Pfiffner et al., 2011). Particularly the apparent recumbent sediment synclines, which are sandwiched between basement gneisses of the Innertkirchen-Lauterbrunnen zone of the Pfaffenchopf- and Loibstock-wedge (Figs. 3, 4, 7 and 9), attracted a large number of geologists in the last almost 200 years provoking a variety of ideas on their formation history (see Labhart, 1966). While at the beginning an origin by magma tectonics was assumed (Hugi, 1830; Studer, 1851), these ideas were replaced by concepts of ductile folding of the basement-cover contact (Heim, 1878) or multistage deformation with a reactivation of pre-Alpine foliations as shear planes and ductile folding (Baltzer, 1888; Morgenthaler, 1921; Rohr, 1926; Mueller and Arbenz, 1938; Kammer, 1989). Although he had never been in the area, Lory (1874)

suggested as first the existence of a thrust plane above the inverted limb of the Pfaffenchopf sediment wedge, an idea which was revisited by Morgenthaler (1921). It was finally Labhart (1966) who locally recognized a two-stage Alpine deformation: first along the steep pre-Alpine fabrics followed by the evolution of a new moderately SE-dipping foliation with associated NW-directed thrusting.

Our new results clearly support Labhart's ideas, now naming his thrust-related structures as Pfaffenchopf phase (Berger et al., 2017; Herwegh et al., 2017). The fact that the steep old foliation (pre-Alpine/Handegg) rotates into the moderately SE-dipping Pfaffenchopf shear planes confirms Kammer's (1989) idea on a synchronous activity. In our view, however, the steep foliation already existed and was reactivated instead of being newly formed (see above).

As documented in Figures 4-6, 9a and 10, the Pfaffenchopf fault array probably reflects a major crustal-scale structure, which has not yet been recognized as such by previous studies. This structure is characterized by (i) the repetitive decameter-scale occurrence of Pfaffenchopf thrust planes over a vertical distance of at least 1500 m (Fig. 9) as well as (ii) the continuation of the Pfaffenchopf foliation until the village of Guttannen in the central Haslital (Fig. 4). Based on retro-deformation of the basement-cover contact, using the rigid Triassic dolomites in the cross-sections of Rohr (1926) as a marker horizon, we derive a minimum accumulated thrust-displacement over the exposed Pfaffenchopf fault array 1 of at least 1500 m (Fig. 9b). This estimate increases when we also consider shortening of the dolomites between the individual thrust planes (Fig. 9b). Finite strain is low at both the low and high altitude parts of the Pfaffenchopf fault array 1 but significantly enhances in its central part displaying a large-scale symmetric strain gradient (Fig. 9b). Kinematically, the

Pfaffenchopf shearing explains the progressive steepening of the basement-cover contact along the Aar Massif's northern rim due to a passive rotation as a function of increasing accumulated shear strain (Figs. 5a and 9a). Additionally, it also delivers a solution for today's complicated shape of the sediment wedges, as can be demonstrated by a retro-deformation of the Pfaffenchopf section (Fig. 11). Similar observations on basement-cover deformation are also described for the Western Alps by Bellahsen et al. (2012, 2014) and in a more general view by Lacombe and Bellahsen (2016). Originating from the only slightly extended passive continental margin with steep normal faults and down-stepping basement blocks towards the south (Figure 11a; see also Rohr, 1926), the tectonic preconditioning with a steep pre-Alpine foliation in the gneisses of the Innertkirchen-Lauterbrunnen zone and the steep normal faults provide mechanical discontinuities. They are reactivated during S-block-up reverse faulting of the Handegg phase bringing the basement-cover contact into progressively higher levels. Note that under these lower greenschist metamorphic conditions, it is mechanically impossible to fold the original gneisses in a ductile manner, as documented by the persistence of the consistently steep SE dipping old foliations in the basement rocks. Similar to observations in the Oisans-Belledonne ECMs (Bellahsen et al., 2012), new fault zones form but pre-existing normal faults are partly reactivated, too. This reactivation occurs probably due to the more pronounced shortening in the case of the Aar Massif and the stronger vertical uplift component. During later Pfaffenchopf shearing at even lower metamorphic conditions, the younger moderately SE-dipping shear planes form. Given the absence of substantial ductile deformation in these gneisses at such low temperatures, the Pfaffenchopf shear planes likely form by a combination of brittle deformation, fluid circulation, and enrichment by precipitation processes of ultrafine grained sheet

silicates as well as vein quartz (see above and Berger et al., 2017). As a consequence, the coarse-grained pre-Alpine gneiss microstructures become reduced in grain size and feldspars are altered during this lower greenschist facies metamorphic conditions. This results in fine-grained sheet-silicate-rich fault planes (phyllonites) and low-T quartz dynamic recrystallization microstructures (Fig. 6c). Hence, a deformation-induced chemical softening of the gneisses occurs. In this way, a mechanically weak network of steep and moderately SE-dipping Handegg and Pfaffenchopf planes evolves, allowing for a comprehensive NW-directed thrusting in the Pfaffenchopf fault array 1. This shearing also affects the originally steep limbs of the sediments in the Handegg phase syncline (Figs. 11b and c) resulting in a transposition from a subvertical into a subhorizontal axial plane, expressed in the current recumbent-fold-like appearance (Figs. 7 and 9c). In contrast to the semi-brittle deformation behavior and associated chemically-induced strain softening in the gneisses, the calcite-dominated Jurassic and Cretaceous limestones in the core of the Pfaffenchopf wedge experienced pronounced ductile deformation as visible by the ductile folds (Fig. 7). Contrastingly, the Triassic dolomites represent an exception because deformation temperatures below 400°C induced dissolution-precipitation accommodated brittle to semi-brittle deformation (e.g. Delle Piane et al., 2008; Davis et al., 2008). Instead of pure ductile folds, therefore imbricates and kink-fold type deformation structures (Figs. 6a and 7) evolved making them ideal passive markers for the performed tectonic restorations (see also Bellahsen et al., 2012; Mair et al., 2018; Nibourel, 2019).

Given the newly established importance of the Pfaffenchopf fault array 1 at the surface, the question about its subsurface continuation with depth and its lateral extension along the SE-dipping fault planes arises. With respect to the latter, the

manifestation of the foliation and small-scale fault planes of the Pfaffenchopf phase until south of Guttannen suggests a continuous subsurface occurrence to at least this geographic location (Fig. 4). By projecting the surface based geometry and associated uncertainties to the SE, Baumberger (2015) hypothesizes a lateral southward continuation of the Pfaffenchopf fault array 1 at depth of the plutonic rocks of the southern Aar Massif. Following this concept, we speculate that the fault array 1 may even continue underneath Grimsel Pass, where it would then mechanically interact with the crustal-scale Grimsel Pass shear zone (Figs. 12d and 13d).

On a crustal-scale, reflection seismic images from the NRP 20 project (Deep structure of the Alps; Pfiffner et al., 1997) provide insights into the continuation of the Pfaffenchopf structures with depth in the northern domain. Based on the observed offset of the basement-cover contact at the junction from the tectonically 'undisturbed' SE-dipping European plate and the displaced and NW-dipping Aar Massif, Pfiffner et al. (1997) distinguished a basal SE-dipping detachment of the Aar Massif (Figs. 13.1-12, 13.1-13 and 13.1-14 of Pfiffner et al., 1997). They interpreted an additional offset of the basement-cover contact in between the basal detachment and the Pfaffenchopf fault array 1. Moreover, some basement internal seismic reflections may also point to the subsurface occurrence of further Pfaffenchopf structures. Hence, NW-directed thrust kinematics, dip angles as well as dip directions of these structural features are all similar to those of the Pfaffenchopf structures observed at the surface. We therefore suggest a periodic reappearance of Pfaffenchopf fault arrays with depth (Figs. 12c,d and 13c,d) and interpreted two additional arrays (Pfaffenchopf fault array 2 and 3), each associated with the previously suggested subsurface displacement zones of Pfiffner et al. (1997). Except of the distinctive offset along the basal detachment, their expression in the seismic reflection data

however is weak, which is probably due to thin and relatively widely spaced individual fault planes, as seen in surface outcrops (Figs. 4, 6, and 7). Again, the continuation of the fault planes towards the south remains speculative (see question marks in Figure 12d). In Figure 13d, we present a possible southward continuation of these arrays, intersecting at depth with the subvertical dextral Grimsel Pass shear zone. Although remaining speculative, current hydrothermal fluid circulation along the Grimsel breccia fault (Belgrano et al., 2016; Egli et al., 2018), as brittle successor of this ductile shear zone, indicates a present day continuation to depths of at least 10 kilometers (Diamond et al., 2018).

Horizontal Shortening and Vertical Rock Uplift Components

We follow the definition of England and Molnar (1990) for the terms “rock uplift” and “exhumation”. Rock uplift describes the displacement of a rock volume with respect to Earth’s geoid, driven by tectonic and/or buoyancy forces. Rock uplift does not imply any changes in surface topography. Contrastingly, the displacement of rocks with respect to Earth’s surface is referred to as ‘exhumation’. Hence, rock uplift and exhumation rates may differ (e.g. vertically growing mountain chains), but they can also coincide in the case of an existing balance between erosion and rock uplift forces. According to Schlunegger and Kissling, (2015), the mean elevation of the Alps did not change over the last 22 Ma, a finding which is also supported by Campani et al. (2012). This is exactly the time interval of the uplift and exhumation of the Aar Massif’s basement rocks from their maximum burial depth to their present-day surface exposition. As a first order approximation, we therefore consider rock

uplift to be similar to exhumation, which is also in line with Bernet et al. (2001) and von Hagke et al. (2014b).

By combining estimates of peak metamorphic conditions, geometric considerations, and the presented ZFT and AFT data, a reconstruction of the total rock uplift along the NNW-SSE transect as well as vertical rock uplift increments for the temperature intervals T_{max} >300°C, 300-110°C, and <110°C can be obtained (Fig. 10). While in the northern domain of the Aar Massif, peak metamorphic conditions rise steeply from 250°C to about 440°C (N to S), the southern domain including the adjacent northern rim of the Gotthard nappe shows only a slight temperature increase of about 50°C (T_{max} = 490°C, Oliot et al., 2010). Note that these peak temperatures agree well with Raman thermometry performed on carbonaceous material of Mesozoic sediments, which are present along the northern and southern rim but unfortunately eroded in between in the case of the central Aar Massif (Erne, 2014; Mair et al., 2018; Nibourel, 2019). Assuming a geothermal gradient of 25°C/km, this corresponds to maximum burial depths of about 18-20 kilometers for the southern part, which is in good agreement with the estimated pressure of 6.5 kbar from Goncalves et al. (2012). The northern domain was at maximum depths of about 10 kilometers. Converting now the ZFT data of 13-12 Ma with the T_c at 300°C/240°C into depth, and subtracting the maximum depth at T_{max} at 22-20 Ma yields information on the vertical uplift component during the Handegg phase deformation (22-13 Ma). The resulting red arrows of Figure 10 reveal a differential uplift for the Handegg phase reverse faulting along a NNW-SSE profile. A constant vertical uplift component of 6-9 km (ZFT T_c 300°C) or 8-11 km (ZFT T_c 240°C) exists for the southern domain, followed by a continuously decreasing vertical uplift component towards the north of the section. These constraints are in well agreement with a stage of rapid decompression under

nearly isothermal conditions during this time interval (Challandes et al., 2008; Diamond and Tarantola 2015; Herwegh et al., 2017 see their supplementary Figure 3), meaning that heat was transported upward with the rising rock masses.

The dark blue/grey and bright blue stippled lines in Figure 10 correspond to the depth conversion of the correlating ZFT (13-12 Ma) and AFT (8-5 Ma) age intervals, respectively. It becomes evident that owing to thrusting along the exposed Pfaffenchopf fault array 1 another 6-7 km (ZFT T_c 300°C) or alternatively 4-5 km (ZFT T_c 240°C) of vertical uplift are homogeneously accommodated within the entire hanging wall between 13 Ma and 5 Ma (Fig. 10, dark blue arrows).

The remaining 3-4 km of vertical uplift must again be accommodated in a homogeneous manner over the entire exposed Aar Massif within the last 5 Ma (see AFT line for 110°C isograde in Fig. 10). Time-integrated deformation along the progressively developing Pfaffenchopf fault arrays results in cumulative vertical en-bloc uplift of the basal thrust's hanging wall by 6-9 km/8-11 km during the timer interval 13-0 Ma (Figs. 12 and 13). Hence, at that time, the Pfaffenchopf thrust system as a large-scale crustal ramp represented the tectonically active boundary. Note that toward the north, Pfaffenchopf thrusting translates into the Subalpine Molasse, where synchronous imbrication takes place (Figs. 12d and 13d; see also von Hagke et al., 2012, 2014b; Mock, 2017; Mock et al., 2019) being mechanically preferentially accommodated in shale-rich lithologies (von Hagke et al., 2014a; Mock et al., 2019). The late Pfaffenchopf thrusting probably also triggers the formation of the Gadmen faults (Figs. 7, 12, and 13). These young cross-cutting faults might compensate for relative displacements (N-block up) in the hanging wall parts while ramping the entire Aar Massif upward along the deeper acting fault arrays 2-3.

We obtained estimates on the amount of total horizontal shortening by retro-deforming the NNW-SSE section in Figure 13. We chose a northern and a southern pin line in the European basement not affected by the Aar Massif's exhumation and at its southern contact to the Gotthard nappe, respectively (Fig. 13). For the Handegg phase, we estimated an average horizontal shortening of 15% (Fig. 13b). While Oberaar phase dextral strike- to oblique-slip faulting removed material out of the section and probably had a small effect on both vertical and horizontal NW-SE movement only, synchronously active Pfaffenchopf phase thrusting contributed substantially to shortening. It accommodated additional 20% and 24% of horizontal shortening for the time intervals 13-8 Ma and 8-0 Ma, respectively (Fig. 13c,d).

Rock Uplift and Exhumation Rates

In the following, we combine the above-presented ZFT and AFT derived time constraints with structure-based geometrical data. For the time interval of Handegg phase activity (22-20 Ma to 13 Ma), we calculated average rock uplift rates of 0.65-1.3 km/Myr (ZFT T_c = 300°C) or 0.9-1.55 km/Myr (ZFT T_c = 240°C) for corresponding estimated vertical components of 6-9 km or 8-11 km, respectively, for the southern domain of the Aar Massif (Figs. 10 and 14). To the north, these values remain stable until the central part of the Haslital before decreasing then steadily northward. Exhumation rates (based on cooling rates) from the Gotthard nappe, which exhumes together with the Aar Massif (see Figs. 12 and 13 as well as Glotzbach et al., 2010), correlate well in terms of timing and range of 0.8-1.4 km/Myr (Fox et al., 2016, see their Fig. 12). Hence, a balance between rock uplift processes and erosion processes can be postulated during Handegg phase activity. Glotzbach et al. (2010)

derived somewhat slower rates of 0.7±0.2 km/Myr between 16 and 14 Ma for domains of the Aar Massif located farther to the east, which is in excellent agreement with a currently postulated eastward migration of exhumation in the Aar Massif (Nibourel, 2019).

For the time interval 13-5 Ma, uplift rates of 0.75-0.9 km/Myr (ZFT T_c = 300°C) or 0.5-0.65 km/Myr (ZFT T_c = 240°C) result. During the synchronous strain partition of Oberaar strike-slip faulting in the S and Pfaffenchopf thrusting only the latter substantially contributes to the vertical uplift rate (Fig. 14). In the southern Aar Massif, thrusting induced rock uplift of the Pfaffenchopf phase is slower compared to rock uplift during vertical tectonics of the Handegg phase (Figs. 10 and 14).

Glotzbach et al. (2010) postulated a constant exhumation rate of ~0.5 km/Myr since ~14 Ma with a slight increase to ~0.7 km/Myr for the time intervals of 16-14 and 10-7 Ma. While the first interval correlates with the termination of the vertical Handegg phase tectonics, the latter occurs during early Pfaffenchopf thrusting along the fault arrays 1 and 2. We are however not able to resolve this late pulse in terms of potential changes in rock uplift owing to a too low temporal resolution of our dataset.

During late Pfaffenchopf thrusting (5-0 Ma), rock uplift shows rates of 0.6-0.8 km/Myr (Fig. 14). Several thermochronological studies suggest a decrease in modeled exhumation rates from 0.7 km/Myr to 0.3-0.5 km/Myr during the last 5 Ma (Reinecker et al., 2008; Glotzbach et al., 2010; Valla et al., 2012; von Hagke et al., 2014b; Fox et al., 2016) with renewed increase owing to glacial rebound for the last 1.2 Ma (Haeuselmann et al., 2007). Note that the time integration of our data over the past 5 Ma blurs the effect of the slowing exhumation rates and the subsequent increase owing to glacial carving after 1 Ma (see below). Present-day surface uplift rates, taken from high-precision leveling data (Schlatter, 2007; see also swisstopo,

www.map.geo.admin.ch), indicate a relative increase with respect to the reference point at Aarburg (Northern CH) from 0.15 km/Myr (Subalpine Molasse) to 0.7 km/Myr (Southern Aar Massif; see Figs. 10 and 14). Considering the absolute uplift of 0.8 mm/a of this reference point (Brockmann 2018), even a total uplift of 0.95-1.6 km/Myr would result for the study area. The relative N-S increase in rock uplift rates correlates well with the slightly tilted ZFT (13-12 Ma) and AFT (13-5 Ma) iso-age curves (see Fig. 10) and is in line with considerations in the western Aar Massif (Reinecker et al., 2008, their Figure 10). Rahn et al. (1997) observed a similar northward dip direction in the Helvetic Alps of eastern Switzerland, which they attributed to a rotation of the iso-age curves by young movements.

Thermochronological studies from literature concur on similar rates of rock uplift and exhumation thus suggesting a balance between tectonic rock uplift and erosion processes until the Mid-Pleistocene revolution (see Mudelsee and Stattegger, 1997; Campani et al., 2012; von Hagke et al., 2014; Schlunegger and Kissling, 2015). For the following period of glaciation cycles, the temporal resolution of our data is not sufficient to document possible tectonic signals associated with the increase in erosion rates for the last 1-0.8 Myr (Haeuselmann et al., 2007; Reinecker et al., 2008; Glotzbach et al., 2008; Sternai et al., 2012; Fox et al., 2016). Despite this young erosional overprint, it is probably the combination of structural inheritance and the remaining stress states of the late collisional stage, which still controls neotectonic activity and may explain the differences in the present-day deformation regimes between the Northalpine foreland and the adjacent Alpine front (see Houlié et al., 2018).

The Aar Massif in Comparison to Other ECMs

Considering mantle dynamics as a key driving force for the uplift of the Aar Massif (see below) in early Miocene times raises the question for comparable effects during Alpine inversion of the former European passive continental margin. Since ECMs align all along the outer rim of the Western and Central Alpine arc (Fig. 1), their exposed basement rocks can be considered to be in a comparable tectonic position; at least until east of the Aar Massif, where no more ECMs are exposed in the Central Alps. In the Western Alps, reconstructions of the Mesozoic rifting structures reveal the inversion of the passive continental margin by an increasing shortening from SW to NE (Bellahsen et al., 2014). In the case of the (south-)western massifs (Oisans, Grand-Rousse, Belledonne, Argentera-Mercantour, and Pelvoux) moderate Alpine inversion mainly took place by horizontal shortening based on a combination of thin- and thick-skinned tectonics in a dominantly thrust-related environment (e.g. Lacombe and Mouthereau 2002; Bogdanoff et al., 2000; Bellahsen et al., 2012; Bellahsen et al., 2014; Boutoux et al., 2014; Lafosse et al., 2016). Here, newly formed Alpine low-angle shear zones accommodated internal shortening under peak metamorphic isothermal conditions for a period of up to ~10 Myr (34-25 Ma; see Bellahsen et al., 2014; Bellanger et al., 2015 and references therein) before becoming uplifted and exhumed by thrust ramps after 20-15 Ma (Lacombe and Mouthereau, 2002; Bellahsen et al., 2012, 2014; Bellanger et al., 2015; Boutoux et al., 2016). With <20%, however, the overall shortening in these western ECMs is approximately half of that estimated for the Aiguilles Rouges/Mont Blanc Massif and the Aar Massif sections (see Table 1 in Bellahsen et al., 2014).

As already stated by Bellahsen et al. (2014), the Mont Blanc and the southern central Aar Massif share a similar retrograde P-T-t evolution (Fig. 15) with an early stage of isothermal decompression from 22-18 Ma, followed by more pronounced cooling

afterwards (for detailed cooling paths see Leloup et al., 2005; Boutoux et al., 2016; Challandes et al., 2008; Diamond and Tarantola 2015). Steep SE-dipping early shear zones with down dip lineations and reverse faulting sense of shear occur in both massifs (see Rolland et al., 2008; Rolland et al., 2009; Wehrens et al., 2016, 2017). However, while in the Aar Massif they are dispersively distributed, they are probably more localized and restricted along two major crustal-scale high strain zones in the Mont Blanc Massif (Faille du Midi and the Mont Blanc shear zone; see Bellier et al., 1988; Rossi et al., 2005; Rolland et al., 2008; Egli and Mancktelow, 2013). The timing of their activity, however, seems to overlap partially (radiometric age determinations for Mont Blanc: 29-22 Ma, Cenki-Tok et al., 2013; Rolland et al., 2008; Aar Massif: 22-17 Ma, Challandes et al., 2008; Rolland et al., 2009). While differential uplift along the densely spaced steep reverse shear zones promoted differential vertical uplift and cooling in the Aar Massif (Herwegh et al., 2017), thermal modeling of Boutoux et al. (2016) suggests that shearing along the Mont Blanc shear zone occurred under isothermal conditions until 18 Ma, without major cooling. In the latter, dextral transpression, reactivating the major faults as well as more distributed dextral strike-slip movement, at the northern and southern rim of the massif led to further exhumation by accentuating the massif in a ‘pop-up’-style with top to NW and shearing in the Chamonix zone in the NW as well as, locally, back-thrusting (Mont Blanc back-thrust at 16 Ma; Rolland et al., 2008) and back-folding / back-steepening at the SE rim of the massif (see also Leloup et al., 2005; Rolland et al., 2008; Egli and Mancktelow, 2013; Egli et al., 2017) until 9.5 Ma (Egli et al., 2017).

Peak metamorphic conditions at 20-18 Ma and subsequent cooling are rather similar for the Aiguilles Rouges and the northern Aar Massif (Fig. 15; Boutoux et al., 2016;

Herwegh et al., 2017). Steep reverse faults are active in both cases between 18-14 Ma (Egli et al., 2017; Berger et al., 2017), probably associated with an onset of basal thrusting in the case of the Aiguilles Rouges Massif at 15 Ma (Egli et al., 2017). The fact that no massif-internal offsets of ZFT (Aar: 13-12 Ma, this study; Mont Blanc: 13-12 Ma, Glotzbach et al., 2011) and AFT (Aar and Aiguilles Rouges: 8-5 Ma, this study and Boutoux et al., 2016; Mont Blanc: <4 Ma, Glotzbach et al., 2008) ages occur, suggests 'en-bloc' rock uplift and cooling above such basal ramps since at least 13-12 Ma. This uplift occurs under still transpressive conditions as indicated by simultaneous strike-slip activity along the Rhone-Simplon line (Campani et al., 2010; Egli and Mancktelow, 2013; Egli et al., 2017) and the Grimsel Pass shear zone / Grimsel Breccia fault (Rolland et al., 2009; Hofmann et al., 2004; Wehrens et al., 2017; Belgrano et al., 2016; Egli et al., 2018). Also the recent relative uplift patterns correlate remarkably well between the Aar and Aiguilles Rouges / Mont Blanc sections (compare section 2 in Figure 8 in Lacombe and Mouthereau (2002) with inset on bottom of Figure 10 of this study). Hence, since 13-12 Ma, the large-scale deformation style correlates very well among the different ECMs (see data this study and Lacombe and Mouthereau, 2002; Bellahsen et al., 2012, 2014; Bellanger et al., 2015; Boutoux et al., 2016). The more pronounced vertical exhumation after peak metamorphic conditions, horizontal shortening as well as higher topographic reliefs of the Mont Blanc and southern Aar Massif, however, clearly differ in comparison to other ECMs. As will be outlined below, these differences might be attributed to a combination of variations in the shape of the former European passive continental margin before collision, its entrance into the subduction channel, and the subsequent interplay between lithospheric and surface processes.

Geodynamic Scenario of the Late-Stage Alpine Continent-Continent Collision

From a plate tectonics point of view, the formation of the Central Alps comprises a more than 50 Myr-long lasting geological history, with closure of the Tethys Ocean (Penninics) by subduction under the Adriatic plate (e.g. Trümpy, 1960; Tricart, 1984; Schmid et al., 1996; Stampfli et al., 2002; Pfiffner, 2009; Handy et al., 2010; Schmid et al., 2017). A major change occurred at the onset of continent-continent collision at ~35 Ma (Rosenberg and Kissling, 2013; Rosenberg et al., 2015), when the slab of the subducting lithosphere broke off (Blankenburg and Davies, 1995). The drastically reduced slab pull forces, resulted in significant rock uplift in the internal Alps, which was at least in parts counterbalanced by surface erosion manifested by a transition from former Flysch deposits in under-filled to Molasse sedimentation in overfilled foreland basins north and south of the Alps (e.g. Sinclair and Allen, 1992; Lihou and Allen, 1996). The north-Alpine Molasse sediments also comprise erosion products of the Austro-Penninic-Helvetic nappe stack being eroded during the rise of the Aar Massif (Schlunegger and Kissling, 2015 and references therein). For the time interval from oceanic slab breakoff at ~35 Ma until today there exist two opposing geodynamic models: (1) The 'Adria push' model evolved out of pre-plate tectonics kinematic concepts (e.g. Argand 1916; Staub 1924) and geophysical evidence gained in the 1990ies from the NRP 20 seismic survey and suggests indentation of the Adriatic lithospheric mantle into the remnants of the European slab (e.g. Schmid et al., 1996, 2017; Pfiffner et al., 1997; Schmid and Kissling, 2000). Consequently, shortening between Europe and Adria evolved, which is manifested by fold-and-thrust tectonics of the Helvetic nappes, the Aar Massif, the Subalpine Molasse as well as the Jura mountains. (2) Recently, an opposing 'orogeny slab rollback model' in the sense of a slab steepening or slab retreat has been suggested (Kissling 2008; Fry et al.,

2010; Singer et al., 2014; Schlunegger and Kissling, 2015; Herwegh et al., 2017; Kissling and Schlunegger, 2018). Schlunegger and Kissling (2015) and Kissling and Schlunegger (2016) question the physical driving forces of the 'Adria push' model for several reasons, among which the paleographically stable position of the European plate since Cretaceous times (Torsvik et al., 2012) as well as the remaining short European slab during the late-stage collision are particularly important. These two points argue against the capability of the European plate to perform slab pull induced subduction under the Adriatic plate. Alternatively, rollback of the remaining European slab is suggested, leading to lower crustal detachment (Fry et al., 2010) and subsequent buoyancy-driven rock uplift of middle to upper crustal rocks, which is accompanied by intense surface erosion (Schlunegger and Kissling, 2015). Note that rollback of the remnant of the European slab is in this context a limited version of the classical rollback process with its typical backarc extension as originally proposed by Royden (1993).

Based on the geographical position as well as the aforementioned deformation structures and the exhumation history, the Aar Massif provides key information for a discussion about the two opposing models. In this light, we revisit the originally suggested evolution scenarios of the Aar Massif presented in the introduction (Fig. 2). The simply buoyancy-driven-uplift model without compression is not in agreement with the deformation structures described in previous and the present studies and the fault-bend-fold model has many similarities with the pure-shear model in terms of kinematics, mechanics and geometry. We therefore focus the subsequent discussion on three main models: (1) pure-shear/buckle-fold, (2) antiformal-imbricate-stack, and (3) multistage block-extrusion model (Fig. 16). Both the (1) pure-shear/buckle-fold, and the (2) antiformal-imbricate-stack model are monophasic and rely on the 'Adria

push' scenario requiring a basal detachment above which middle to upper crustal rocks of the Aar Massif can be thrust northward and thickened. Crustal thickening in the pure-shear/buckle-fold model (Fig. 16a; picking up concepts of Choukroune and Gapais, 1983; Marquer, 1990; Burkhard, 1990, 1999) is accommodated by passive bending of the basement-cover contact into a large-scale upright fold and horizontal shortening in the basement. This model would explain the steep orientation of Handegg phase shear zones and the resulting flattening component. In theory, the intensity of the latter should increase underneath the 'hinge' of the buckle fold instead of its southern margin, as is the case in reality. Moreover, this model cannot explain the significant peak metamorphic N-S gradient across the Aar Massif. The crustal thickening in the case of the alternative antiformal-imbricate-stack model (Fig. 16b; modified after Burkhard, 1990, 1999) occurs by the piling up of imbricates. According to theory, they evolve at a shallow angle (~30°) in the active frontal part and subsequently steepen towards the south with progressive shortening, correlating with the observed fault zone orientations in the southern Aar Massif. In this model, however, considerable displacement between the individual imbricates would be required. Accordingly, we would expect deep sediment wedges being pervasively distributed over the entire Aar Massif transect and jumps in peak metamorphic isogrades across the fault zones generating the overall N-S peak metamorphic gradient. As mentioned above, this is not the case (see also Nibourel et al., 2018, Nibourel, 2019; Schneeberger et al. 2017). Given the shortcomings of both 'Adria push' related models, the block-extrusion model presents an alternative end-member solution (Fig. 16c). It comprises parts of the previous models but additionally integrates the possibility to exhume rock volumes not only by horizontal compression but also by a strong vertical component, as in fact is also the case by the buoyancy-

driven-uplift model (Fig. 2). In contrast to the previous models, block-extrusion requires a two-stage deformation as observed in the field and summarized in the following.

Pre-22 Ma horizontal tectonics generates the Upper Helvetic (Drusberg and Axen nappe) and Lower Helvetic (Infrahelvetic) nappes/imbricates, followed by the transport of the Gotthard nappe onto the southern parts of the future Aar Massif (Figs. 12a and 13a; for details we refer to Pfiffner et al., 2011; Berger et al., 2011; Mair et al., 2018; Nibourel, 2019). At the time these tectonic units are emplaced, the Aar Massif is still part of the European continental middle to upper crust, which becomes involved in the progressing continent-continent collision. Beginning at about 22 Ma, the Aar Massif detached from the lower crust and lithospheric mantle of the European plate and started to exhume differentially along the simultaneously acting steep normal and reverse faults during the Handegg phase (22-13 Ma, Figs. 12b and 13b), also explaining the metamorphic N-S gradient with its significant vertical component of 8-10 km in the south and its gradual decrease to a few 100 m in the north (Fig. 10). Such steep shear zones with a dominant reverse fault component cannot form in an overall stress regime with a horizontal maximum stress, as implied by the 'Adria push' scenario. Instead, Herwegh et al. (2017) explained the originally steep and frequent Handegg shear zones by a NW-SE trending, but non-horizontal principal stress direction, which allows for both an initialization of Handegg reverse shearing along steep fault planes as well as a NW oriented upward mass transfer vector exhuming higher grade rocks in the south compared to the north (Figs. 12b and 13b). These physical aspects are linked to a buoyancy-driven model, which is most likely caused by aforementioned lithospheric mantle rollback (Kissling, 2008; Kissling and Schlunegger, 2018; Singer et al., 2014; Schlunegger and Kissling, 2015; Fry et al.,

2010) manifested by a steepening of the remaining slab of the European lithosphere and a delamination in the sense of a mechanical decoupling (see Nelson, 1992) of the light continental upper/middle crust from the denser lower crust and lithospheric continental mantle (Herwegh et al., 2017). The proposed hypothesis of delamination somewhere in the lower crust is based on geophysical observations such as a combination of (i) ambient noise tomography showing an orogen parallel anisotropy in the European crust underneath the Alps (Fry et al., 2010), and (ii) seismic p-wave tomography (Diehl et al., 2009) and (iii) combined refraction seismics-gravity modeling (Holliger and Kissling, 1992), which shows an accumulation of lower crustal material on mid-crustal level (see Figs. 3 and 5 in Herwegh et al., 2017). As a consequence of delamination, gravitational slab-pull and negatively buoyant forces imposed by the European lithospheric mantle and counterbalancing the positively buoyant forces exerted by the less dense European middle to upper crust and the overlying rocks of the accretionary complex, diminish (Herwegh et al., 2017). Consequently, positive buoyancy forces lead to a reactivation, as well as the formation of new, subvertical discontinuities within the Aar Massif allowing for its exhumation along these steep Handegg phase faults. This model of vertical tectonics explains both the differential, northward decreasing, uplift of the Aar Massif (Fig. 10) owing to progressive migration of the active deformation front towards the north (Figs. 12b and 13b) as well as the observed southward increase in deformation intensity (including flattening; Choukroune and Gapais, 1983; Wehrens et al., 2017). Moreover, it agrees with the freezing of ZFTs at about 22-16 Ma in the northern Aar Massif (Figs. 5b and 10), when exhumation during Handegg phase faulting brought these rocks below 240°C/300°C (Figs. 5 and 13b). Note that also during this phase of buoyancy-driven vertical tectonics, the steepening of the European lithospheric slab

still attracts the Adriatic plate by suction forces (Kissling and Schlunegger, 2018), thus maintaining an overall compressional regime. Contemporaneously with this rock uplift dynamics, erosional unloading at the surface (Willet et al., 2010, Schlunegger and Kissling, 2015) yields a positive feedback for the exhumation of the Aar Massif. The process of European slab rollback probably slows down remarkably at about 20 Ma, manifested by the fixed axis of the Northalpine foreland basin without any further northward propagation (von Hagke et al., 2012; Schlunegger and Kissling, 2015). However, the crustal scale stress regime, lower crustal delamination processes, and buoyancy-driven rock uplift still persists. With progressive rock uplift and associated surface erosion, the positive buoyancy-driven component reduces between Handegg and Pfaffenchopf/Oberaar phases, as manifested by decreasing rock uplift rates (Fig. 14). Owing to persisting compressional forces, therefore a gradual transition from vertical to horizontal tectonics occurs towards 13 Ma (Herwegh et al., 2017; see also Wehrens et al., 2017). As a consequence, strain strongly partitions between the southern and northern domain of the Aar Massif (Figs. 12c and 13c). While Handegg phase reverse faulting progressively changes to Oberaar phase dextral strike- and oblique-slip shearing along the Grimsel Pass shear zone in the south (Rolland et al., 2009; Belgrano et al., 2016; Wehrens et al., 2017; Egli et al., 2018), the Pfaffenchopf fault arrays evolves underneath the Aar Massif and accommodates NW-directed thrusting (Fig. 13c).

Buoyancy-driven vertical uplift (extrusion) of upper to mid-crustal crystalline basement rocks might also present a valuable concept for the early rock uplift stage and associated isothermal decompression of the Mont Blanc Massif (22-18 Ma). Important for the onset of potential vertical extrusion of basement rocks is the delamination from the lithospheric mantle. Whether this occurs by a slab rollback

process in the sense describe above or solely by a transpressional upward movement (e.g. Leloup et al. 2005; Egli and Mancktelow, 2013) without a slab dynamic component remains an open research question, which might be addressed in future by geodynamic modeling approaches. Independent of the geodynamic outcome, delamination-triggered buoyancy-driven vertical extrusion under dextral compression could indeed be a potential geodynamic scenario for the onset of early stages of exhumation in the Mont Blanc Massif, which would benefit from activity of the steep early reverse fault zones therein (e.g. Mont Blanc shear zone, Faille du Midi).

Conclusion

The Haslital transect provides temporally and spatially highly resolved information on the exhumation history of the central Aar Massif and its adjacent units of the Helvetic nappes and the Subalpine Molasse.

Based on our new data, which resolves the Aar Massif's internal deformation structures, their kinematics, and timing, we present a new geodynamic model for the massif's exhumation history. While comprising parts of the classical models (see introduction and Burkhard, 1990, 1999), it describes a multistage evolution of a sequence of (i) horizontal – (ii) vertical – (iii) horizontal tectonics:

(i) The transition from thin-skinned thrust tectonics (Kiental phase) to imbricate-type thick-skinned tectonics reflects the progression of deformation along the more to the less extended parts of the European passive continental margin.

(ii) As a consequence of counteracting negative slab pull forces and positive buoyancy forces exerted by the lighter middle and upper crust, delamination of the future Aar Massif occurred. Driven by buoyancy forces and additionally

supported by erosional unloading (e.g. Willet et al. 2010; Fox et al., 2012), the delaminated mid- to upper-crustal block extruded subvertically along the steep Handegg phase shear zones (22-13 Ma).

(iii) After the slab rollback of the European plate decelerated, geodynamically there still remained the plate tectonic compressional forces. Vertical tectonics (see above) gradually translated again into a horizontal tectonic deformation style. This resulted in a large-scale strain partitioning between dextral strike to oblique-slip shearing in the south (Oberaar phase) and northward migration of the entire Aar Massif along the subsequently down-stepping Pfaffenchopf thrust fault arrays (Pfaffenchopf phase). In this way, the latter acted as large-scale crustal ramps enabling an en-bloc exhumation of the entire Aar Massif.

The tectonic sequence from (i) to (iii) is controlled by plate driving forces and the role of the European lithospheric mantle (Kissling, 2008; Herwegh et al., 2017; Kissling and Schlunegger, 2018). The combination of thermochronometric and structural data allows a reconstruction of the buoyancy-driven vertical uplift component from 22-13 Ma with uplift rates of up to ~1.4 km/Myr (Figs. 10 and 14). The northward decreasing differential uplift speaks against an en-bloc exhumation but underlines the importance of the steep pervasive Handegg faults in accommodating this differential vertical uplift. Subsequent thrust-related rock uplift results in slower uplift rates (~0.6 to 0.8 km/Myr, Fig. 14).

In sum, it is the tectonic forcing of the succession of steep Handegg faulting and Pfaffenchopf thrusting in combination with surface erosion, which is responsible for (i) the exhumation of basement rocks to altitudes of up to >4000 m and (ii) the steep inclination of the basement-cover contact. This provides the base for preferential

erosion along the northern rim of the Aar Massif resulting in its today's impressive morphological expression (Fig. 3).

Acknowledgements

We acknowledge funding by the Swiss National Science Foundation (project 20002-1132196) as well as Midland Valley (PETEX) for providing us access to the academic license of MOVE. The manuscript greatly benefited from careful review and constructive suggestions by Olivier Lacombe, Christoph von Hagke and two anonymous reviewers.

Data Availability

Data used in this paper are either available in the cited papers or in the data files attached to this manuscript.

References

Abrecht, J. 1994 J. Abrecht
Geologic units of the Aar Massif and their pre-Alpine rock associations: a critical review. The pre-Alpine crustal evolution of the Aar, Gotthard and Tavetsch massifs.
Schweizerische Mineralogische und Petrographische Mitteilungen, 74 (1994), pp. 5-27

Abrecht and Schaltegger 1988 J. Abrecht, U. Schaltegger
Aplitic intrusions in the central Aar Massif basement - geology, petrography and rb-sr data
Eclogae Geologicae Helvetiae, 81 (1988), pp. 227-239

Baltzer (1888) A. Baltzer

Das Aarmassiv (mittlerer Theil), nebst einem Abschnitt des Gotthard-Massivs enthalten auf Blatt XIII, von Dr. A. Baltzer
Schmid, Francke und C°

Bambauer et al. 2009 H.U. Bambauer, M. Herwegh, H. Kroll
Quartz as indicator mineral in the Swiss Alps: the quartz recrystallization isograd in the rock series of the northern Aar massif
Swiss Journal of Geosciences, 102 (2009), pp. 345-351

Baumberger 2015 R. Baumberger
Quantification of lineaments: Link between internal 3D structure and surface evolution of the Hasli valley (Aar massif, Central alps, Switzerland)
PhD thesis, Bern University (2015), 132 pp.

Baumberger et al. (in press) R. Baumberger, M. Herwegh, E. Kissling
Remote sensing and field data based structural 3D modelling (Haslital, Switzerland) in combination with uncertainty estimation and verification by underground data
AGU Monographs (in press)

Bauville and Schmalholz, S.M. 2017. A. Bauville. S.M. Schmalholz
Tectonic inheritance and kinematic strain localization as trigger for the formation of the Helvetic nappes, Switzerland
Swiss Journal of Geosciences, 110 (2017), pp. 523-534

Belgrano et al. 2016 T.M. Belgrano, M. Herwegh, A. Berger
Inherited structural controls on fault geometry, architecture and hydrothermal activity: an example from Grimsel Pass, Switzerland
Swiss Journal of Geosciences, 109 (2016), pp. 345-364

Bellahsen et al. 2012 N. Bellahsen, L. Jolivet, O. Lacombe, M. Bellanger, A. Boutoux, S. Garcia, F. Mouthereau, L. Le Pourhiet, C. Gumiaux
Mechanisms of margin inversion in the external Western Alps: Implications for crustal rheology
Tectonophysics, 560 (2012), pp. 62-83

Bellahsen et al. 2014 N. Bellahsen, F. Mouthereau, A. Boutoux, M. Bellanger, O. Lacombe, L. Jolivet, Y. Rolland
Collision kinematics in the western external Alps
Tectonics, 33 (2014), pp. 1055-1088

Bellanger et al. 2014 M. Bellanger, N. Bellahsen, L. Jolivet, T. Baudin, R. Augier, A. Boutoux
Basement shear zones development and shortening kinematics in the Ecrins Massif, Western Alps
Tectonics, 33 (2014), pp. 84–111

Belliere 1988 J. Belliere
On the age of mylonites within the Mont Blanc massif
Geodinamica Acta, 2 (1988), pp. 13–16

Berger et al. 2016 A. Berger, I. Mercolli, M. Herwegh, E. Gnos
Geological map of the Aar Massif, Tavetsch and Gotthard nappes 1: 100000
Swisstopo, Geological special map 129

Berger et al. 2011 A. Berger, S. Schmid, M. Engi, R. Bousquet, M. Wiederkehr
Mechanisms of mass and heat transport during Barrovian metamorphism: A discussion based on field evidence from the Central Alps (Switzerland/northern Italy)
Tectonics, 30 (2011), doi:10.1029/2009TC002622

Berger et al. 2017 A. Berger, P. Wehrens, P. Lanari, H. Zwingmann, M. Herwegh
Microstructures, mineral chemistry and geochronology of white micas along a retrograde evolution: An example from the Aar massif (Central Alps, Switzerland
Tectonophysics, 721 (2017), pp. 179-195

Bernet 2001 M. Bernet, M. Zattin, J.I. Garver, M.T. Brandon, J.A. Vance
Steady-state exhumation of the European Alps
Geology, 29 (2001), pp. 35-38

Bernet 2009 M. Bernet
A field-based estimate of the zircon fission-track closure temperature
Chemical Geology, 259 (2009), pp. 181-189

Blanckenburg and Davies 1995 F. Blanckenburg, J.H. Davies
Slab breakoff: a model for syncollisional magmatism and tectonics in the Alps
Tectonics, 14 (1995), pp. 120-131

Bogdanoff et al. 2000 S. Bogdanoff, A. Michard, M., Mansour, G. Poupeau
Apatite fission track analysis in the Argentera massif: evidence of contrasting denudation rates in the External Crystalline Massifs of the Western Alps
Terra Nova, 12 (2000), pp. 117-125

Boutoux et al. 2014 A. Boutoux, N., Bellahsen, O., Lacombe, A., Verlaguet, F. Mouthereau
Inversion of pre-orogenic extensional basins in the external Western Alps: structure, microstructures and restoration
Journal of Structural Geology, 60 (2014), pp. 13-29

Boutoux et al. 2016 A. Boutoux, N., Bellahsen, U., Nanni, R., Pik, Y. Rolland, A., Verlaguet, O. Lacombe
Thermal and structural evolution of a collisional wedge: insights from U-Th-Sm/He thermochronology and RSCM thermometry in the Aiguilles Rouges/Mont Blanc massifs, Western Alps
Tectonophysics, 683 (2016), pp. 109-123

Brandon et al. 1998 M.T. Brandon, M.K., Roden-Tice, J.I. Garver
Late Cenozoic exhumation of the Cascadia accretionary wedge in the Olympic Mountains, northwest Washington State

Geological Society of America Bulletin, 110 (1998), pp. 985-1009

Brockmann 2018 E. Brockmann
LV95 / CHTRF2016 (Swiss Terrestrial Reference Frame 2016) - Teil 2: Auswertung der GNSS-Messungen 2016 und Resultate der Gesamtausgleichung
Swisstopo report (Wabern, Switzerland: Bundesamt für Landestopografie swisstopo), 16-19A (2018), pp. 1-84

Buess 2019 D. Buess
Geologie und Tektonik des nördlichen Randes des Aar Massivs (Urbachtal, Berner Oberland)
MSc thesis University of Bern, (2019), pp-1-91

Burchfiel 1980 B.C. Burchfiel
Eastern European Alpine system and the Carpathian orocline as an example of collision tectonics
Tectonophysics, 1-4 (1980), pp. 31-61

Burkhard 1988 M. Burkhard
L'Helvetique de la bordure occidentale du massif de l'Aar (évolution tectonique et métamorphique
Eclogae geol. Helv., 81 (1988), pp. 63-114

Burkhard 1990 M. Burkhard
Aspects of the large-scale Miocene deformation in the most external part of the Swiss Alps (sub-Alpine molasse to Jura fold belt)
Eclogae Geologicae Helvetiae, 83 (1990), pp. 559-583

Burkhard 1999 M. Burkhard
Strukturgeologie und Tektonik im Bereich AlpTransit
Vorerkundung und Prognose der Basistunnels am Gotthard und am Lötschberg (1999), pp. 45-57

Burkhard and Sommaruga 1998 M. Burkhard, A. Sommaruga
Evolution of the western Swiss Molasse basin: structural relations with the Alps and the Jura belt
Geological Society, London, Special Publications, 134 (1998), pp. 279-298

Butler and Mazzoli 2006 R.W. Buttler, S. Mazzoli
Styles of continental contraction: A review and introduction
Special papers - Geological Society of America 414 (2006), pp. 1

Campani et al. 2012 M. Campani A., F. Herman, N. Mancktelow
Two- and three-dimensional thermal modeling of a low-angle detachment: Exhumation history of the Simplon Fault Zone, central Alps
Journal of Geophysical Research, 115 (2010), B10420, pp. 1-25

Campani et al. 2012 M. Campani A., Mulch, O. Kempf, F. Schlunegger, N. Mancktelow
Miocene paleotopography of the Central Alps

Earth and Planetary Science Letters, 337 (2012), pp. 174-185

Challandes et al. 2008 N. Challandes, D., Marquer, I. Villa
P-T-t modelling, fluid circulation, and 39Ar-40Ar and Rb-Sr mica ages in the Aar Massif shear zones (Swiss Alps)
Swiss Journal of Geosciences, 101 (2008), pp. 269-288

Cenki-Tok (2013) B. Cenki-Tok, J.R. Darling, Y. Rolland, B. Dhuime, C.D. Storey,
Direct dating ofmidcrustal shear zones with synkinematic allanite: new in situ U–Th–Pb geochronological approaches applied to the Mont Blanc massif
Terra Nova, 26 (2013), pp. 29–37

Choukroune and Gapais 1983 P. Choukroune, D. Gapais
Strain patterin in the Aar granite (Central Alps): orthogneiss developed by bulk inhomogeneous flattening
Journal of Structural Geology, 5 (1983), pp. 411-418.

Davis et al. 2008 N. Davis, A., Kronenberg, J. Newman
Plasticity and diffusion creep of dolomite
Tectonophysics, 456 (2008), pp. 127-146

Delle Piane et al. 2008 C. Delle Piane, L., Burlini, K., Kunze, P., Brack, J.P. Burg
Rheology of dolomite: Large strain torsion experiments and natural examples
Journal of Structural Geology, 30 (2008), pp. 767-776

Diamond and Tarantola 2015 L.W. Diamond, A. Tarantola
Interpretation of fluid inclusions in quartz deformed by weak ductile shearing: Reconstruction of differential stress magnitudes and pre-deformation fluid properties
Earth and Planetary Science Letters, 417 (2015), pp. 107-119

Diamond et al. 2018 L.W. Diamond, C. Wanner, H.N. Waber
Penetration depth of meteoric water in orogenic geothermal systems
Geology, 46 (2018), pp. 1063-1066

Diehl et al. 2009 T. Diehl, S., Husen, E., Kissling, N. Deichmann
High-resolution 3-D P-wave model of the Alpine crust
Geophysical Journal International, 179 (2009), pp. 1133-1147

Egli et al. (2018) D. Egli, M., Herwegh, A., Berger, L., Baron, R., Baumann, S. Küng
Structural characteristics and evolution of an exhumed long-lived hydrothermal reservoir
Tectonocphysics, 747-748, pp. 239-258

Egli and Mancktelow 2013 D. Egli, N. Mancktelow
The structural history of the Mont Blanc massif with regard to models for its recent exhumation
Swiss Journal of Geosciences, 106 (2013), pp. 469-489

Egli et al. 2017 D. Egli, N. Mancktelow, R. Spikings

Constraints from 40Ar/39Ar geochronology on the timing of Alpine shear zones in the Mont Blanc-Aiguilles Rouges region of the European Alps
Tectonics, 36 (2017), pp. 730-748

England and Molnar 1990 P. England, P., P. Molnar
Surface uplift, uplift of rocks, and exhumation of rocks
Geology, 18 (1990), 1173-1177

Erne 2014 S. Erne
Temperaturabschätzung der Metasedimente zwischen Gotthard- und Aar-Massiv in der Urseren-Garvera Zone mittels Ramanspektroskopie
Bachelor thesis, (2014), Universität Bern

Escher et al. 1993 A. Escher, H. Masson, A. Steck
Nappe geometry in the Western Swiss Alps
J. Struct. Geol., 13 (1993), pp. 501-509

Fölmli et al. 2015 C. Fölmli, M. Herwegh, F. Schlunegger, A. Anselmetti
Murgänge und Felsstürze im Gebiet Ritzlihorn-Spreitgraben, Guttannen BE–Analyse der Felskonditionierung und des Mur-und Sturzkegels
Swiss Bulletin für angewandte Geologie/Swiss Bulletin de géologie appliquée, 20 (2015), pp. 47-69

Fox et al. 2016 M. Fox, F. Herman, S.D. Willett, S.M. Schmid
The exhumation history of the European Alps inferred from linear inversion of thermochronometric data
American Journal of Science, 316 (2016), pp. 505-541

Frey and Mählman 1999 M. Frey, R.F. Mählman
Alpine metamorphism of the Central Alps, Switzerland
Schweiz. Mineral. Petrogr. Mitt., 79 (1999), pp. 169-183

Fry et al. 2010 B. Fry, F. Deschamps, E. Kissling, L. Stehly, D. Giardini
Layered azimuthal anisotropy of Rayleigh wave phase velocities in the European Alpine lithosphere inferred from ambient noise
Earth and Planetary Science Letters, 297 (2010), pp. 95-102

Garver et al. 2005 J.I. Garver, P.W. Reiners, L.J. Walkers, J.M. Ramage, S.e. Perry
Implications for Timing of Andean Uplift from Thermal Resetting of Radiation-Damaged Zircon in the Cordillera Huayhuash, Northern Peru
Journal of Geology, 113 (2005), pp. 117-138

Gleadow et al. 1983 A. Gleadow, I. Duddy, J. Lovering
Fission track analysis: a new tool for the evaluation of thermal histories and hydrocarbon potential
The APPEA Journal, 23 (1983), pp. 93-102

Glotzbach et al. 2008 C. Glotzbach, J. Reinecker, M. Danisik, M. Rahn, W. Frisch, C. Spiegel
Neogene exhumation history of the Mont Blanc massif, western Alps

Tectonics, 27 (2008), doi.10.1029/2008tc002257

Glotzbach et al. 2010 C. Glotzbach, J. Reinecker, M. Danisik, M. Rahn, C. Spiegel
Thermal history of the central Gotthard and Aar massifs, European Alps: Evidence for steady state, long-term exhumation
Journal of Geophysical Research-Earth Surface, 115 (2010), doi.10.1029/2009jf001304

Glotzbach et al. 2011 C. Glotzbach, P-A. van der Beek, C. Spiegel
Episodic exhumation and relief growth in the Mont Blanc massif, Western Alps from numerical modelling of thermochronology data
Earth and Planetary Science Letters, 304 (2011), pp. 417-430

Goncalves et al. 2012 P. Goncalves, E. Oliot, D. Marquer, J.A.D. Connolly
Role of chemical processes on shear zone formation: an example from the Grimsel metagranodiorite (Aar massif, Central Alps)
Journal of Metamorphic Geology, 30 (2012), pp. 703-722

Grasemann, B. and N. S. Mancktelow 1993 B. Grasemann, N.S. Mancktelow
2-dimensional thermal modeling of normal faulting - the Simplon fault zone, Central Alps, Switzerland
Tectonophysics, 225 (1993), pp. 155-165

Günzler-Seiffert 1943 H. Günzler-Seiffert
Beweise für passive Tektonik im Berner Oberland
Eclogae geol. Helv., 36 (1943), pp. 219-223

Hänni and Pfiffner 2001 R. Hänni, O.A. Pfiffner
Evolution and internal structure of the Helvetic nappes in the Bernese Oberland
Eclogae geol. Helv., 94 (2001), pp. 161-171

Haeuselmann et al. 2007 P. Haeuselmann, D.E. Granger, P.Y. Jeannin, S.E. Lauritzen
Abrupt glacial valley incision at 0.8 Ma dated from cave deposits in Switzerland
Geology, 35 (2007), pp. 143-146

Handy et al. 2010 M.R. Handy, S.M. Schmid, R. Bousquet, E. Kissling, D. Bernoulli
Reconciling plate-tectonic reconstructions of Alpine Tethys with the geological–geophysical record of spreading and subduction in the Alps
Earth-Science Reviews, 102 (2010), pp. 121-158

Herwegh et al. 2017 M. Herwegh, A. Berger, P. Wehrens, R. Baumberger, E. Kissling
Large-Scale Crustal-Block-Extrusion During Late Alpine Collision
Scientific Reports, 7 (2017), doi.10.1038/s41598-017-00440-0

Herwegh and Pfiffner 2005 M. Herwegh, O.A. Pfiffner
Tectono-metamorphic evolution of a nappe stack: A case study of the Swiss Alps
Tectonophysics, 404 (2005), pp. 55-76

Hofmann et al. 2004 B.A. Hofmann, M. Helfer, L.W. Diamond, I. Villa, R. Frei

Topography-driven hydrothermal breccia mineralization of Pliocene age at Grimsel Pass, Aar Massif, Central Swiss Alps
Schweizerische Mineralogische und Petrographische Mitteilungen, 84 (2004), pp. 271-302.

Houlie 2018 N. Houlie, J. Woessner, D. Giardini, M. Rothacher
Lithosphere strain rate and stress field orientations near the Alpine arc in Switzerland
Scientific Reports, 8 (2018), doi:10.1038/s41598-018-20253-z

Hugi 1830 F. J. Hugi
Naturhistorische Alpenreise
Amiet-Lutiger

Hurford 1986 A. J. Hurford
Cooling and uplift patterns in the Lepontine Alps South Central Switzerland and an age of vertical movement on the Insubric fault line
Contributions to Mineralogy and Petrology, 92 (1986), pp. 413-427

Jefferies 2006 S. Jefferies, R. Holdsworth, C. Wibberley, T. Shimamoto, C. Spiers, A. Niemeijer, G. Lloyd
The nature and importance of phyllonite development in crustal-scale fault cores: an example from the Median Tectonic Line, Japan
Journal of Structural Geology, 28 (2006), pp. 220-235

Kammer 1989 A. Kammer
Alpidische Verformung des aarmassivischen Nordrandes
Schweizerische Mineralogische und Petrographische Mitteilungen, 69 (1989), pp. 37-53

Ketcham et al. 2007 R.A. Ketcham, A. Carter, R.A. DonelickJ. Barbarand, A.J. Hurford
Improved modeling of fission-track annealing in apatite
American Mineralogist, 92 (2007), pp. 799-810

Keusen et al. 1989 H.R. Keusen, J. Gangui, P. Schuler, M. Buletti
Felslabor Grimsel
Nagra Technischer Bericht, 87-14 (1989)

Kissling 2008 E. Kissling
Deep structure and tectonics of the Valais—and the rest of the Alps
Bulletin Angewandte Geologie, 13 (2008), pp. 3-10

Kralik et al. 1992 M. Kralik, N. Clauer, R. Holnsteiner, H. Huerner, F. Kappel
Recurrent fault activity in the Grimsel test site (GTS, Switzerland), revealed by Rb-Sr, K-Ar and tritium isotope analysis
Journal of the Geological Society, London, 149 (1992), pp. 293-303

Krayenbuhl and Steck 2009 T. Krayenbuhl, A. Steck

Structure and kinematics of the Jungfrau syncline, Faflertal (Valais, Alps), and its regional significance
Swiss Journal of Geosciences, 102 (2009), pp. 441-455

Labhart 1966 T.P. Labhart
Mehrphasige alpine Tektonik am Nordrand des Aarmassivs: Beobachtungen im Druckstollen Trift-Speicherberg (Gadmental) der Kraftwerke Oberhasli AG
Eclogae Geol. Helv., 59 (1966), pp. 803-830

Labhart 1977 T.P. Labhart
Aarmassiv und Gotthardmassiv
Berlin, Stuttgart, Gebrüder Bornträger (1977), 173 pp.

Lacombe and Bellahsen 2016 O. Lacombe, N. Bellahsen
Thick-skinned tectonics and basement-involved fold–thrust belts: insights from selected Cenozoic orogens
Geological Magazine, 153 (2016), pp. 763-810

Lacombe and Mouthereau 2002 O. Lacombe, Mouthereaus
Basement-involved shortening and deep detachment tectonics in forelands of orogens : insights from recent collision belts (Taiwan, western Alps, Pyrenees)
Tectonics, 21 (2002), 1030

Lafosse et al. 2016 M. Lafosse, A. Boutoux, N. Bellahsen, L. Le Pourhiet
Role of tectonic burial and temperature on the inversion of inherited extensional basins during collision
Geological Magazine, 153 (2016), pp. 811-826

Laubscher 1983 H. Laubscher
Detachment, shear, and compression in the central Alps
Geol. Soc. Am. Mem., 158 (1983) pp.191-211

Leloup et al. 2005 P.H. Leloup, N. Arnaud, E.R. Sobel, R. Lacassin
Alpine thermal and structural evolution of the highest external crystalline massif: The Mont Blanc
Tectonics, 24 (2004), doi.10.1029/2004tc001676

Lihou and Allen 1996 J.C. Lihou, P.A. Allen
Importance of inherited rift margin structures in the early North Alpine Foreland Basin, Switzerland
Basin Research, 8 (1996), pp. 425-442

Lory 1874 C. Lory
Note sur quelques faits de la structure des chaînes centrales des Alpes
Arch. sc. phys. nat., 49 (1874), pp. 89-102

Mancktelow and Grasemann 1997 N.S. Mancktelow, B. Grasemann
Time-dependent effects of heat advection and topography on cooling histories during erosion
Tectonophysics, 270 (1997), pp. 167-195

Mair et al. 2018 D. Mair, A. Lechmann, M. Herwegh, L. Nibourel, F. Schlunegger
Linking Alpine deformation in the Aar Massif basement and its cover units–the case of the Jungfrau–Eiger mountains (Central Alps, Switzerland)
Solid Earth, 9 (2018), pp. 1099-1122.

Marquer 1990 D. Marquer
Structures et déformation alpine dans les granites hercyniens du massif du Gothard (Alpes centrales suisses)
Eclogae Geologicae Helvetiae, 83 (1990), pp. 77-97

Marquer and Burkhard 1992 D. Marquer, M. Burkhard
Fluid circulation, progrssive deformation and mass-transfer processes in the upper crust: the example of basement-cover relationships in the External Crystalline Massifs, Switzerland
J. Struct. Geol., 14 (1992), pp. 1074-1057

Marquer and Gapais 1985 D. Marquer, D. Gapais
Les massifs cristallins externes sur une transversale Guttanen-Val Bedretto (alpes centrales): Structures et histoire cinématique
Comptes rendus de l'Académie des sciences. Série 2, Mécanique, Physique, Chimie, Sciences de l'univers, Sciences de la Terre, 301 (1985), pp. 543-546

Michalski and Soom 1990 I. Michalski, M. Soom
The Alpine thermo-tectonic evolution of the Aar and Gotthard massifs, Central Switzerland: fission track ages on zircon and apatite and K–Ar mica ages
Schweizerische Mineralogische Petrographische Mitteilungen, 70 (1990), pp. 373-387

Mock 2014 S. Mock
Deformation of the sediment-crystalline contact in the northern Aar massif (Innertkirchen, Bernese Oberland)
MSc thesis University of Bern, (2014), pp. 1-92

Mock 2017 S. Mock
The Neogene tectonic and geodynamic evolution of the central Swiss Molasse Basin: An integrative 3-D modeling, tectonic and thermochronological study
University of Bern. PhD thesis (2017), 131pp

Mock 2019 S. Mock, C. von Hagke, F. Schlunegger, I. Dunkl, M. Herwegh
Late Miocene thrusting in the North Alpine foreland: Driven by a deep-seated process and shaped by the local mechanical stratigraphy
Solid Earth Discuss, in press (2019)

Mohn 2012 G. Mohn, G. Manatschal, M. Beltrando, E. Masini, N. Kusznir
Necking of continental crust in magma-poor rifted margins: Evidence from the fossil Alpine Tethys margins
Tectonics, 31 (2012), pp. 1-28

Morgenthaler 1921 H. Morgenthaler

Petrographisch-tektonische Untersuchungen am Nordrand des Aarmassivs
E. Birkhäuser & Cie. (1921)

Mudelsee and Stattegger 1997 M. Mudelsee, K. Stattegger
Exploring the structure of the mid-Pleistocene revolution with advanced methods of time-series analysis
Geologische Rundschau, 86 (1997), pp. 499-511

Müller and Arbenz 1938 F. Müller, P. Arbenz
Geologie der Engelhörner, der Aareschlucht und der Kalkkeile bei Inntertkirchen: Berner Oberland
Beiträge zur Geologischen Karte der Schweiz, NF91 (1938)

Nelson 1992 K. Nelson
Are crustal thickness variations in old mountain belts like the Appalachians a consequence of lithospheric delamination?
Geology, 20 (1992), pp. 498-502

Neugebauer et al. 1980 H. Neugebauer, R. Brotz, L. Rybach
Recent crustal uplift and the present stress field of the Alps along the Swiss Geotraverse Basel-Chiasso
Eclogae Geologicae Helvetiae, 73 (1980), pp. 489-500

Nibourel 2019. L. Nibourel
The structural and thermo-kinematic evolution of the eastern Aar Massif, Switzerland
PhD thesis University of Bern (2019), pp. 172

Nibourel et al. 2018 L. Nibourel, A. Berger, D. Egli, N.K. Luensdorf, M. Herwegh
Large vertical displacements of a crystalline massif recorded by Raman thermometry
Geology, 46 (2018), pp. 879-882

Oliot et al. 2010 E. Oliot, P. Goncalves, D. Marquer
Role of plagioclase and reaction softening in a metagranite shear zone at mid-crustal conditions (Gotthard Massif, Swiss Central Alps)
Journal of Metamorphic Petrology, 28 (2010), pp. 849-871

Pfeiffer et al. 1992 H.R. Pfeiffer, Sanchez, A., C. Degueldre
Thermal springs in granitic rocks from the Grimsel Pass (Swiss Alps): The late stage of a hydrothermal system related to Alpine Orogeny
In: Water-Rock Interaction (Kharaja and Maest) Rotterdam, Balkema, (1992), pp. 1327-1331

Pfiffner et al. 1997 O.A. Pfiffner, S. Sahli, M. Stäuble
Compression and uplift of the external massifs in the Helvetic zone
In: Deep Structure of the Swiss Alps: results of NRP 20, (1997), pp. 139-153

Pfiffner 1993 O.A. Pfiffner

The structure of the Helvetic nappes and its relation to the mechanical stratigraphy
J. Struct. Geology, 15 (1993), pp. 511-521

Pfiffner 2009 O.A. Pfiffner
Geologie der Alpen
Haupt Verlag (2009)

Pfiffner 2016 O.A. Pfiffner
Basement-involved thin-skinned and thick-skinned tectonics in the Alps
Geological Magazine, 153 (2016), pp. 1085-1109

Pfiffner 2017 O.A. Pfiffner
Thick-Skinned and Thin-Skinned Tectonics: A Global Perspective
Geosciences, 7 (2017), pp. 1-71

Pfiffner et al. 2011 O.A. Pfiffner, M. Burkhard, R. Hänni, A. Kammer, R. Kligfield, N. Mancktelow, J.W. Menkveld, J. Ramsay, S.M. Schmid, R. Zurbriggen
Structural Map of the Helvetic Zone of the Swiss Alps
Geological Special Map 1:100'000, Bern, Swisstopo, 128 (2011)

Pfiffner et al. 1997 O.A. Pfiffner, P. Lehner, P. Heitzmann, S. Mueller, A. Steck
Deep Structure of the Swiss Alps: results of NRP 20
Birkäuser, (1997), pp. 1-380

Pleuger et al. 2012 J. Pleuger, N. Mancktelow, H. Zwingmann, M. Manser
K–Ar dating of synkinematic clay gouges from Neoalpine faults of the Central, Western and Eastern Alps
Tectonophysics, 550 (2012), pp. 1-16

Rahn et al. 1997 M.K. Rahn, A.J Hurford, M. Frey
Rotation and exhumation of a thrust plane: Apatite fission-track data from the Glarus thrust, Switzerland
Geology, 25 (1997), pp. 599-602

Rahn et al. 2004 M.K. Rahn, M.T. Brandon, G.E. Batt, J.I. Garver
A zero-damage model for fission-track annealing in zircon
American Mineralogist, 89 (2004), pp. 473-484

Rahn et al. 2019 M.K. Rahn, H. Wang, I. Dunkl
A natural long-term annealing experiment for the zircon fission track system in the Songpan-Garzê flysch, China
Terra Nova, 31 (2019), pp. 295-305

Reinecker et al. 2008 J. Reinecker, M. Danisik, C. Schmid, C. Glotzbach, M. Rahn, W. Frisch, C. Spiegel
Tectonic control on the late stage exhumation of the Aar Massif (Switzerland): Constraints from apatite fission track and (U-Th)/He data
Tectonics, 27 (2008), doi.10.1029/2007tc002247

Reiners and Brandon 2006 P.W. Reiners, M.T. Brandon
Using thermochronology to understand orogenic erosion
Annu. Rev. Earth Planet. Sci., 34 (2006), pp. 419-466

Rohr 1926. K. Rohr
Stratigraphische und tektonische Untersuchung der Zwischenbildungen am Nordrand des Aarmassivs (zwischen Wendenjoch und Wetterhorn)
Beiträge zur Geologie der Schweiz, NF57 (1926)

Rolland et al. 2008 Y. Rolland, M. Rossi, S.F. Cox, M. Corsini, N.S. Mancktelow, G. Pennacchioni, M. Fornari, A. Boullier
40Ar/39Ar dating of synkinematic white mica: insights from fluidrock reaction in low-grade shear zones (Mont Blanc Massif) and constraints on timing of deformation in the NW external Alps
Geological Society of London, Special Publications, 299 (2008), pp. 293–315

Rolland et al. 2009 Y. Rolland, S.F. Cox, M. Corsini
Constraining deformation stages in brittle–ductile shear zones from combined field mapping and 40Ar/39Ar dating: The structural evolution of the Grimsel Pass area (Aar Massif, Swiss Alps)
Journal of Structural Geology, 31 (2009), pp. 1377-1394

Rosenberg and Kissling 2013 C.L. Rosenberg, E. Kissling
Three-dimensional insight into Central-Alpine collision: Lower-plate or upper-plate indentation?
Geology, 41 (2013), pp. 1219-1222

Rosenberg et al. 2015. C.L. Rosenberg, A. Berger, N. Bellahsen, R. Bousquet
Relating orogen width to shortening, erosion, and exhumation during Alpine collision. Tectonics, 34

Rossi et al. 2005. M. Rossi, Y. Rolland, O. Vidal, S.F. Cox
Geochemical variations and element transfer during shear zone development and related episyenites at middle crust depths: insights from the study of the Mont-Blanc Granite (French–Italian Alps)
Geological Society of London, Special Publications, 245 (2005), pp. 373–396

Royden 1993 L.H. Royden
Evolution Of Retreating Subduction Boundaries Formed During Continental Collision
Tectonics, 12 (1993), pp. 629-638

Schaltegger and Corfu 1995 U. Schaltegger, F. Corfu
Late Variscan "Basin and Range" magmatism and tectonics in the Central Alps: evidence from U-Pb geochronology
Geodynamica Acta, 8 (1995), pp. 82-98

Schlatter 2007 A. Schlatter
Das neue Landeshöhennetz der Schweiz LHN95

Geodätisch-geophysikalische Arbeiten in der Schweiz (Schweizerische Geodätische Kommission), 72 (2007), pp. 1-375

Schlunegger and Kissling 2015 F. Schlunegger, E. Kissling
Slab rollback orogeny in the Alps and evolution of the Swiss Molasse basin
Nature Communications, 6 (2015) doi.10.1038/ncomms9605

Schmid and Kissling 2000 S.M. Schmid, E. Kissling
The arc of the western Alps in the light of geophysical data on deep crustal structure
Tectonics, 19 (2000), pp. 62-85

Schmid et al. 1996 S.M. Schmid, O.A. Pfiffner, N. Froitzheim, G. Schönborn, E. Kissling
Geophysical-geological transect and tectonic evolution of the Swiss-Italian Alps
Tectonics, 15 (1996), pp. 1036-1064

Schmid et al. 2017 S.M Schmid, E. Kissling, T. Diehl, D.J. van Hinsbergen, G. Molli
Ivrea mantle wedge, arc of the Western Alps, and kinematic evolution of the Alps–Apennines orogenic system
Swiss Journal of Geosciences, 110 (2017), pp. 581-612

Schneeberger 2017 R. Schneeberger
Interplay in 3D between faults and water flow paths in crystalline bedrock (Grimsel, Switzerland)
Bern University, PhD thesis (2017), pp. 1-146

Schneeberger et al. 2017 R. Schneeberger, M. de La Varga, D. Egli, A. Berger, F. Kober, F. Wellmann, M. Herwegh
Methods and uncertainty estimations of 3-D structural modelling in crystalline rocks: a case study
Solid Earth, 8 (2017), pp. 987-1002

Seward and Mancktelow 1994 D. Seward, N.S. Mancktelow
Neogene kinematics of the Central and Western Alps - evidence from fission-track dating
Geology, 22 (1994), pp. 803-806

Sinclair and Allen 1992 H. Sinclair, P., Allen
Vertical versus horizontal motions in the Alpine orogenic wedge: stratigraphic response in the foreland basin
Basin Research, 4 (1992), pp. 215-232

Singer et al. 2014 J. Singer, T. Diehl, S. Husen, E. Kissling, T. Duretz
Alpine lithosphere slab rollback causing lower crustal seismicity in northern foreland
Earth and Planetary Science Letters, 397 (2014), pp. 42-56

Stampfli et al. 2002 G. Stampfli, G.D., Borel, R., Marchant, J., Mosar
Western Alps geological constraints on western Tethyan reconstructions

Journal of the Virtual Explorer, 8 (2002), pp. 77

Steck 1968 A. Steck
Die alpidischen Strukturen in den zentralen Aaregraniten des westlichen Aarmassivs
Eclogae geol. Helv., 61 (1968), pp. 19-48

Sternai et al. 2012
Pre-glacial topography of the European Alps
Geology, 40 (2012), pp.1067-1070

Studer 1851 B. Studer
Geologie von der Schweiz
Stämpflische Verlagshandlung, (1851)

Stüwe et al. 1994 K. Stüwe, L. White, R. Brown
The influence of eroding topography on steady-state isotherms. Application to fission track analysis
Earth and Planetary Science Letters, 124 (1994), pp. 63-74

Tagami et al. 1998 T. Tagami, R. Galbraith, R. Yamada, G. Laslett
Revised annealing kinetics of fission tracks in zircon and geological implications
Advances in fission-track geochronology, Springer, (1998), pp. 99-112

Tricart 1984 P. Tricart
From passive margin to continental collision; a tectonic scenario for the Western Alps
American Journal of Science, 284 (1984), pp. 97-120

Trümpy 1949 R. Trümpy
Der Lias der Glarner Alpen
Denkschriften der Schweizerischen Naturforschenden Gesellschaft, RTH Zürich, 79 (1949), pp. 1-192

Trümpy 1960 R. Trümpy
Paleotectonic evolution of the Central and Western Alps
Geological Society of America Bulletin, 71 (1960), pp. 843-907

Valla et al. 2012 P.G. Valla, P.A. Beek, D.L. Shuster, J. Braun, F. Herman, L. Tassan-Got, C. Gautheron
Late Neogene exhumation and relief development of the Aar and Aiguilles Rouges massifs (Swiss Alps) from low-temperature thermochronology modeling and 4He/3He thermochronometry
Journal of Geophysical Research: Earth Surface, 117 (2012), doi.org/10.1029/2011JF002043

Valla et al. 2016 P.G. Valla, M. Rahn, D.L. Shuster, D.L. P.A.van der Beek
Multi-phase late-Neogene exhumation history of the Aar massif, Swiss central Alps
Terra Nova, (2016), pp. 1-12, doi.10.1111/ter.12231

Vernon 2008 A.J. Vernon
Thermochronological approach to the late Neogene exhumation of the European Alps
The University of Edinburgh. PhD thesis (2008), pp. 1-216

Vernon et al. 2009 A.J. Vernon, P.A. van der Beek, H.D. Sinclair, C. Persano, J. Foeken, F.M. Stuart
Variable late Neogene exhumation of the central European Alps: Low-temperature thermochronology from the Aar Massif, Switzerland, and the Lepontine Dome, Italy
Tectonics, 28 (2009), doi.10.1029/2008tc002387

von Hagke et al. 2012 C. von Hagke, C. Cederbom, O. Oncken, D. Stöckli, M. Rahn, F. Schlunegger
Linking the northern Alps with their foreland: The latest exhumation history resolved by low-temperature thermochronology
Tectonics, 31 (2012), doi.10.1029/2011TC003078

von Hagke et al. 2014a C. von Hagke, O. Oncken, S. Eveseev
Critical taper analysis reveals lithological control of variations in detachment strength: An analysis of the Alpine basal detachment (Swiss Alps)
Geochemistry, Geophysics, Geosystems, 15 (2014), pp. 176-191

von Hagke et al. 2014b C. von Hagke, O. Oncken, H. Ortner, C.E. Cederborn, S. Aichholzer
Late Miocene to present deformation and erosion of the Central Alps - Evidence for steady state mountain building from thermokinematic data
Tectonophysics, 632 (2014), pp. 250-260

von Raumer and Neubauer 1993 J. Von Raumer, F. Neubauer
Late Precambrian and Palaeozoic evolution of the Alpine basement—an overview
Pre-Mesozoic geology in the Alps, Springer (1993) pp. 625-639

von Tscharner et al. 2016 M. von Tscharner M., S. Schmalholz, J.-L. Epard
3-D numerical models of viscous flow applied to fold nappes and the Rawil depression in the Helvetic nappe system (western Switzerland)
Journal of Structural Geology, 86 (2016), pp. 32-46

Wagner et al. 2012 G.A. Wagner, G.M. Reimer, E. Jäger
Combining controlled-source seismology and local earthquake tomography to derive a 3-D crustal model of the western Alpine region
Geophysical Journal International, 191 (2012), pp. 789-802

Wangenheim 2016 C. Wangenheim
Quantifying fluvial and glacial erosion using (detrital) thermochronology, cosmogenic nuclides and numerical modelling: A case study in the European Alps
University Hanover, Germany. PhD thesis, (2016)

Wehrens et al. 2016 P.C. Wehrens, R. Baumberger, A. Berger, M. Herwegh
Deformation at the frictional-viscous transition: Evidence for cycles of fluid-assisted embrittlement and ductile deformation in the granitoid crust
Tectonphysics, 693 (2016), pp. 66-84

Wehrens 2015 P.C. Wehrens
Structural evolution in the Aar Massif (Haslital transect): Implications for mid-crustal deformation
Institut für Geologie, University of Bern. PhD thesis, (2015), pp. 1-139

Wehrens et al. 2017 P.C. Wehrens, A. Berger, M. Peters, T. Spillmann, M. Herwegh
How is strain localized in a meta-granitoid, mid-crustal basement section? Spatial distribution of deformation in the central Aar massif (Switzerland)
Journal of Structural Geology, 94 (2017), pp. 47-67

Wibberley 2005 C.A. Wibberley
Initiation of basement thrust detachments by fault-zone reaction weakening
Geological Society, London, Special Publications, 245 (2005), pp. 347-372

Yamada et al. 1995 R. Yamada, T. Tagami, S. Nishimura, H. Ito
Annealing kinetics of fission tracks in zircon: an experimental study
Chemical Geology, 122 (1995), pp. 249-258

Zaun and Wagner 1985 P. Zaun, G. Wagner
Fission-track stability in zircons under geological conditions
Nuclear Tracks and Radiation Measurements, 10 (1982), pp. 303-307

Zurbriggen, R. 2015 R. Zurbriggen
Ordovician orogeny in the Alps: a reappraisal
International Journal of Earth Sciences, 104 (2015), pp. 335-350

Figure captions

Figure 1

Geological overview of the Central to Western Alps showing the former European margin with its External Crystalline Massifs (modified after Egli and Mancktelow, 2013). Aar: Aar Massif, AR: Aiguilles Rouge, MB: Mont Blanc, B: Belledonne, Oi: Oisans, NF: Northalpine front, PF: Periadriatic fault, PT: Penninic Thrust.

Figure 2

Sketches of five conceptual models as suggested in the past to explain the exhumation of the Aar Massif (modified after Figs. 2 and 4 of Burkhard, 1990 and 1999, respectively; see text for explanations).

Figure 3

(a) Perspective view on shaded relief map overlain by a geological map (source swisstopo map.geo.admin.ch) and (b) photograph of the steep northern rim (black arrows) of the Aar Massif showing the present day outcrops of basement rocks up to altitudes >3600 m and the steep north-dipping autochthonous to parautochthonous cover sediments (view from Hasliberg towards W). Note the moderately SE-dipping planes in the basement (to to NW (pink arrows in a) Pfaffenchopf fault array: white arrows, see text for explanation). Note sediment wedges of the Loibstock (LBW) and Dossen (DW) within the basement of the Innertkirchen-Lauterbrunnen zone (IKL).

Figure 4

Geological map of the Haslital (central Aar Massif; modified after Wehrens et al., 2017 and Herwegh et al, 2017) showing the main tectonic units and associated rock types, traces of the major fault zones and the link to the respective kinematic deformation phase, as well as new zircon fission track ages (Wangenheim 2016) and literature data (Michalski and Soom, 1991). The study area is the northern rim of the Aar Massif, given here in full colors. Pale colors in the southern part of the map

correspond to data extensively treated in Wehrens et al. (2016, 2017). Inset shows the location of the Aar Massif and the Haslital transect. Lines A-A' (2'659'000/1'206'500 to 2'673'000-1'155'000) and B-B' indicate profile traces of Figures 5, 7, 9-13. PFW: Pfaffenchopf wedge, LBW: Loibstock wedge. Note that for Handegg and Oberaar phases only fault zones with widths >1m are displayed, knowing that a large number of thinner faults exists.

Figure 5

Tectonic NNW-SSE section along the Haslital and fission track data. (a) Section with rock types and major fault planes of the Handegg (red), Oberaar (blue), and Pfaffenchopf (purple) phase. For color code of rock types and section trace AA'(southern Aar Massif internal part) see Fig. 4. MiGr: Mittagfluh granite, CaGr: Central Aar granite, GrGr: Grimsel granodiorite, Helv: Helvetic nappes, Aat: autochthonous sedimentary cover, Gt: Gotthard nappe. (b) Zircon fission track data with absolute ages, stippled line indicates iso-age trend at ~13–12 Ma. (c) Apatite fission track data presented by color-coded age ranges, stippled line indicates iso-age trend at 8-5 Ma.

Figure 6

Polyphase deformation history at the basement-cover contact and in the basement units underneath. (a) Steep SE dipping Handegg phase faults (red) are dissected by moderately SE dipping Pfaffenchopf phase fault planes (purple, array 1). Note the N-directed brittle dissection of the Röti-Fm by the Pfaffenchopf fault planes as well as

the ductile folds in the limestones of the Quinten-Fm (Swiss coordinates 2’674’000/1’179’000). (b) Outcrop with steep SE dipping Handegg structures (S_h) are sheared into Pfaffenchopf fault planes (S_p) and become reactivated with a top to the NW sense of shear. (c) Thin-section (crossed nicols) showing white mica (wm) rich S-C fabrics of the Pfaffenchopf phase, again with top to the NW sense of shear. Note that quartz (qtz) experienced only low-T crystal plasticity (grey arrow) and pressure solution (white arrows) without dynamic recrystallization (Swiss coordinate 2’662’424/1’169’806).

Figure 7

Tectonic NW-SE section showing the basement-cover contact, the sediment wedge at the Paffenchopf as well as schematic structural overprint (modified after Berger et al., 2016). Note multiple deformational overprint and reactivation of pre-existing mechanical discontinuities by Handegg, Pfaffenchopf (array 1), and Gadmen faults. Location of section trace B-B’ shown in Fig. 4.

Figure 8

Lower hemisphere equal-area plots showing the poles of fault planes and stretching lineations for the Handegg, Pfaffenchopf, and Gadmen phases. Black: mean fault plane orientation; grey: mean of the lineation and contours (intervals 2 times uniform distribution).

Figure 9

Quantification of thrusting accommodated by Pfaffenchopf fault array 1. (a) Enlarged cross-section from Fig. 7a displaying the intersection of the different Pfaffenchopf fault planes (numbers 1-14; IKL: Innertkirchen-Lauterbrunnen zone). (b) Distance versus altitude diagram showing the displacement along the individual fault planes, the distance of shortening in the sheets between the faults and the total amount of shortening and displacement calculated on the base of Rohr (1926).

Figure 10

Synthesis on the thermal evolution of the Aar Massif showing maximum burial at the time of peak metamorphic conditions (22-20 Ma) based on data from Figure 5. Red boxes display uncertainties, which result from assuming geothermal gradients of 25°C/km or 30°C/km. (1) and (2) relate, respectively, to used 300°C or 240°C closing temperatures of the ZFT system. On the retrograde path during the Handegg phase (22-12 Ma), the Aar Massif underwent a stage of differential subvertical uplift, which was more pronounced in the south compared to the north. See differences in lengths of red arrows between the 300°C zircon fission track isograde (dark blue stippled line) and the line of maximum vertical uplift (stippled red line). Between 13 Ma and 5 Ma, the entire central and southern part of the Aar Massif was exhumed en-bloc. Only in the northernmost parts (Pfaffenchopf fault domain), thrust-related deformation induced differential movements. After 5 Ma, the nowadays exposed part of the Aar Massif further rose in its entirety as indicated by the continuous and non-disrupted apatite fission track 110°C isograde (bright blue stippled line). Hence, since that time, thrust-related deformation structures must have formed in the non-exposed subsurface

promoting the final stages of exhumation. (3) Bottom diagram shows relative recent uplift (Schlatter, 2007; see also www.geo.admin.ch) with respect to Aarburg (N-CH) as reference point, which itself rises by 0.8 mm/a with respect to stable Europe (Brockmann, 2018).

Figure 11

Reconstruction of the inversion stages of the former European passive continental margin in the Pfaffenchopf area (1-3: marker points). (a) Initial rift-related geometry with normal faults (black), (b) followed by a stage of shortening and strong vertical S-block up reverse faulting (red) during the Handegg phase, and (c) final N-directed shearing (purple) during the Pfaffenchopf phase and N-block up shearing along the steep Gadmen faults (green).

Figure 12

Geological evolution of the Aar Massif. (a) Onset of continent-continent collision with the former proximal passive continental margin of the European plate being bend underneath the tectonically active margin of the overriding plate. Scraping off of the Helvetic nappes (Drusberg (Dr) and Axen (Ax) nappes) and basal amalgamation onto the hanging plate. (b) Delamination in the European lower crust (see Herwegh et al., 2017) and buoyancy-driven, northward decreasing and hence differential uplift of the future Aar Massif. Surface erosion on the hanging wall plate. (c) Further uplift and exhumation of the Aar Massif by north-directed trusting and continuous surface erosion. (d) Today's situation with the risen Aar Massif. Gt: Gotthard nappe.

Figure 13

Structural evolution of the Aar Massif highlighting the deformation phases (based on Figs. 10 and 12). (a) Tectonically active boundary with thrust-related deformation during basal amalgamation of the Helvetic nappes. Note the former Permo-Carboniferous to Mesozoic extensional faults (black lines). (b) Vertical tectonics and differential uplift of the Aar Massif during the Handegg phase reactivates in parts former extensional faults as steep SE-dipping reverse and normal faults. (c) Change from vertical buoyancy-driven tectonics to a late stage transpressional deformation style inducing dextral strike- and oblique-slip shearing along the Grimsel Pass shear zone in the south (Oberaar phase) and contemporaneous north-directed thrusting along the fault arrays (Pfaffenchopf phase) in the northern part of the Aar Massif. (d) Continuous transpressional strain partitioning with progressive formation of further Pfaffenchopf fault arrays in an in-sequence manner while the Grimsel Pass shear zone further accommodates strike-slip shearing. Gt: Gotthard nappe, PA-1..3: Pfaffenchopf fault array 1 to 3.

Figure 14:

Synthesis showing the orogenic timetable from the southern Aar Massif to the Plateau Molasse for the last 25 Ma. Numbers (km/Myr) in the boxes indicate rock uplift rates for the Aar Massif estimated in this study (Handegg and Pfaffenchopf phases; based on ZFT closing temperatures of 300°C[(1)] and 240°C[(2)]) and for the Subalpine and Plateau Molasse based on data from von Hagke et al. (2012)[(3)] and Mock et al.

(2019)[4]. Moreover, incision rates since the Mid-Pleistocene[5] revolution derive from Haeuselmann al. (2007) and recent surface uplift rates from Schlatter (2007)[6], see also www.map.geo.admin.ch). Note that recent uplift rates represent relative rates related to the reference point Aarburg (N-CH), which itself rises by 0.8 mm/a with respect to stable Europe (Brockmann 2018). Widths of boxes relate to maximum estimated rates. The effect of the uplifting Aar Massif on the overlaying Austroalpine(Aust)-Penninic(Pen)-Helvetic(Helv) nappe stack is also indicated.

Figure 15:

P-T-t evolution of the (a) northern and southern Aar Massif (modified after Herwegh et al., 2017) and (b) the Mont Blanc and Aiguilles Rouges Massifs. (a) [1]P/T from Goncalves et al. (2012), age from Challandes et al. (2008) and Rolland et al. (2009). [2]Temperatures from Wehrens (2015), Mullis (1996), and Bergemann et al. (2017), ages from Rolland et al. (2009), Bergemann et al. (2017), and Berger et al. (2017). [3]Temperatures and ages from Berger et al. (2017). [4, 5]Apatite FT ages, temperatures and associated P estimates (used geothermal gradient of 25°/km) from this study. (b) [10]P/T from Rolland et al. (2003), timing from Rolland et al. (2008) and Cenki-Tok et al. (2013). [11]Fluid inclusion data from Marshal et al. (1998) and Rossi et al. (2005). [12] Peak temperature from RSCM thermometry in sediments between Mont Blanc and Aiguilles Rouges from Boutoux et al. (2016). [13]Chlorite thermometry in veins from Rolland and Rossi (2016). [14] Lowest RCSM temperatures from Boutoux et al. (2016). [15]Aiguilles Rouges and [16] Mont Blanc P-T path using temperatures 300°C-100°C and timing obtained via thermal modeling by Boutoux et al. (2016) and transferring them into P estimates assuming a geothermal gradient of 25°C/km.

Deformation events indicated between the two P-T-t diagrams are based on Rolland et al. (2009), Wehrens et al. (2016, 2017), Berger et al. (2017), Herwegh et al. (2017), and this study for the Aar Massif; while Leloup et al. (2005), Rossi et al. (2005), Glotzbach et al. (2008, 2011), Rolland et al. (2008), Egli and Mancktelow (2013), Egli et al. (2017), and Boutoux et al. (2016) provide the base for the Aiguilles Rouges - Mont Blanc Massifs.

Figure 16

Three potential geodynamic end member models for the late Alpine collision stage resulting in the doming up of the Aar Massif and the passive bending of above laying tectonic nappes. (a) Pure-shear/buckle-fold model resulting in a co-axial shortening and bulk flattening (e.g. Choukroune and Gapais, 1983). (b) Classical thrust tectonics forming an antiformal-imbricate-stack, which evolves by progressive shortening during north-directed indentation of the Adriatic plate (e.g. Burkhard, 1999). (c) Mulitstage block-extrusion model, with (1) a first exhumation stage owing to slab rollback of the European lithosphere, lower crustal delamination, and buoyancy driven vertical tectonics in the middle to upper crust; followed by (2) a thrust-dominated final shortening stage (Herwegh et al., 2017; Kissling and Schlunegger, 2018).

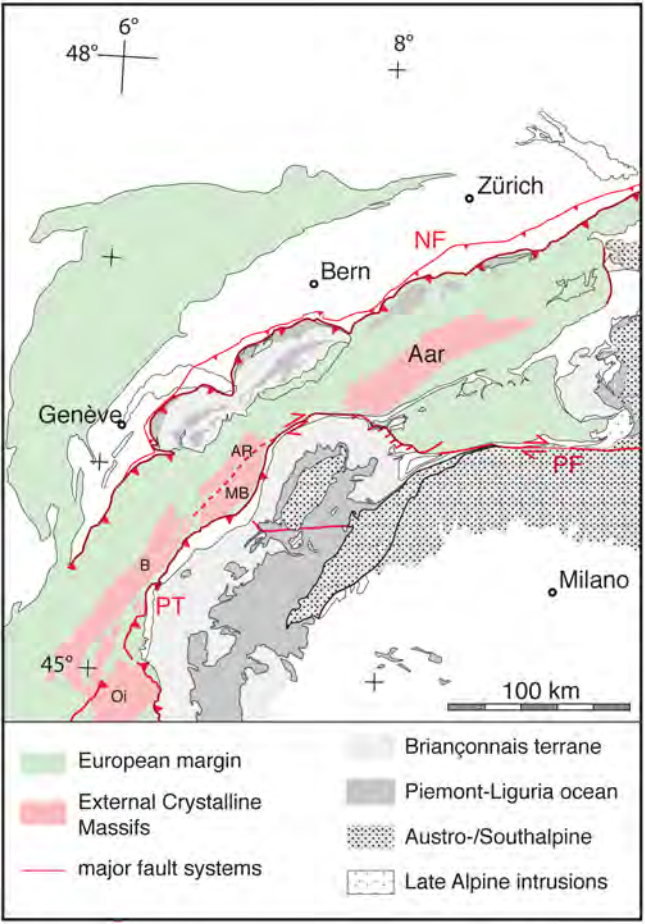
6°
48°
8°
Zürich
NF
Bern
Aar
Genève
AR
MB
PF
B
PT
Milano
45°
Oi
100 km
European margin
External Crystalline Massifs
major fault systems
Briançonnais terrane
Piemont-Liguria ocean
Austro-/Southalpine
Late Alpine intrusions

Figure 1

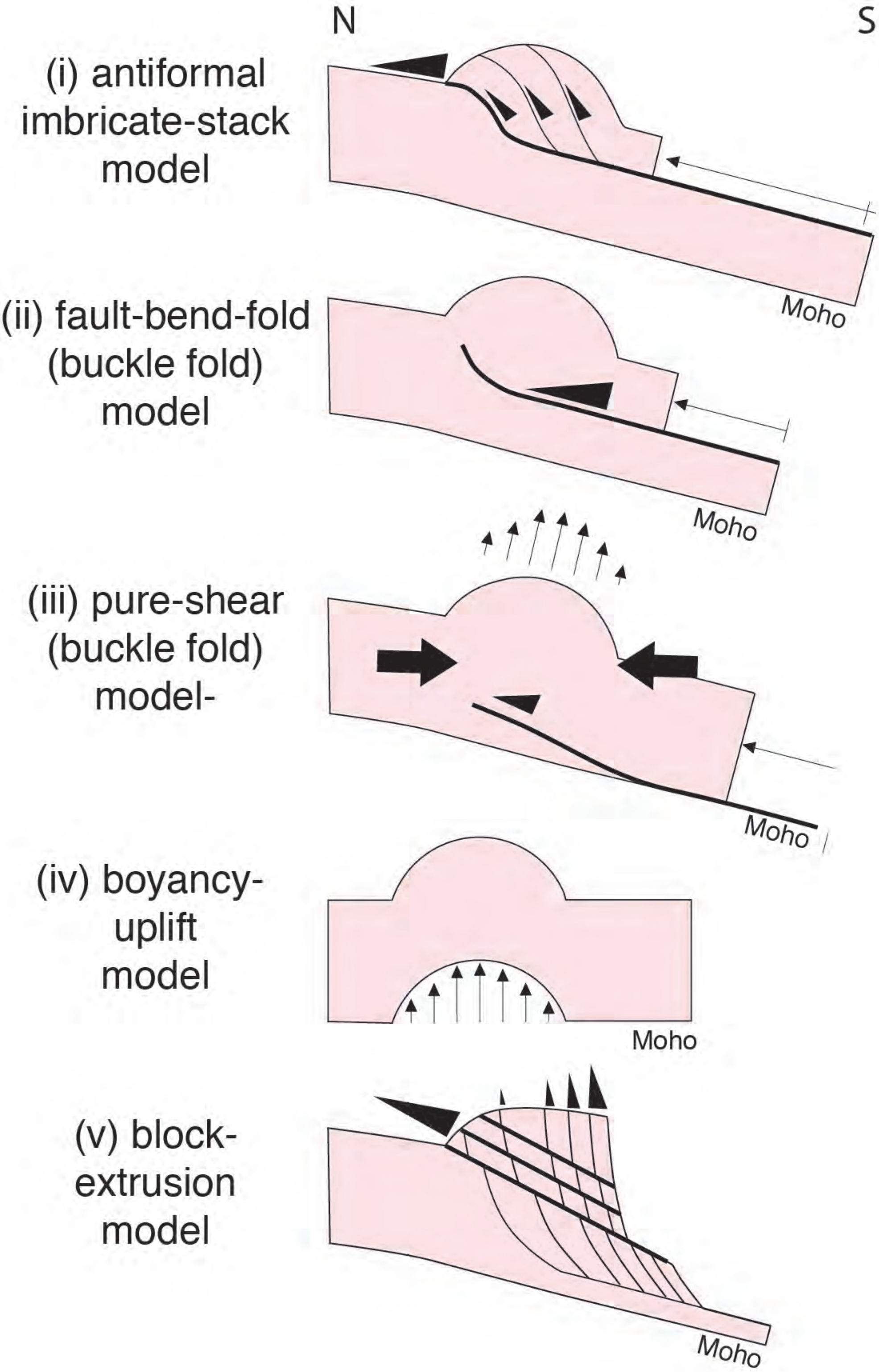
N
S
(i) antiformal imbricate-stack model
Moho
(ii) fault-bend-fold (buckle fold) model
Moho
(iii) pure-shear (buckle fold) model-
Moho
(iv) boyancy-uplift model
Moho
(v) block-extrusion model
Moho

Figure 2

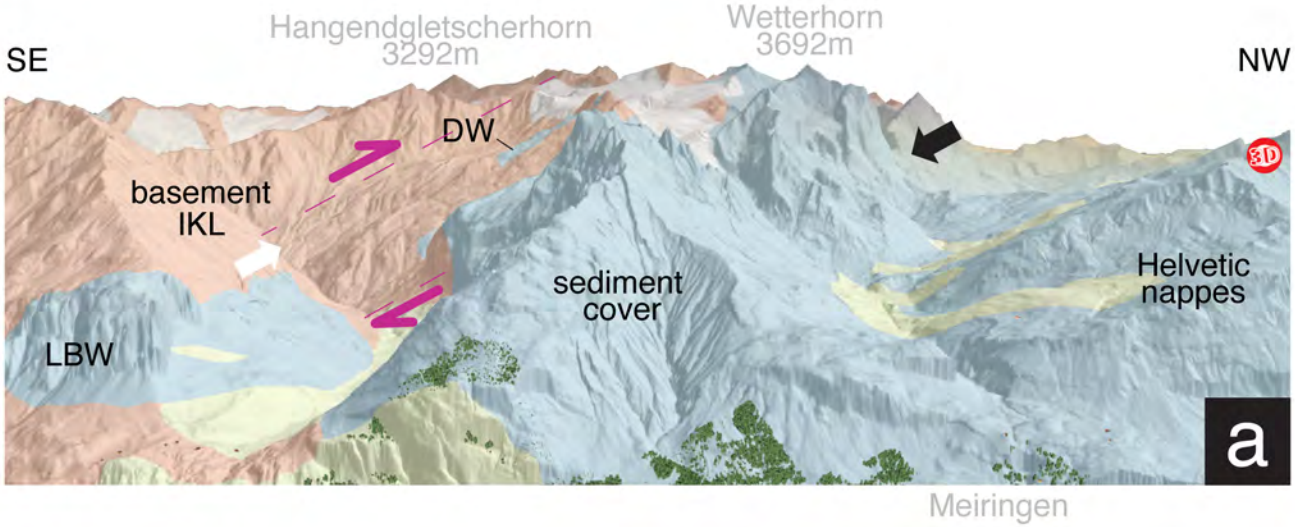
Hangendgletscherhorn
3292m
Wetterhorn
3692m
SE
NW
DW
basement
IKL
sediment
cover
Helvetic
nappes
LBW
a
Meiringen

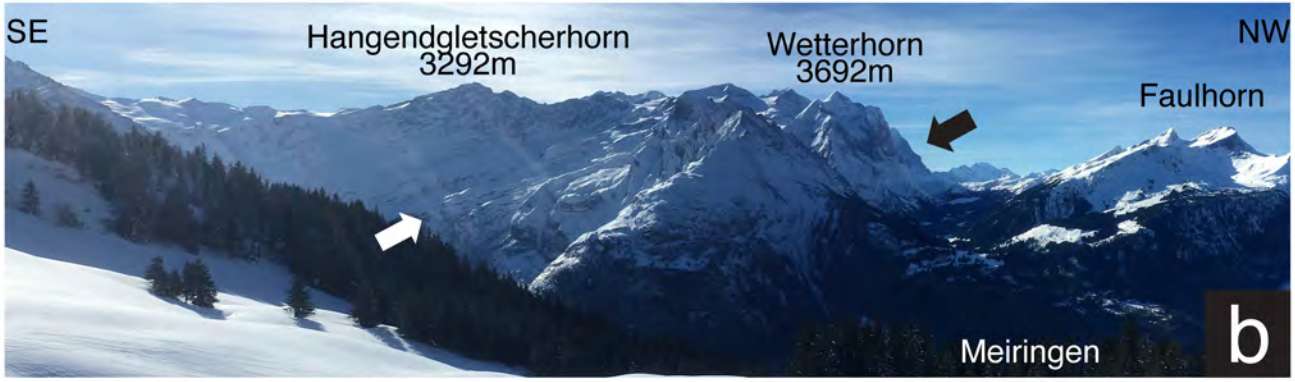
SE
Hangendgletscherhorn
3292m
Wetterhorn
3692m
NW
Faulhorn
Meiringen
b

Figure 3

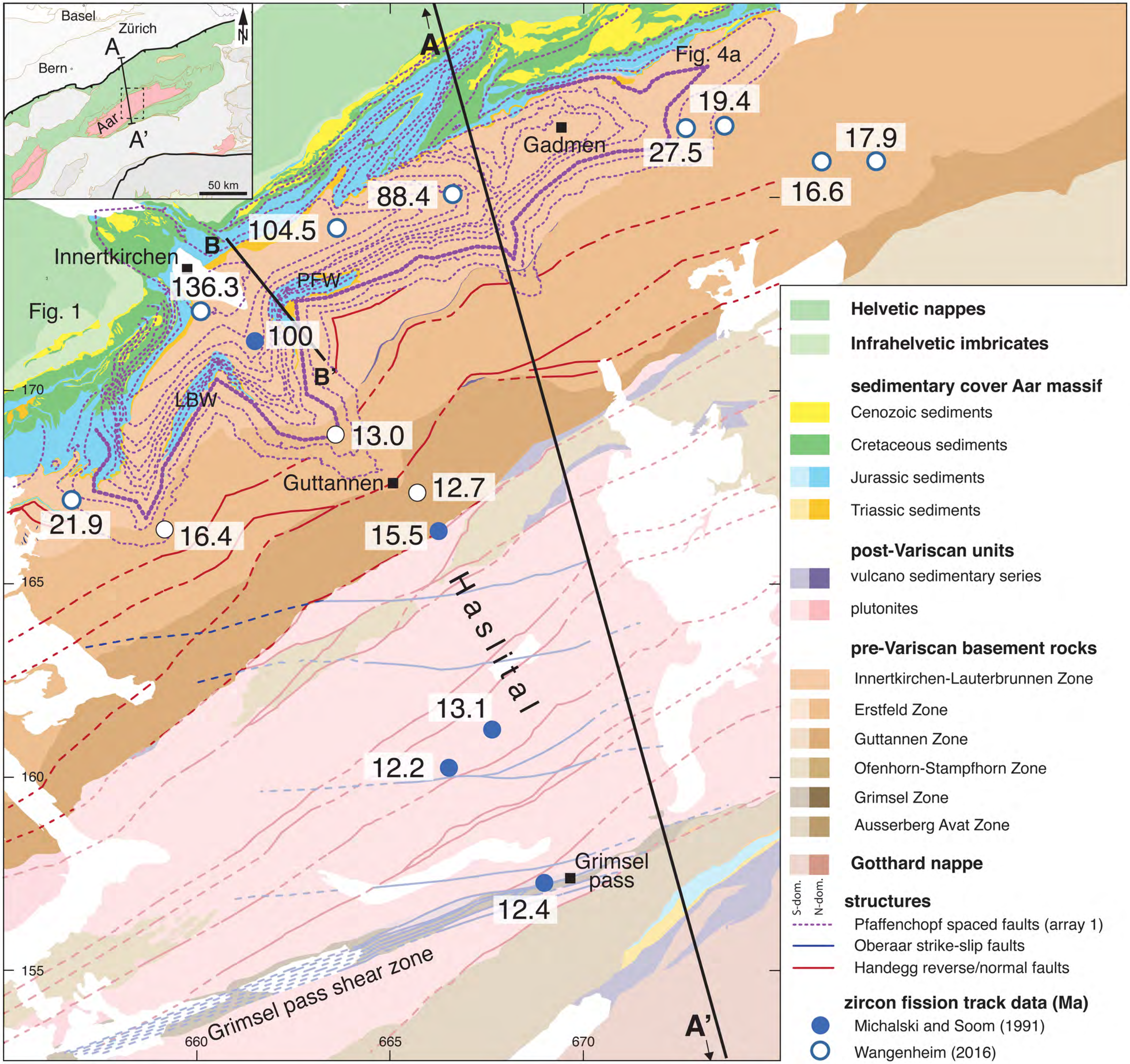
Basel
Zürich
Bern
A
A'
Aar
N
50 km
A
Fig. 4a
19.4
27.5
17.9
16.6
Gadmen
88.4
104.5
B
Innertkirchen
136.3
PFW
Fig. 1
100
B'
LBW
13.0
Guttannen
12.7
21.9
16.4
15.5
Haslital
13.1
12.2
Grimsel pass
12.4
Grimsel pass shear zone
A'
170
165
160
155
660
665
670
Helvetic nappes
Infrahelvetic imbricates
sedimentary cover Aar massif
Cenozoic sediments
Cretaceous sediments
Jurassic sediments
Triassic sediments
post-Variscan units
vulcano sedimentary series
plutonites
pre-Variscan basement rocks
Innertkirchen-Lauterbrunnen Zone
Erstfeld Zone
Guttannen Zone
Ofenhorn-Stampfhorn Zone
Grimsel Zone
Ausserberg Avat Zone
Gotthard nappe
S-dom.
N-dom.
structures
Pfaffenchopf spaced faults (array 1)
Oberaar strike-slip faults
Handegg reverse/normal faults
zircon fission track data (Ma)
Michalski and Soom (1991)
Wangenheim (2016)

Figure 4

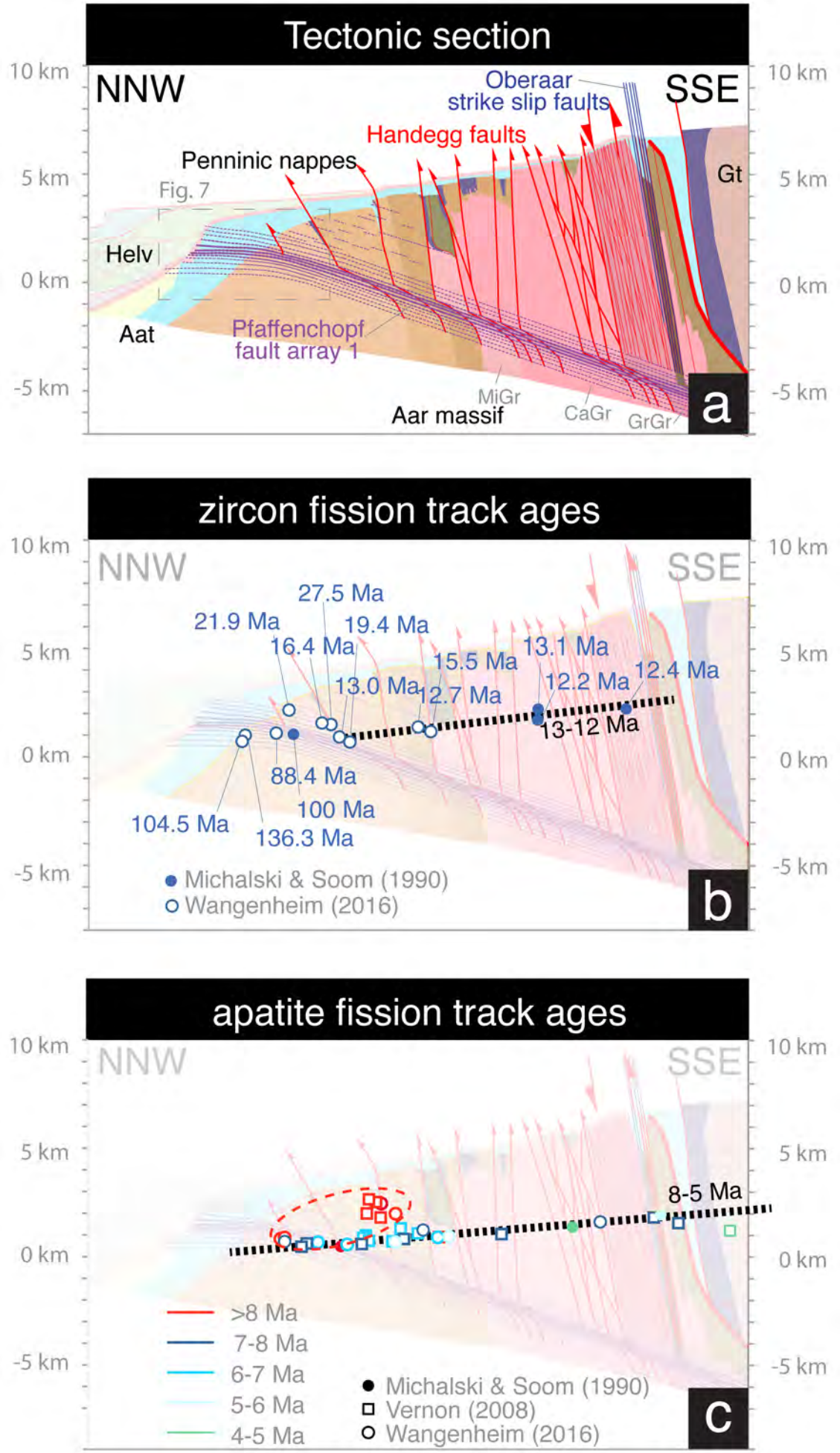
Tectonic section
NNW
SSE
10 km
5 km
0 km
-5 km
Oberaar
strike slip faults
Handegg faults
Penninic nappes
Fig. 7
Helv
Aat
Gt
Pfaffenchopf
fault array 1
MiGr
Aar massif
CaGr
GrGr
a
zircon fission track ages
27.5 Ma
21.9 Ma
19.4 Ma
16.4 Ma
15.5 Ma
13.1 Ma
12.4 Ma
13.0 Ma
12.7 Ma
12.2 Ma
13-12 Ma
88.4 Ma
100 Ma
104.5 Ma
136.3 Ma
Michalski & Soom (1990)
Wangenheim (2016)
b
apatite fission track ages
8-5 Ma
>8 Ma
7-8 Ma
6-7 Ma
5-6 Ma
4-5 Ma
Michalski & Soom (1990)
Vernon (2008)
Wangenheim (2016)
c

Figure 5

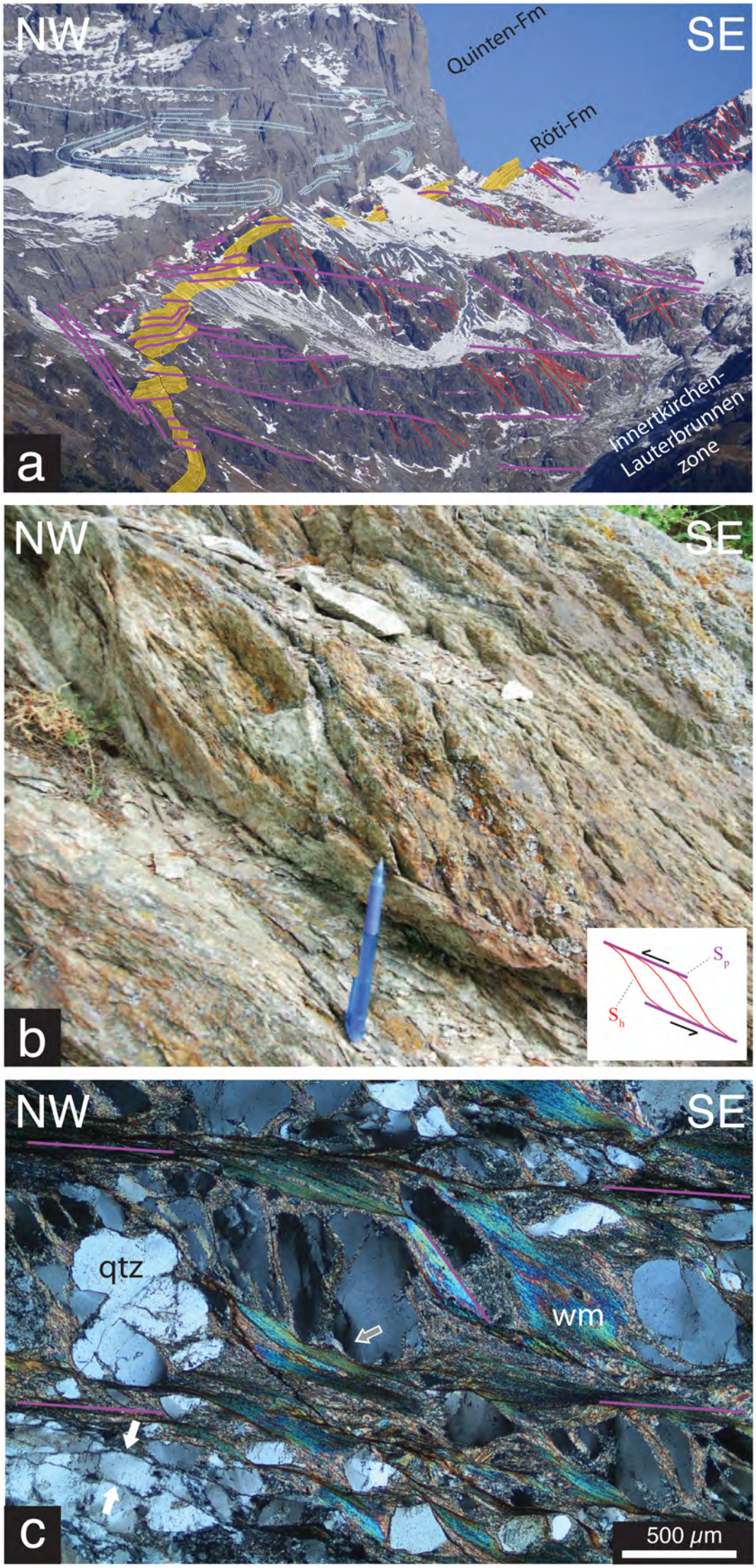
NW
SE
Quinten-Fm
Röti-Fm
Innertkirchen-
Lauterbrunnen
zone
a
NW
SE
S_p
S_h
b
NW
SE
qtz
wm
500 μm
c

Figure 6

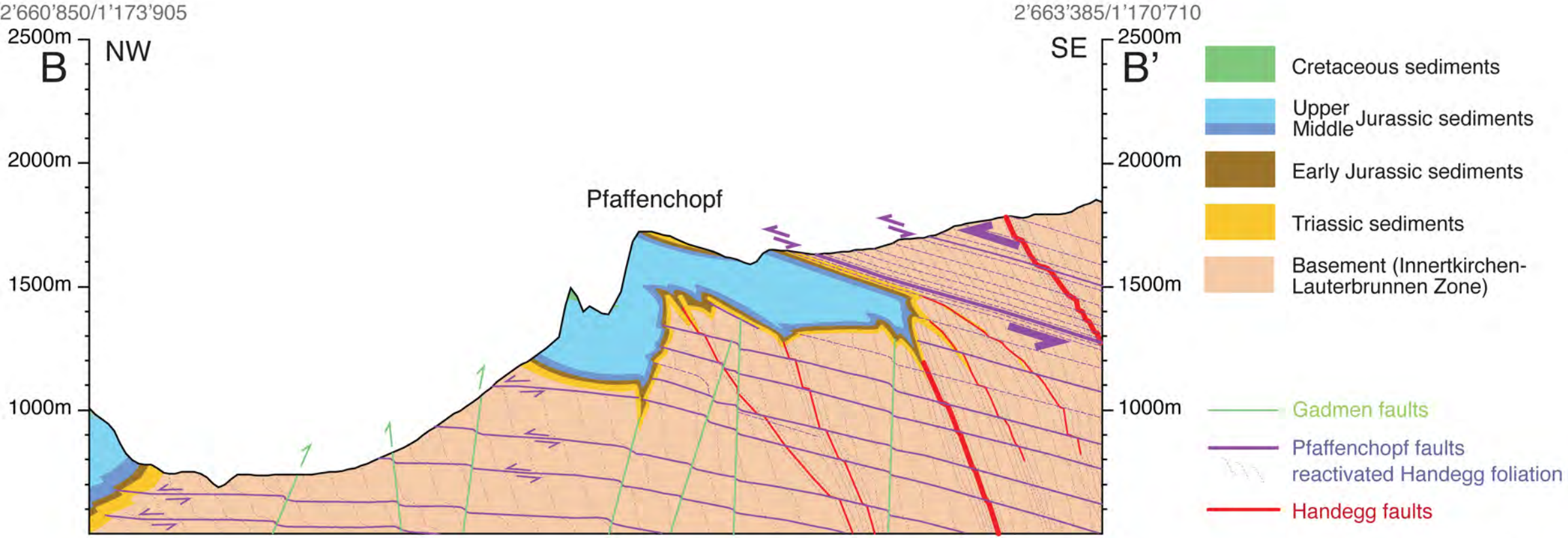
2'660'850/1'173'905
2'663'385/1'170'710
2500m
B
NW
SE
B'
2000m
1500m
1000m
Pfaffenchopf
Cretaceous sediments
Upper
Middle
Jurassic sediments
Early Jurassic sediments
Triassic sediments
Basement (Innertkirchen-
Lauterbrunnen Zone)
Gadmen faults
Pfaffenchopf faults
reactivated Handegg foliation
Handegg faults

Figure 7

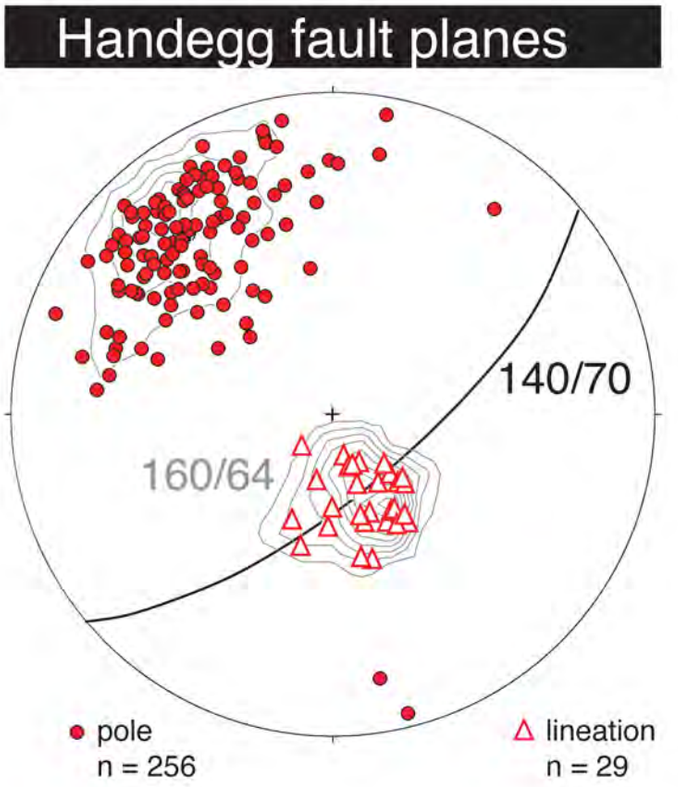
Handegg fault planes
140/70
160/64
pole
n = 256
lineation
n = 29

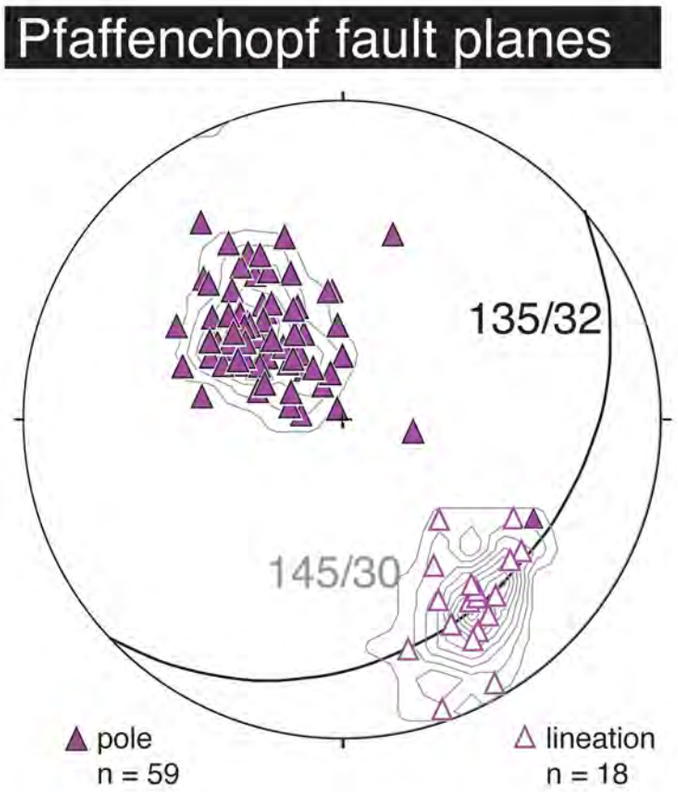
Pfaffenchopf fault planes
135/32
145/30
pole
n = 59
lineation
n = 18

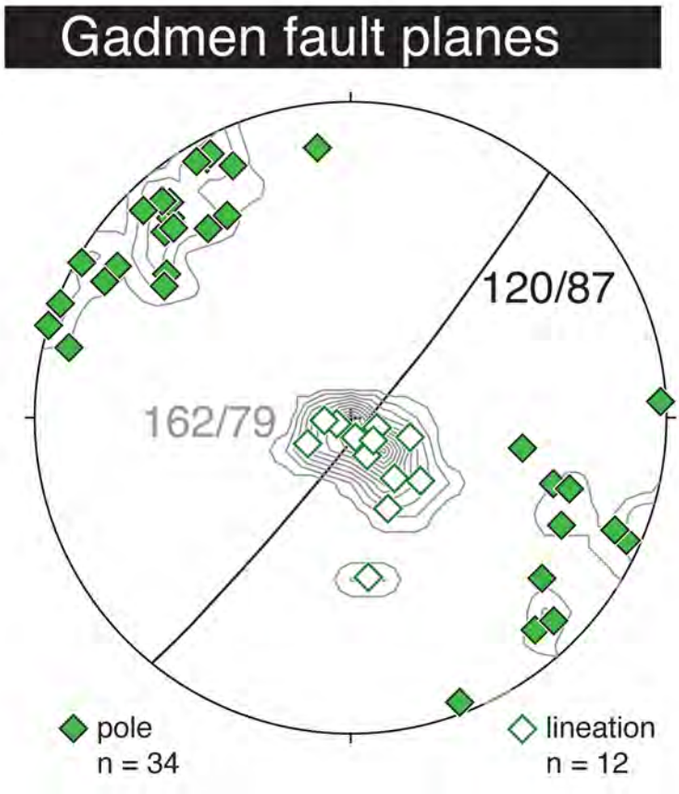
Gadmen fault planes
120/87
162/79
pole
n = 34
lineation
n = 12

Figure 8

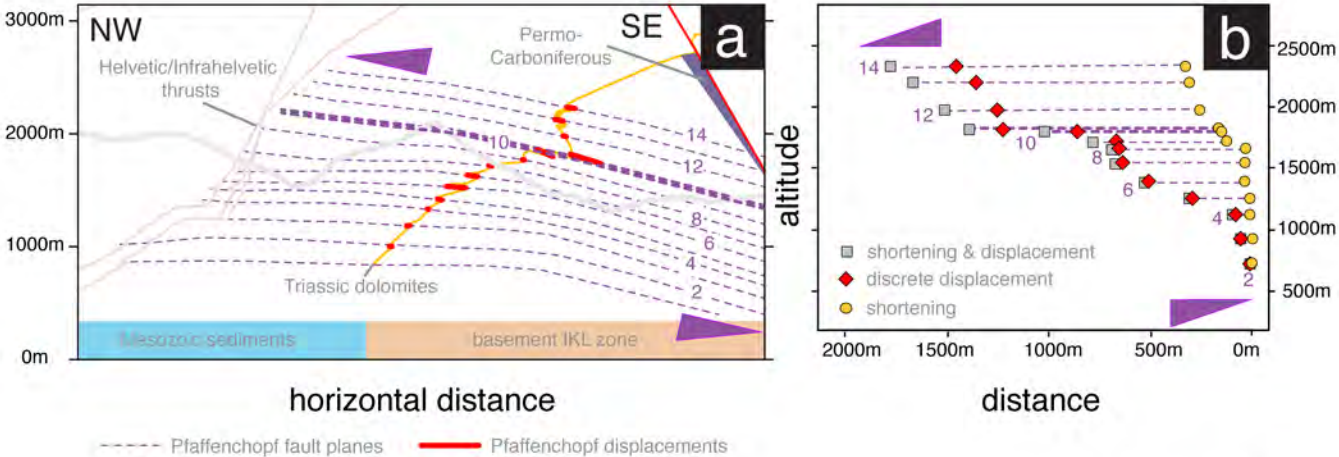
a
NW
SE
Helvetic/Infrahelvetic thrusts
Permo-Carboniferous
Triassic dolomites
Mesozoic sediments
basement IKL zone
3000m
2000m
1000m
0m
horizontal distance
Pfaffenchopf fault planes
Pfaffenchopf displacements
b
altitude
distance
shortening & displacement
discrete displacement
shortening
2500m
2000m
1500m
1000m
500m
0m

Figure 9

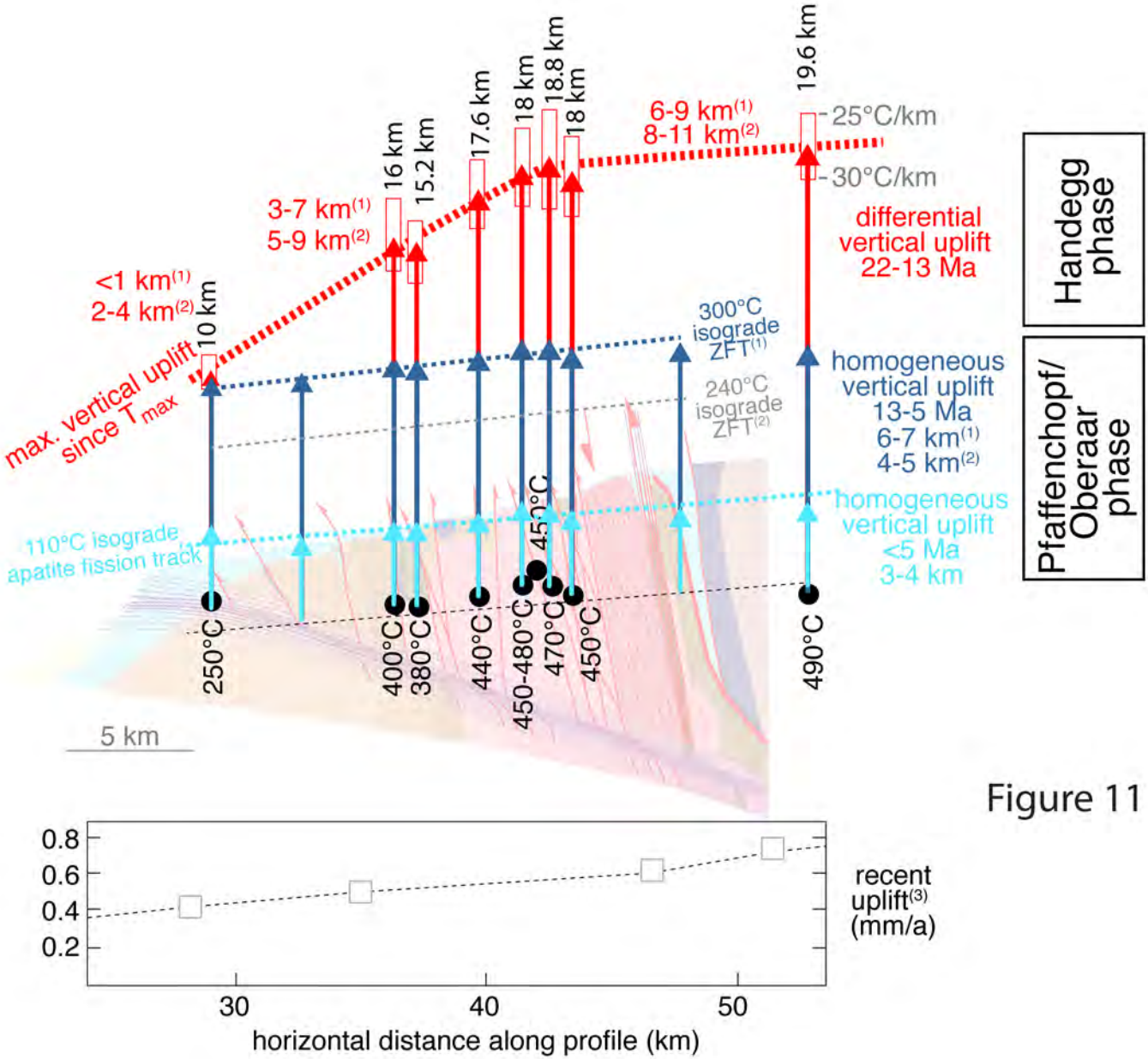
10 km
16 km
15.2 km
17.6 km
18 km
18.8 km
18 km
19.6 km
<1 km(1)
2-4 km(2)
3-7 km(1)
5-9 km(2)
6-9 km(1)
8-11 km(2)
25°C/km
30°C/km
differential
vertical uplift
22-13 Ma
Handegg
phase
max. vertical uplift
since T max
300°C
isograde
ZFT(1)
240°C
isograde
ZFT(2)
homogeneous
vertical uplift
13-5 Ma
6-7 km(1)
4-5 km(2)
Pfaffenchopf/
Oberaar
phase
110°C isograde
apatite fission track
homogeneous
vertical uplift
<5 Ma
3-4 km
250°C
400°C
380°C
440°C
450-480°C
470°C
450°C
490°C
5 km
0.8
0.6
0.4
0.2
recent
uplift(3)
(mm/a)
30
40
50
horizontal distance along profile (km)

Figure 11

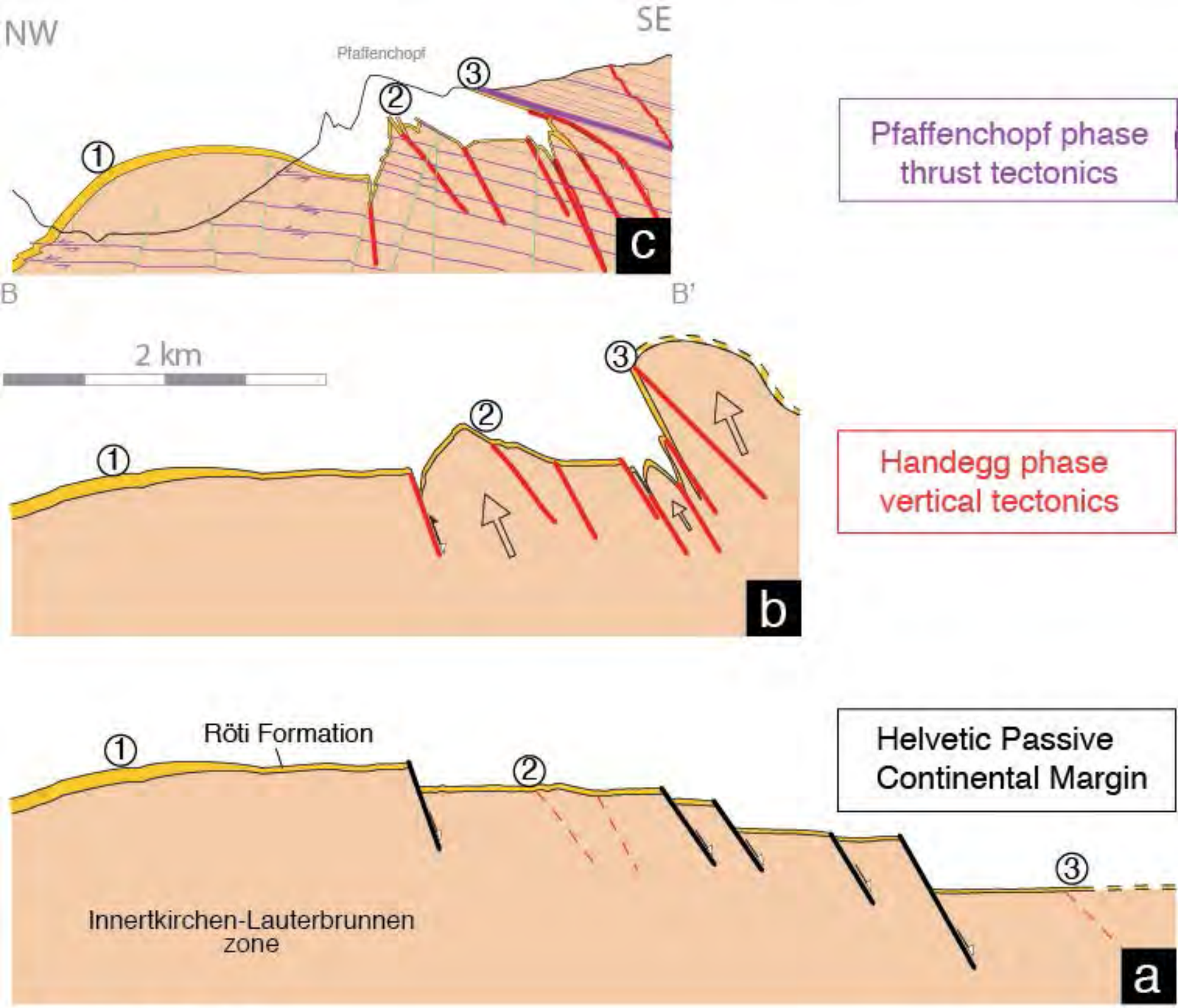
NW
SE
Pfaffenchopf
①
②
③
c
B
B'
Pfaffenchopf phase
thrust tectonics
2 km
①
②
③
b
Handegg phase
vertical tectonics
①
Röti Formation
②
③
Innertkirchen-Lauterbrunnen
zone
a
Helvetic Passive
Continental Margin

Figure 11

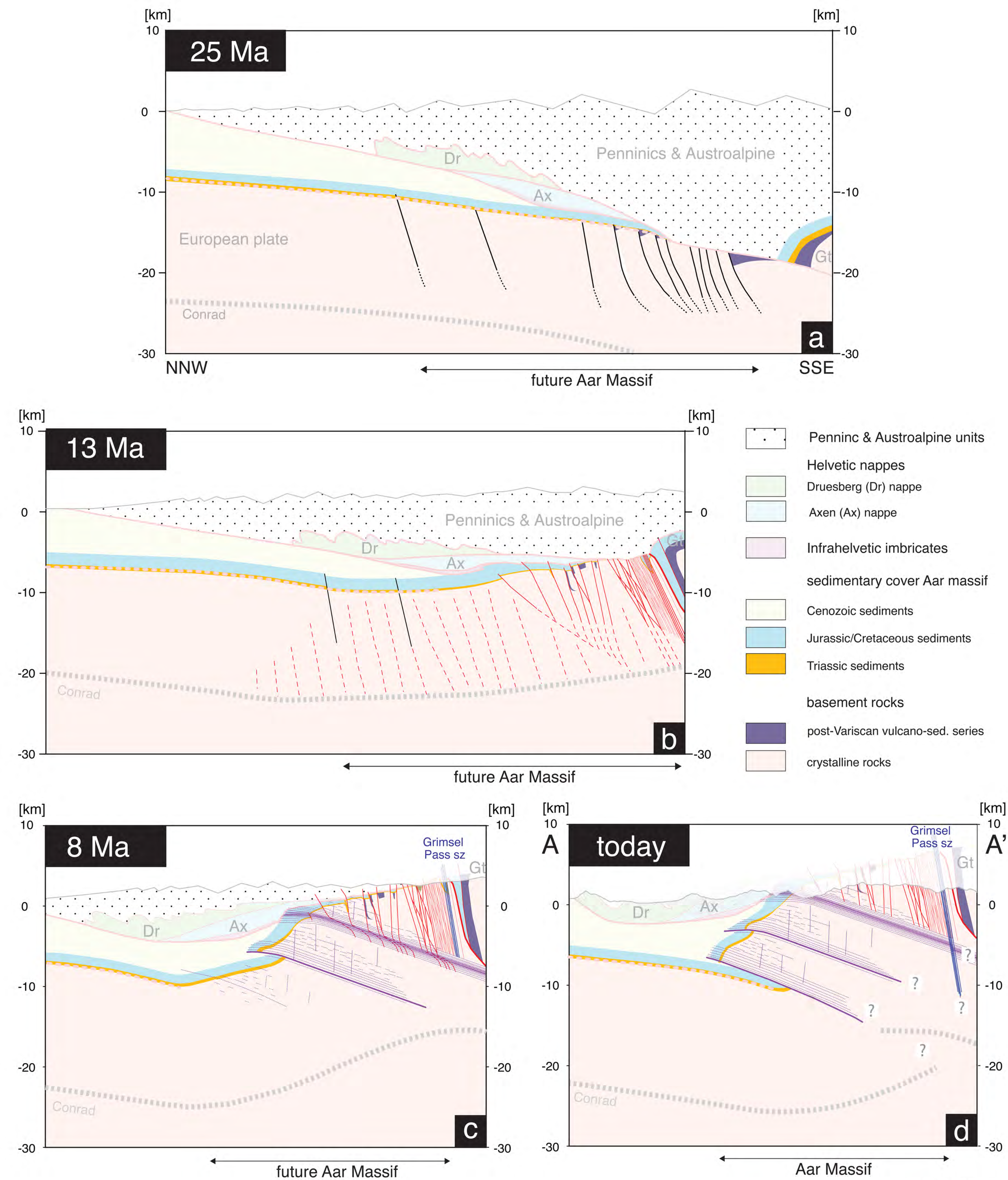
25 Ma
[km]
10
0
-10
-20
-30
Penninics & Austroalpine
Dr
Ax
European plate
Gt
Conrad
a
NNW
SSE
future Aar Massif
13 Ma
Penninics & Austroalpine
Dr
Ax
Gt
Conrad
b
future Aar Massif
Penninc & Austroalpine units
Helvetic nappes
Druesberg (Dr) nappe
Axen (Ax) nappe
Infrahelvetic imbricates
sedimentary cover Aar massif
Cenozoic sediments
Jurassic/Cretaceous sediments
Triassic sediments
basement rocks
post-Variscan vulcano-sed. series
crystalline rocks
8 Ma
Grimsel
Pass sz
Gt
Dr
Ax
Conrad
c
future Aar Massif
A
A'
today
Grimsel
Pass sz
Gt
Dr
Ax
?
Conrad
d
Aar Massif

Figure 12

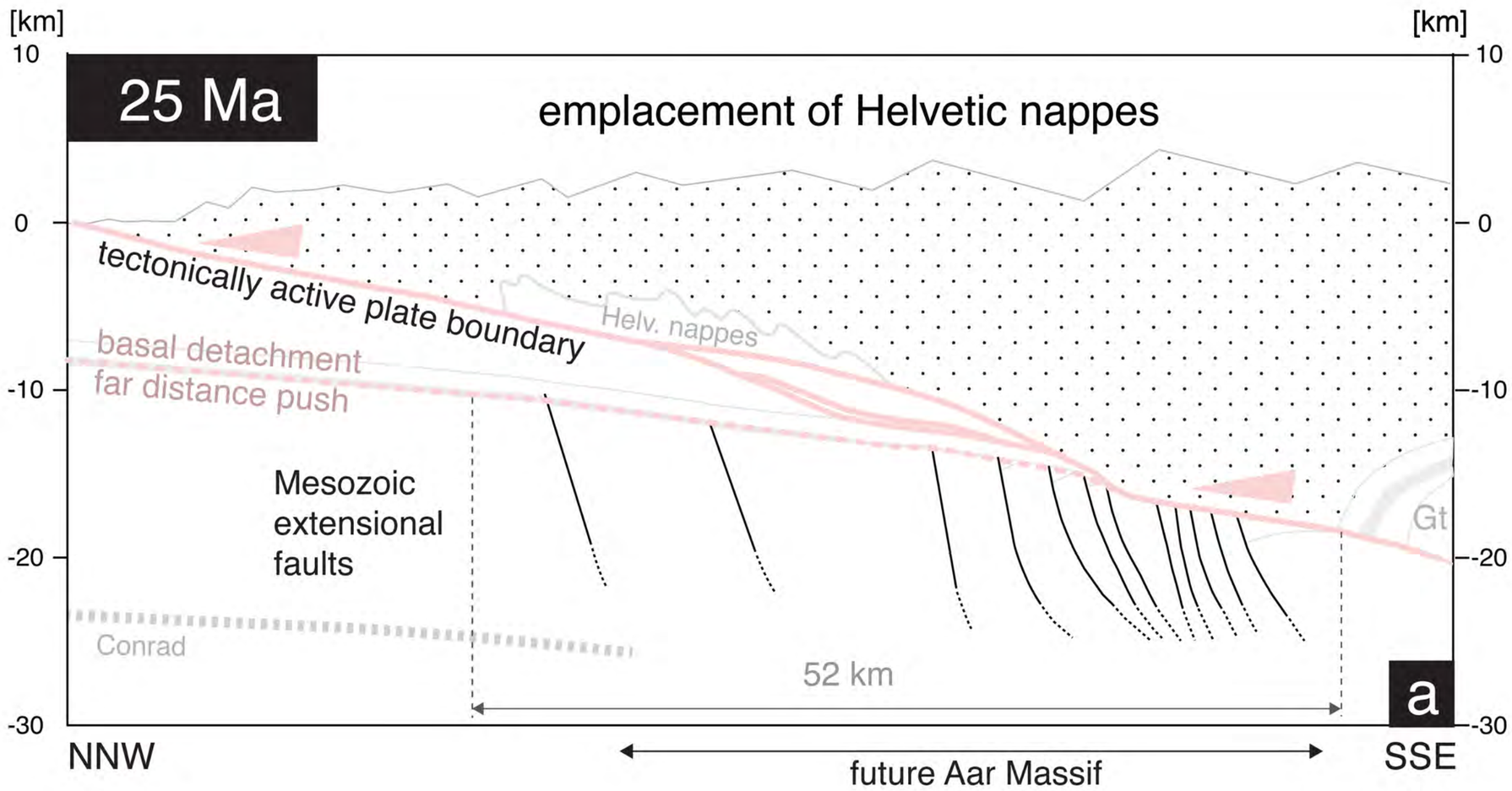
25 Ma
emplacement of Helvetic nappes
[km]
10
0
-10
-20
-30
tectonically active plate boundary
Helv. nappes
basal detachment
far distance push
Mesozoic
extensional
faults
Gt
Conrad
52 km
a
NNW
SSE
future Aar Massif

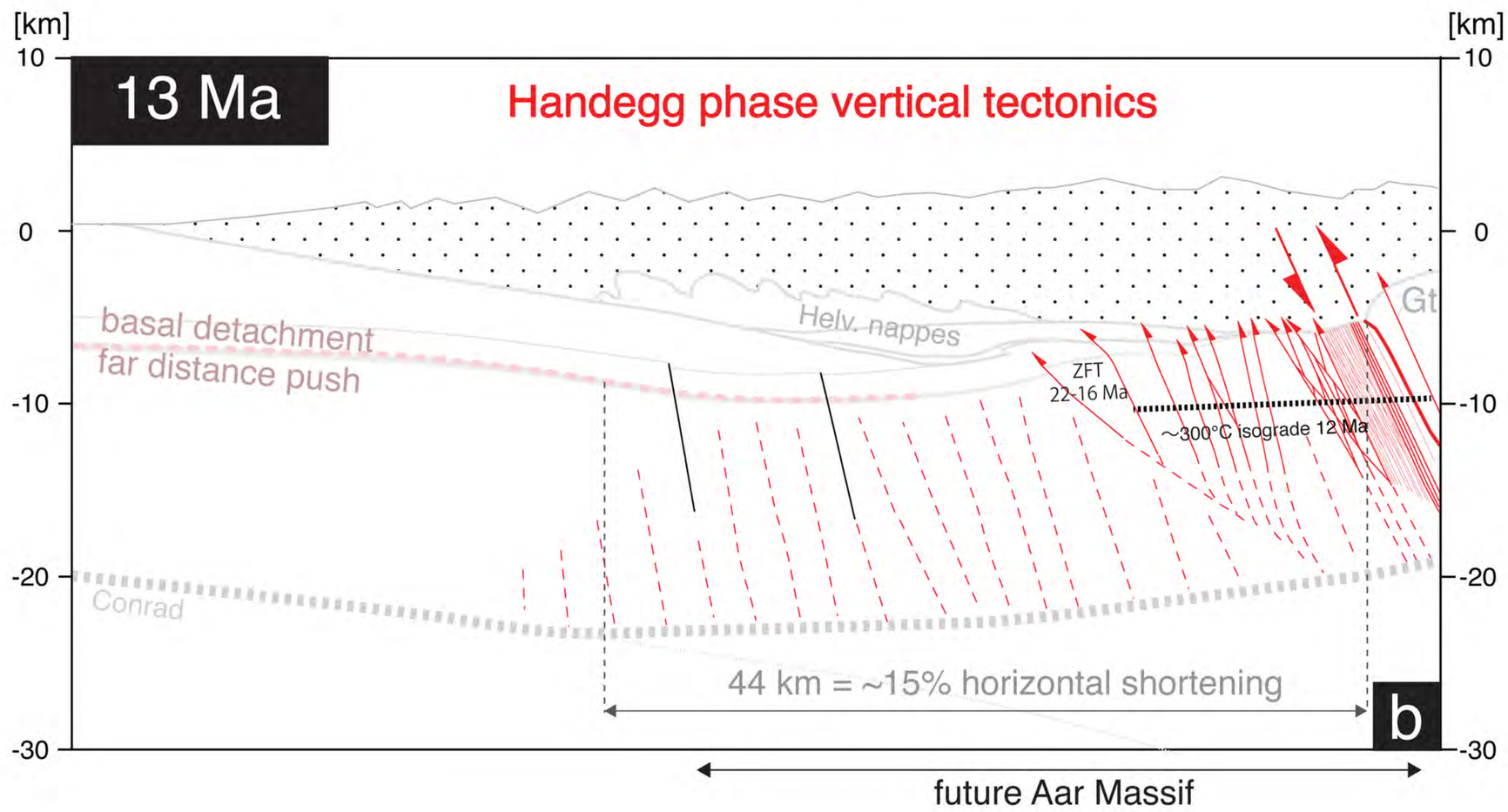
13 Ma
Handegg phase vertical tectonics
[km]
10
0
-10
-20
-30
basal detachment
far distance push
Helv. nappes
Gt
ZFT
22-16 Ma
~300°C isograde 12 Ma
Conrad
44 km = ~15% horizontal shortening
b
future Aar Massif

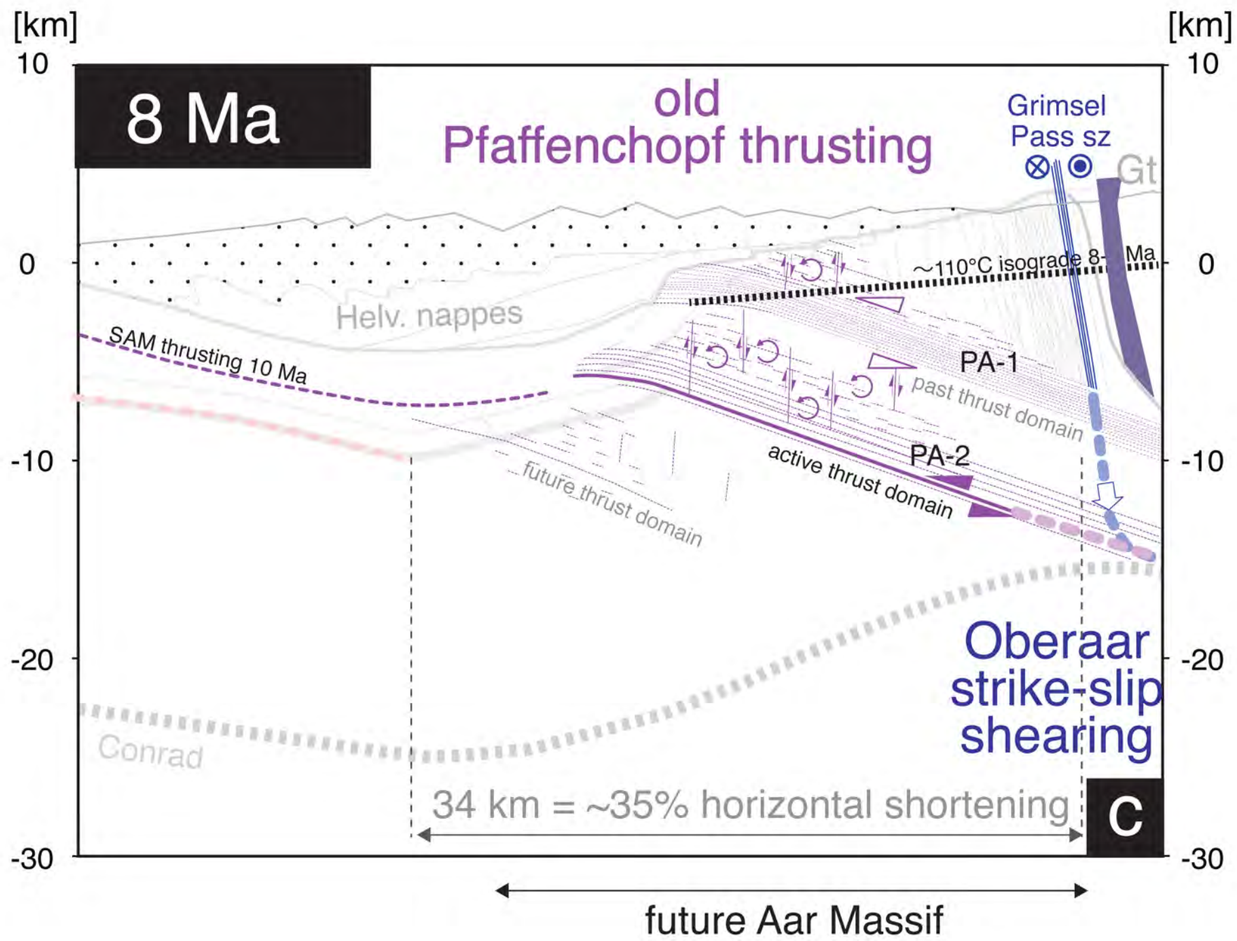
8 Ma
old
Pfaffenchopf thrusting
Grimsel
Pass sz
Gt
[km]
10
0
-10
-20
-30
~110°C isograde 8-
Ma
Helv. nappes
SAM thrusting 10 Ma
PA-1
past thrust domain
PA-2
active thrust domain
future thrust domain
Oberaar
strike-slip
shearing
Conrad
34 km = ~35% horizontal shortening
c
future Aar Massif

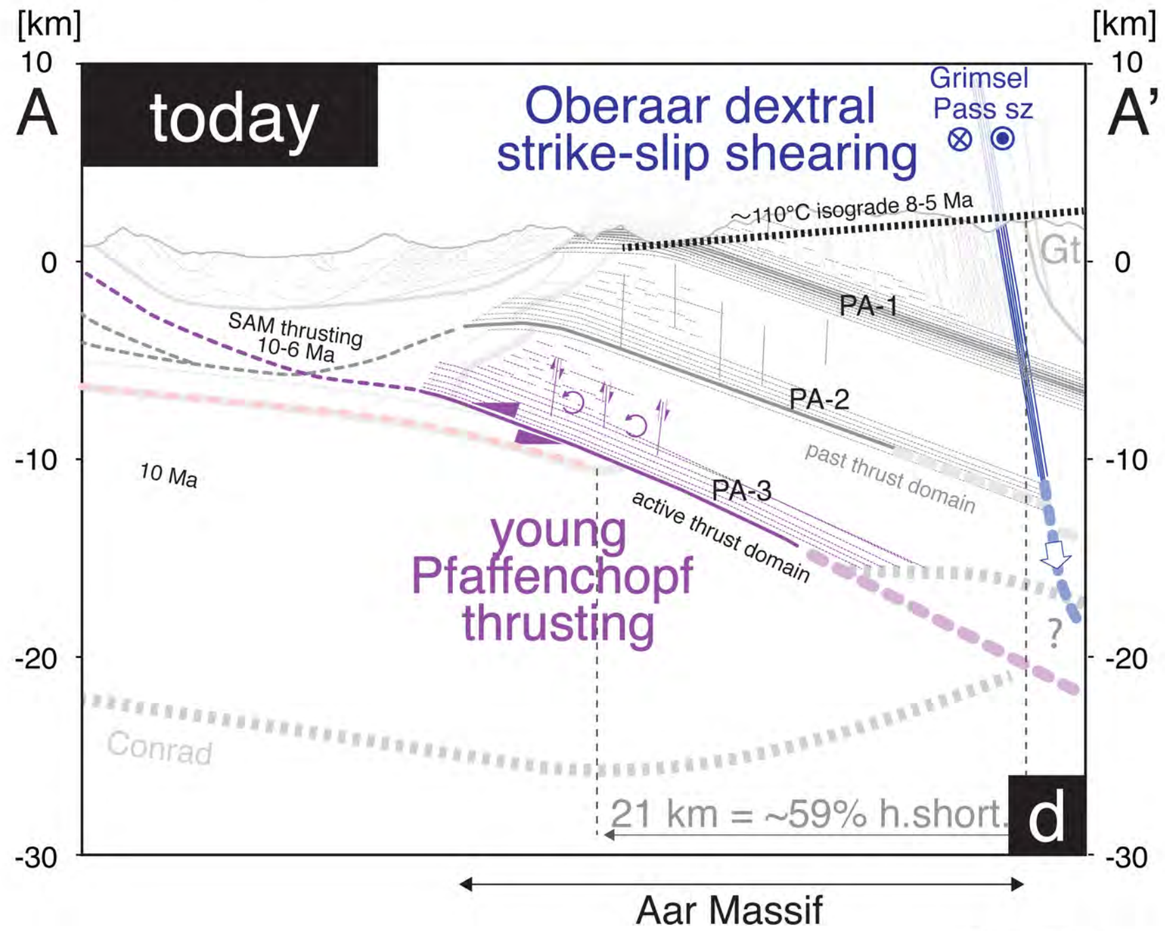
A
today
Oberaar dextral
strike-slip shearing
Grimsel
Pass sz
A'
[km]
10
0
-10
-20
-30
~110°C isograde 8-5 Ma
Gt
SAM thrusting
10-6 Ma
PA-1
PA-2
past thrust domain
10 Ma
PA-3
active thrust domain
young
Pfaffenchopf
thrusting
?
Conrad
21 km = ~59% h.short.
d
Aar Massif

Figure 13

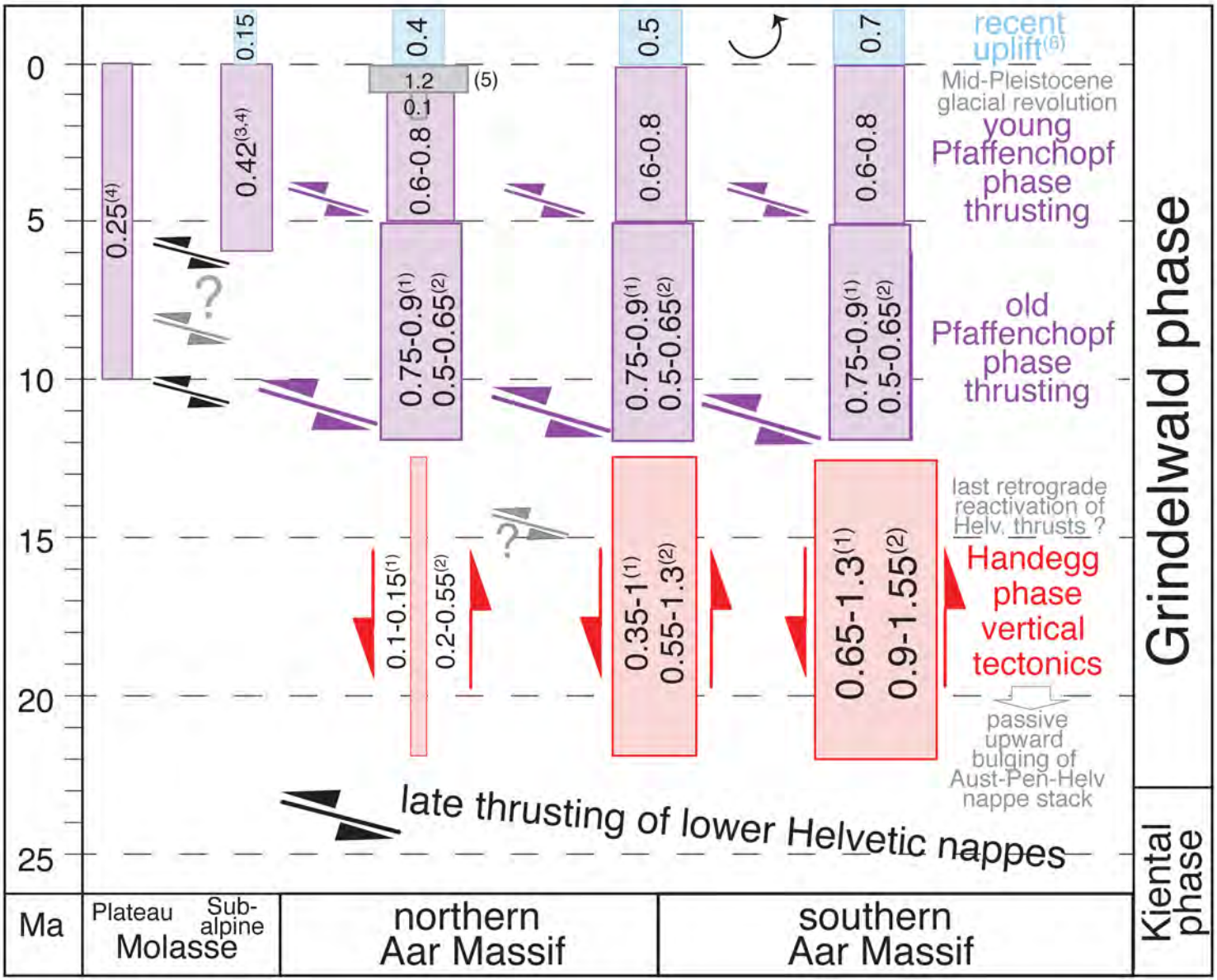
0
5
10
15
20
25
Ma
0.25(4)
0.15
0.42(3,4)
0.4
1.2
(5)
0.1
0.6-0.8
0.75-0.9(1)
0.5-0.65(2)
0.5
0.6-0.8
0.75-0.9(1)
0.5-0.65(2)
0.7
0.6-0.8
0.75-0.9(1)
0.5-0.65(2)
recent uplift(6)
Mid-Pleistocene glacial revolution
young Pfaffenchopf phase thrusting
old Pfaffenchopf phase thrusting
0.1-0.15(1)
0.2-0.55(2)
0.35-1(1)
0.55-1.3(2)
0.65-1.3(1)
0.9-1.55(2)
last retrograde reactivation of Helv. thrusts ?
Handegg phase vertical tectonics
passive upward bulging of Aust-Pen-Helv nappe stack
late thrusting of lower Helvetic nappes
Grindelwald phase
Kiental phase
Plateau
Sub-alpine
Molasse
northern Aar Massif
southern Aar Massif

Figure 14

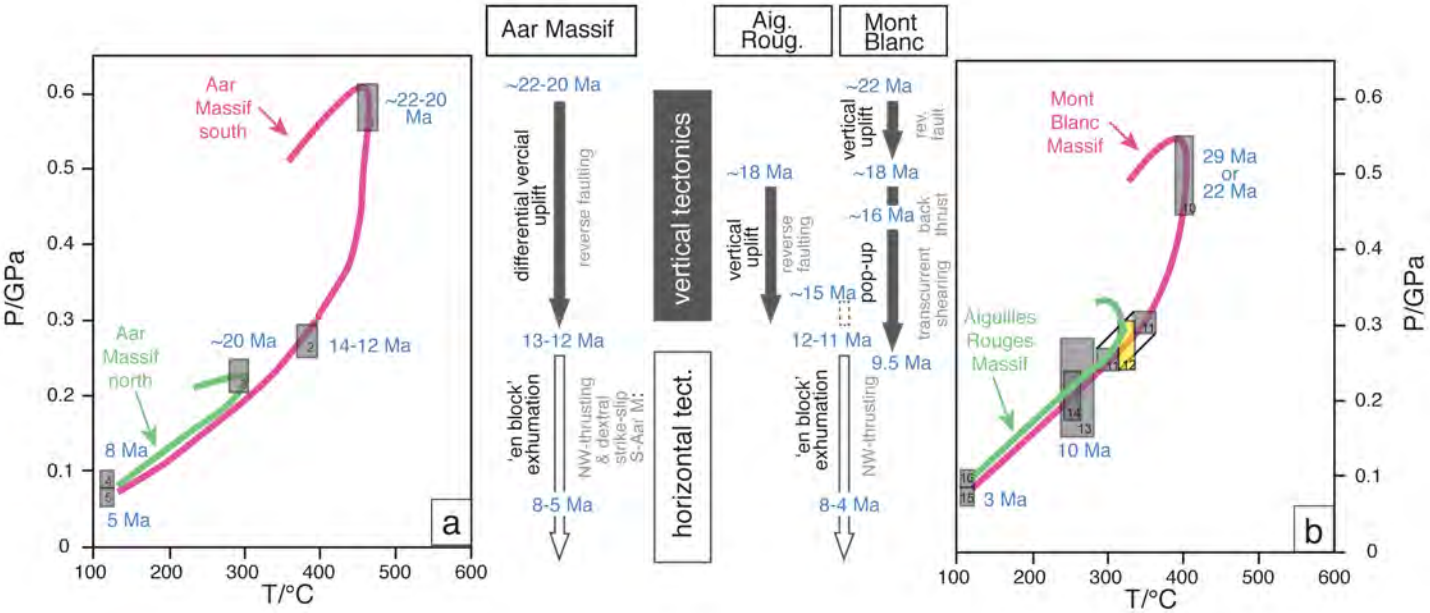
Aar Massif
Aig. Roug.
Mont Blanc
Aar Massif south
~22-20 Ma
Aar Massif north
~20 Ma
14-12 Ma
8 Ma
5 Ma
P/GPa
T/°C
a
~22-20 Ma
differential vercial uplift
reverse faulting
13-12 Ma
'en block' exhumation
NW-thrusting & dextral strike-slip S-Aar M:
8-5 Ma
vertical tectonics
horizontal tect.
~18 Ma
vertical uplift
reverse faulting
~15 Ma
12-11 Ma
'en block' exhumation
NW-thrusting
8-4 Ma
~22 Ma
vertical uplift
rev. fault
~18 Ma
~16 Ma
back thrust
pop-up
transcurrent shearing
9.5 Ma
Mont Blanc Massif
29 Ma or 22 Ma
Aiguilles Rouges Massif
10 Ma
3 Ma
b

Figure 15

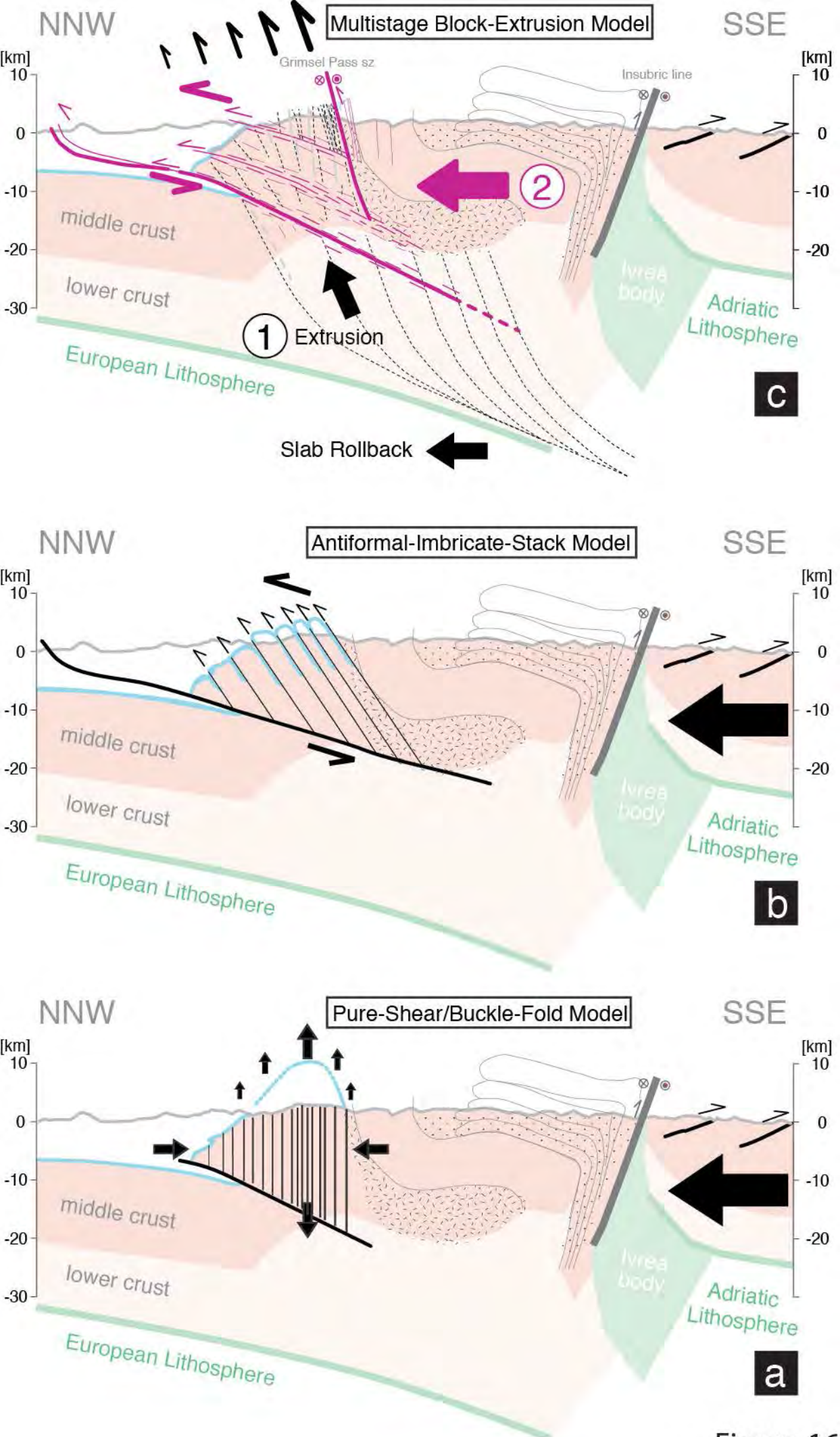
NNW
Multistage Block-Extrusion Model
SSE
[km]
10
0
-10
-20
-30
Grimsel Pass sz
Insubric line
2
middle crust
lower crust
1 Extrusion
Ivrea body
Adriatic Lithosphere
European Lithosphere
c
Slab Rollback
NNW
Antiformal-Imbricate-Stack Model
SSE
middle crust
lower crust
Ivrea body
Adriatic Lithosphere
European Lithosphere
b
NNW
Pure-Shear/Buckle-Fold Model
SSE
middle crust
lower crust
Ivrea body
Adriatic Lithosphere
European Lithosphere
a

Figure 16

x-coordinate (m)	y-coordinate (m)	elevation (m)	lithology	AFT age (Ma)	st.dev. (Ma)	reference
2674071	1151501	1910	granodiorite	10.1	2.1	Michalski and Soom (1990)
2672182	1158375	2130	bt granite gneiss	5.3	1.1	Michalski and Soom (1990)
2672182	1158375	2130	bt granite gneiss	5.3	1.1	Michalski and Soom (1990)
2671112	1162265	1580	bt granite	4.2	1.1	Michalski and Soom (1990)
2668784	1170737	2700	bt-amph-qtz diorite	7.7	1.7	Michalski and Soom (1990)
2668230	1172750	700	bt granite gneiss	12	0.9	Michalski and Soom (1990)
2676841	1141424	1720	micaschist	6.4	1	Vernon (2008)
2674953	1148291	2485	bt_orthogneiss	6.1	0.9	Vernon (2008)
2673030	1155289	1405	orthogneiss	4.6	0.9	Vernon (2008)
2672403	1157569	1790	porphyroid_orthogneiss	7.1	0.9	Vernon (2008)
2672107	1158648	2005	porphyroid_orthogneiss	7.9	1.6	Vernon (2008)
2670233	1165464	1240	orthogneiss	7.3	2.3	Vernon (2008)
2669460	1168276	1095	quartzite_with_ep	8.3	1.3	Vernon (2008)
2669201	1169218	1303	micaschist	6.7	0.6	Vernon (2008)
2669030	1169841	1000	orthogneiss	7.4	0.7	Vernon (2008)
2668991	1169980	1505	orthogneiss	6.9	0.6	Vernon (2008)
2668895	1170333	900	porphyroid_orthogneiss	6.1	0.6	Vernon (2008)
2668747	1170871	2000	orthogneiss	8.6	0.7	Vernon (2008)
2668671	1171147	2720	orthogneiss	8.7	0.9	Vernon (2008)
2668634	1171280	2800	Kfs_orthogneiss	8.7	0.8	Vernon (2008)
2668578	1171485	2200	orthogneiss	8.7	0.8	Vernon (2008)
2668562	1171541	905	micaschist	6.6	0.6	Vernon (2008)
2668555	1171567	1110	orthogneiss	6.9	0.7	Vernon (2008)
2668547	1171598	1005	granitoid	6.2	1	Vernon (2008)
2668518	1171701	780	mu_granitoid	7.3	0.7	Vernon (2008)
2667835	1174186	770	bt_orthogneiss	7.9	0.8	Vernon (2008)
2667768	1174429	640	deformed_granitoid	7.7	0.8	Vernon (2008)
2671444	1161057	1804	Aar granite	7.2	1	Wangenheim (2016)
2671444	1161057	1804	Aar granite	7.2	1	Wangenheim (2016)
2671112	1162265	1580	bt granite	4.2	1.1	Wangenheim (2016)
2669567	1167886	1140	Variscan basement	5.7	0.9	Wangenheim (2016)
2669567	1167886	1140	Variscan basement	5.7	0.9	Wangenheim (2016)
2669449	1168316	1093	Variscan basement	6.1	1	Wangenheim (2016)
2669449	1168316	1093	Variscan basement	6.1	1	Wangenheim (2016)
2669273	1168956	1448	Variscan basement	7.2	0.9	Wangenheim (2016)
2669273	1168956	1448	Variscan basement	7.2	0.9	Wangenheim (2016)
2668917	1170252	908	Variscan basement	5.6	0.9	Wangenheim (2016)
2668917	1170252	908	Variscan basement	5.6	0.9	Wangenheim (2016)
2668914	1170260	2117	Variscan basement	8.3	0.8	Wangenheim (2016)
2668742	1170886	2664	Variscan basement	10.5	1.1	Wangenheim (2016)
2668742	1170886	2664	Variscan basement	10.5	1.1	Wangenheim (2016)
2668334	1172371	780	Variscan basement	6.1	1.2	Wangenheim (2016)
2668334	1172371	780	Variscan basement	6.1	1.2	Wangenheim (2016)
2668230	1172750	700	bt granite gneiss	12	0.9	Wangenheim (2016)
2667974	1173682	850	Variscan basement	6.7	0.9	Wangenheim (2016)
2667974	1173682	850	Variscan basement	6.7	0.9	Wangenheim (2016)
2667938	1173814	793	Variscan basement	8.8	1.1	Wangenheim (2016)
2667938	1173814	793	Variscan basement	8.8	1.1	Wangenheim (2016)
2667622	1174964	1025	Variscan basement	7.4	1.5	Wangenheim (2016)
2667564	1175174	896	Variscan basement	7.5	0.9	Wangenheim (2016)
2667564	1175174	896	Variscan basement	7.5	0.9	Wangenheim (2016)
2667562	1175181	941	Variscan basement	8.5	1.2	Wangenheim (2016)
2667562	1175181	941	Variscan basement	8.5	1.2	Wangenheim (2016)
2667555	1175207	940	Variscan basement	8.2	1.6	Wangenheim (2016)
2667555	1175207	940	Variscan basement	8.2	1.6	Wangenheim (2016)

Table 2: Compilation of apatite fission track (AFT) ages for the Haslital transect. bt: biotite, ep: epidote, kfs: k-feldspar, mu: muscovite, plag: plagioclase,

x coordinate (m)	y coordinate (m)	altitude (m)	lithology	ZFT age (Ma)	st.dev. (Ma)	reference
2661500	1170900	700	bt granite gneiss	100	7	Michalski & Soom (1990)
2666200	1166180	1140	granite	15.5	2	Michalski & Soom (1990)
2667600	1161300	1580	bt granite	13.1	0.7	Michalski & Soom (1990)
2669000	1157500	2130	bt granite gneiss	12.4	0.6	Michalski & Soom (1990)
2666500	1160300	1740	bt granite	12.2	0.9	Michalski & Soom (1990)
2660201	1171687	793	granitic gneiss	136.3	11.9	Wangenheim (2016)
2663450	1174043	896	orthogneiss	104.5	9.3	Wangenheim (2016)
2666285	1174830	941	orthogneiss	88.4	6.5	Wangenheim (2016)
2672179	1176491	1365	granitic gneiss	27.5	3.7	Wangenheim (2016)
2656879	1166952	2117	granitic gneiss	21.9	2	Wangenheim (2016)
2673154	1176669	1614	granitic gneiss	19.4	1.9	Wangenheim (2016)
2677034	1175794	2234	orthogneiss	17.9	1.4	Wangenheim (2016)
2675666	1175861	1883	orthogneiss	16.6	1.2	Wangenheim (2016)
2659268	1166206	1448	granitic gneiss	16.4	1.3	Wangenheim (2016)
2663597	1168790	908	orthogneiss	13	0.9	Wangenheim (2016)
2665642	1167270	1093	bt-plag gneiss	12.7	0.8	Wangenheim (2016)

Table 1: Compilation of zircon fission track (ZFT) ages for the Haslital transect. bt: biotite, plag: plagioclase.